

Generating the Ollie Manoeuvre

Trajectory Optimization and its Application to Skateboarding



Presented by:

Nicholas Haddon Anderson
ANDNIC019

Department of Electrical and Electronics Engineering
University of Cape Town

Prepared for:

Amir Patel

Department of Electrical and Electronics Engineering
University of Cape Town

Submitted to the Department of Electrical Engineering at the University of Cape Town
in partial fulfilment of the academic requirements for a Bachelor of Science degree in
Mechatronics Engineering

November 5, 2019

Key words: trajectory optimization, skateboarding, biomechanics, contact-implicit

Declaration

1. I know that plagiarism is wrong. Plagiarism is to use another's work and pretend that it is one's own.
2. I have used the IEEE convention for citation and referencing. Each contribution to, and quotation in, this report from the work(s) of other people has been attributed, and has been cited and referenced.
3. This report is my own work.
4. I have not allowed, and will not allow, anyone to copy my work with the intention of passing it off as their own work or part thereof.

Signature:

N. H. Anderson

Date: November 5, 2019

Acknowledgements

For a brief moment, I am going to take off my report writing cap and take this opportunity to pay some respects to the people that provided me with help for this project, and my degree as a whole.

But before I dive into any of that, the first and biggest thank you of all must go out to my family: my mother Colleen, late father Greg, and brothers Ryan and Rob. It is without a doubt that, without the guidance from my parents, and the friendships with my brothers, I would not be half the person I am today. I cannot thank you enough.

I would like to thank my supervisor, Dr Amir Patel, and student supervisors, Stacey Shield and Alexander Knemeyer. Without the creativity of Dr Patel, I would never have stumbled upon such an exciting project involving skateboarding (how cool!). I can say with utter conviction that I would never have been able complete this project without the help of Stacey and Alex. To Alex, thank you for getting me going with this project and for the always interesting perspectives that you gave me. To Stacey, I cannot thank you enough for the Pyomo tutorials and endless guidance (and entertainment) along the way.

To my engineering friends, Ben, Joash and Dev. You guys have kept me sane and supported me throughout the whole four years of this degree. I have enjoyed every impromptu song with Ben, every Linux-Windows argument with Joash, and every discussion about God with Dev. I value our friendships dearly and am so glad that I found three lifelong friends to live life and faith with.

A quick thanks must go out to Wian for providing me with guidance throughout my degree. Your excitement for engineering and love for other people is infectious.

Lastly, I'm going to throw in a risky thank you to Christine for supporting me throughout the trials of this project and my entire final year. I cannot imagine what this year would have been like without you.

That is not even close to everyone who has supported me throughout this project and degree, so to those I have not mentioned, thank you also for everything.

Abstract

Model-based trajectory optimization is a rapidly growing field with applications in robotics, biomechanics and sports. One such sport that has not been sufficiently modelled and simulated is the sport of skateboarding. Skateboarders can perform intricate tricks and, in recent times, extreme “big air” manoeuvres. However, the fundamental manoeuvre in skateboarding that transcends all skill levels is called the ollie. Developing a system which can provide insights into the forces involved on a skateboarder performing an ollie has direct clinical applications in injury prevention strategies. Therefore, the purpose of this study was to develop a system which can accurately replicate an ollie in terms of the simulated motion and ground reaction forces (GRFs) experienced by the skateboard.

However, the ollie manoeuvre involves various scheduled and unscheduled contacts between the skateboard, skateboarder and the ground. In the state of current literature, methods to model elastic and inelastic collisions between multi-body systems are sparse. Therefore, in order to formulate a trajectory optimization problem, the contact-implicit method was implemented in conjunction with the hybrid dynamics method to model the multi-body inelastic and elastic collisions involved in the ollie manoeuvre.

Four similar ollie manoeuvres were chosen for the purpose of this study, namely the standing ollie (SO), rolling ollie (RO), ollie up (OU) and ollie down (OD) manoeuvres. Although the simulated trajectory of the OU manoeuvre was not able to be solved under the time-constraints of the project, the results of the trajectory optimization of the developed system showed that the skateboard and skateboarder models were capable of replicating the motion of the SO and RO manoeuvres. But the simulated GRFs experienced by the skateboard performing the SO, RO and OD manoeuvres were significantly different to the peak GRFs and GRF profiles recorded in studies into the biomechanics of skateboarding.

Contents

1	Introduction	1
1.1	Background to the Study	1
1.2	Objectives of this Study	2
1.3	Scope and Limitations	3
1.4	Report Outline	5
2	Science of the Ollie	6
2.1	Understanding the Ollie	6
2.2	Dynamics of the Ollie	8
2.3	Physical Properties of the Skateboard	11
3	Studying Motion with Trajectory Optimization	13
3.1	An Overview of Trajectory Optimization	13
3.1.1	The Trajectory Optimization Problem	13
3.1.2	The Optimal Trajectory	14
3.1.3	Constraints	14
3.1.4	The Objective Function	15
3.2	Modeling Dynamic Systems	16
3.2.1	Coordinates	16
3.2.2	Skateboard Models	21
3.2.3	Deriving the Equations of Motion	22
3.3	Integrating the Dynamics	24
3.3.1	Shooting and Direct Methods	25

3.3.2	Numerical Approaches for ODEs	25
3.4	Modeling Collisions	27
3.4.1	Elastic and Inelastic Collisions	27
3.4.2	Hybrid-Dynamic Systems	27
3.4.3	Hybrid Dynamics Method	28
3.4.4	Contact-Implicit Method	30
3.5	Solving Trajectory Optimization Problems	32
3.5.1	Initialization	32
3.6	The Use of Trajectory Optimization in Motion Studies	33
4	Methodology	34
4.1	Conventions and Notation	34
4.2	Development of the Trajectory Optimization Problem	34
4.3	Formulating the Trajectory Optimization Problem	35
4.3.1	Modeling Approach	35
4.3.2	Transcription Method and Integration Scheme	35
4.3.3	The Objective Function	36
4.3.4	Initialization	37
4.3.5	Software Implementation	37
4.4	Validation of Results	38
5	Model Design and Development	40
5.1	The Bouncing Ball Model	40
5.2	Modeling the Skateboard	41
5.2.1	Summary of Assumptions for the Skateboard Model	42

5.2.2	Generalized Coordinates	43
5.2.3	Applied Forces and Ground Reaction Forces	44
5.3	The Skateboard Tail and Ground Contact	44
5.4	The Skateboard Wheels and Ground Contact	47
5.5	The Foot and Deck Contact	48
5.5.1	The Skateboard-Foot Reaction Force	49
5.5.2	The Skateboard Reference Frame	51
5.5.3	The Skateboard-Foot Friction Force	52
5.6	The Ground Function	56
5.7	Development of the Skateboarder Model and the Ollie	57
5.7.1	Design 1: Fixed Position of the Applied Forces on the Skateboard	59
5.7.2	Design 2: Dynamic Position of the Applied Forces on Skateboard	64
5.7.3	Design 3: Monopods on Skateboard	68
5.8	Final Design: Biped with Torso on Skateboard	79
5.8.1	Modeling the System	79
5.8.2	The Trajectory Optimization Problems	83
6	Results	93
6.1	The SO Simulation Results	93
6.2	The RO Simulation Results	93
6.3	The OD Simulation Results	94
6.4	Summary of Peak Ground Reaction Forces	94
7	Discussion	98
7.1	The Simulated Trajectories	98

7.1.1	The SO simulated Trajectory	98
7.1.2	The RO simulated Trajectory	101
7.2	The Ground Reaction Forces	102
7.2.1	Peak Ground Reaction Forces	103
7.2.2	Ground Reaction Force Profiles	103
7.3	Additional Observations	106
8	Conclusions	108
9	Recommendations for Future Work	110
9.1	Development of the System Models	110
9.1.1	The Skateboarder Model	110
9.1.2	The Skateboard Model	111
A	Additional Information	117
A.1	Example: Application of the Euler-Lagrange Method for Chapter 3 . . .	117
B	Links to Simulation Videos & Code	119
B.1	The Simulated Videos	119
B.2	The Python Code	120

List of Figures

3.5	The skateboard model used in the study by Kuleshov et al. [9] similar to that of the other studies deriving the dynamics of the skateboard in the transverse plane [10][11].	21
3.6	Direct transcription methods represent the control as a piecewise-constant trajectory and the state as a piecewise-linear trajectory [12].	26
3.7	A visual description of hybrid-dynamic system state trajectories - the initial state trajectories are continuous until the guard condition is met, then a discontinuous change in state occurs. A simple example of a single discontinuous state mapping is shown in (a) and a complex example with multiple discontinuous state mappings is shown in (b) [13].	28
3.8	An illustration of the hybrid models of the ball - when it is in contact with the ground, \ddot{y}_{gnd} , and when it is above the ground, \ddot{y}_{air}	29
3.9	The ollie manoeuvre was posed as discrete hybrid dynamic models in the study by Kolev [14].	30
3.10	A visual depiction of the friction cone created in the implementation of the contact-implicit method [7].	32
3.11	An illustration of local and global minima in an optimization problem, with the shaded area representing conditions where the constraints are not satisfied [12].	33
3.12	Results from the study by Mordatch et al. which used trajectory optimization to generate human manoeuvres [15].	33
4.1	The notation adopted for this study to describe the variables in the systems.	34
4.2	The trajectory of the front (red) and back (blue) wheels, and the centre of mass (green) of the skateboard performing an ollie. Adapted from Bhatia [16].	38
4.3	Snapshots of a skateboarder performing a SO manoeuvre [17].	38
5.1	A basic description of the skateboard-skateboarder system and the identified problems under investigation.	40
5.2	The two ball models used to demonstrate the elastic tail and ground collision (A) and the inelastic wheel on ground collision (B).	41

5.3	The skateboard model used in all stages of development, described in terms of its physical properties (A), and the chosen generalized coordinates and forces (B).	43
5.4	An illustration of the auxiliary variables chosen for the skateboard model.	44
5.5	Plot of the y-position of the bouncing ball against time showing that as the coefficient of restitution is decreased, the ball loses more energy at impact and subsequently bounces to a lower height.	45
5.6	The conventions used for the skateboard model to model the elastic collision between the skateboard tail and the ground, or the "pop".	46
5.7	The test results of dropping the ball from varying heights using the contact-implicit method. These results are inelastic by nature.	48
5.8	The ball-skateboard model used to develop the theory for the reaction force between the skateboard and the ball.	49
5.9	Snapshots of the animation of the skateboard-ball test with the corresponding plots of the position of the ball (black), the GRFs on the skateboard (blue and purple) and the reaction force from the skateboard on the ball (red) showing that the contacts are behaving as expected.	50
5.10	A simple diagram of the inertial and skateboard reference frames for the ball-skateboard model. The skateboard frame coordinates are shown in green and the inertial coordinates in black.	51
5.11	The ball-skateboard model with the friction force, ${}^bF_x^s$ and the perpendicular distance between the ball and the skateboard in the skateboard frame, ϕ , added.	52
5.12	Snapshots of the dropping ball test with the corresponding plots of the position and tangential velocity of the ball (black), the GRFs (blue and purple), the skateboard reaction force on the ball (red) and the friction force between the skateboard and the ball (orange) showing that all the contacts are behaving as expected.	55
5.13	The results of the ball-ground drop test showing the simulated results and trajectories of the low-step and high-step.	57
5.14	Stages of development of the skateboard-skateboarder model used to generate the ollie manoeuvre using trajectory optimization.	58

5.15 Design 1: the skateboarder is modelled as applied forces on the skateboard acting in the inertial reference frame. The positions of the applied forces are fixed at the nose and tail of the skateboard.	60
5.16 The solved results for the first design, showing the visual simulation results and force profiles.	63
5.17 Design 2: the skateboard-skateboarder system is modelled as applied forces on the skateboard acting in the skateboard reference frame which are constrained to move along the length of the skateboard.	65
5.18 The solved results for the second design, showing the visual simulation results and force profiles.	66
5.19 The dimensions and mass conventions of design 3.	69
5.20 The coordinates and actuators of the monopods used in design 3 to model the skateboarder. The positions of the front and back feet are shown in pink, and the hard-stop reaction forces in the prismatic joints are shown in green.	69
5.21 An illustration of the monopods' feet and the foot-deck contact: the positions of the feet are shown in pink; the position of the feet in the skateboard frame is shown in green; the expected position of contact of the foot on the deck is shown in yellow; and the foot deck reaction forces are shown in red.	71
5.22 The simulated results of design 3 showing snapshots of the system performing the ollie, and the corresponding force and torque profiles.	77
5.23 The coordinates and actuators of the final design - a biped model with a torso, pelvis and two legs.	81
5.24 The dimensions and mass conventions of the final design.	82
5.25 A simple illustration of the formulation of the step-up and step-down ground functions.	84
6.1 The simulated trajectory of the modelled skateboard-skateboarder system performing a 0.5m SO manoeuvre given in four node intervals.	95

6.2	The simulated force profile of the SO manoeuvre showing the foot-deck and wheel-ground reaction forces, the applied force at the prismatic joint and the applied torques.	95
6.3	The simulated force profile of the RO manoeuvre showing the foot-deck and wheel-ground reaction forces, the applied forces at the prismatic joint and the applied torques.	96
6.4	The simulated force profile of the RO manoeuvre showing the foot-deck and wheel-ground reaction forces, the applied forces at the prismatic joint and the applied torques.	96
6.5	The simulated trajectory of the modelled skateboard-skateboarder system performing an OD manoeuvre from a $0.36m$ step, given in four node intervals.	97
6.6	The simulated force profile of the $0.36m$ OD manoeuvre showing the foot-deck and wheel-ground reaction forces, the applied forces at the prismatic joint and the applied torques.	97
7.1	A comparison of the SO simulation results to snapshots of a skateboarder performing an SO. On a high level, the simulated results appear to replicate the ollie trajectory.	101
7.2	A comparison of the observed trajectory provided by Bhatia [16] and the simulated trajectory of the RO manoeuvre.	102
7.3	The RO simulation results from the study conducted by Kolev [14]. The skateboarder's legs were fixed to the skateboard and the upper body was modelled as a rigid-body. The arms were drawn for aesthetic appeal.	102
7.4	A comparison of the simulated RO take-off GRF profile to the OU take-off GRF profiles recorded in literature [2], with a three-point moving average shown in blue.	104
7.5	A comparison of the simulated OD landing GRF profile to the OD landing GRF profiles recorded in literature [2], with a three-point moving average shown in blue.	105
7.6	Plots of the position of the front foot relative to the skateboard and the foot-deck reaction force during landing. The foot is in contact with the skateboard for $0.515s < t < 0.535s$	105

7.7	A comparison of the recorded GRF profile for a kickflip [?] to the simulated RO GRF profile.	106
7.8	The real-life skateboarder lands on the ground with his feet already on the skateboard, whereas the biped lands on the skateboard once the skateboard has already made contact with the ground.	107
7.9	The simulated trajectory of the high SO reaching a 1.0m apex. It can be seen that the biped tucks its legs in.	107
9.1	A model of a biped with a torso and arms proposed for future development of the skateboard model.	110
9.2	Simulated results of the biped model proposed for future works performing a 0.5m SO manoeuvre.	111
9.3	The pop-angle of the skateboard is the angle at which the skateboard nose and tail are set at relative to the deck [18].	111

List of Tables

2.1	Summary of the results of previous studies focused on the VGRFs experienced by the skateboard upon take-off and landing for various ollie manoeuvres expressed in terms of BW.	11
5.1	The variable bounds for design 1. S=100N.	61
5.2	The path constraints for designs 1 and 2.	62
5.3	The variable bounds for design 2. S=100N.	65
5.4	The chosen variable values of the monopod model.	69
5.5	The variable bounds for design 3. BW=196N.	74
5.6	The path constraints for design 3.	76
5.7	The chosen variable values of the biped model, based on the study by Plagenhoef et al. [19].	83
5.8	The variable bounds for the final design. BW=716N.	86
5.9	The path constraints for the SO manoeuvre.	89
5.10	The path constraints for the RO manoeuvre.	90
5.11	The path constraints for the OD manoeuvre.	91
5.12	The path constraints for the OU manoeuvre.	92
6.1	A summary of the recorded GRFs from the simulated SO, RO and OD manoeuvres, expressed in terms of BW.	94
7.1	A comparison of the peak GRF data from literature and the simulated results. The GRFs are expressed in terms of BW.	103

Chapter 1

Introduction

1.1 Background to the Study

Skateboarding began in the late 1940's as a way for surfers in California to "surf the streets" when the waves were flat [20]. Since then, the sport has rapidly increased in popularity on both an amateur and professional level, transcending age and gender boundaries, with an estimate of 11.08 million participants in 2009, and a market value of \$4.8 billion [21].

At a professional level, skateboarding is an established global entertainment powerhouse. Skateboarding competitions range from small technical tricks in skateboarding arenas, to extreme manoeuvres hosted in the X-Games and the Nitro World Games involving large ramps and "big-air". One of the more well-known extreme manoeuvres is the "900" which professional skateboarder Tony Hawk landed for the first time in 1999, completing two and a half full rotations while airborne. Twenty short years later, in 2019, Mitchie Brusco landed a "1260" at the X-Games, a whole three and a half full rotations while airborne. The sport of skateboarding has a culture of continuing to push the boundaries of what is possible within the sport - going faster, getting more "air" and doing impossible tricks.

Skateboarding has not only grown in the number of participants, but also in its viewer base. In recognition of the competitive level and global interest of the sport, skateboarding will make its debut at the 2020 Tokyo Summer Olympic Games, where the sport will involve both male and female competitions in "park" and "street" events.

Stripping back all these impressive tricks, big jumps and competitions, we have the fundamental manoeuvre in skateboarding, the ollie, named after Alan Gelfand (nicknamed "Ollie") who in 1978 invented the revolutionary manoeuvre [20]. The basics of the manoeuvre entails snapping the tail of the skateboard into the ground while jumping, propelling both the skateboarder and skateboard into the air, leveling the skateboard in the air, and then landing back on the skateboard. This manoeuvre forms the basis for almost all off-ground tricks in skateboarding.

In skateboarding, injury prevention has been a topic of focus for many years. Understanding the factors which cause injuries is highly desirable for skateboarders. This introduces a field of immense and growing interest to sports people and scientists alike - biomechanics. Understanding and simulating the biomechanics of human motion is playing

an increasingly important role in understanding motion, and, in its application to sport, improving performance and injury prevention strategies.

The sport of skateboarding has become a global phenomenon, large enough to feature at the Olympics. The tricks in the sport contain intricate manoeuvres and interactions with the external environment. However, despite the increased focus on studies into sports and other aspects of human motion using simulation, a functional skateboard-skateboarder system that can represent the unscheduled interactions between the skateboarder, skateboard and the ground is yet to have been developed.

1.2 Objectives of this Study

The aim of this study is to apply the principles of biomechanics to develop a mathematical model for a skateboard and skateboarder that, through the application of trajectory optimization, has the required complexity to replicate the characteristics of the ollie manoeuvre. The chosen characteristics of the manoeuvre are the observed motion of the model, the external forces experience by the skateboard, and most importantly, the various unscheduled contacts during the manoeuvre. The purpose of attempting to replicate the ollie manoeuvre is to develop a simulation tool which can be used in further biomechanics related research to understand the forces and torques experienced and applied by the skateboarder in completing the ollie manoeuvre.

It has been proven that understanding and quantifying the biomechanics of a specific motion or manoeuvre is a useful tool for understanding the causes of injuries associated with the manoeuvre [22], and for identifying factors which may improve the performance of the manoeuvre [23]. Thus, the outcome of this study could be used to develop the understanding of the biomechanics and clinical aspects of the ollie manoeuvre, with applications in injury identification and prevention, and performance enhancement.

Furthermore, current literature is sparse regarding unscheduled contacts between two bodies where the point of contact is changing. Thus, since the skateboarder system has a variety of different contacts, this study aims to explore possible solutions to modeling these contacts.

The problem of replicating the ollie using trajectory optimization has been attempted previously by Kolev [14], however, the results of the study by Kolev were unsatisfactory for the following reasons:

- The position of the skateboarder's feet were fixed to the skateboard. This meant

that the skateboarder model could not move or “slide” its feet along the skateboard.

- The collision between the skateboard tail and the ground was not adequately explained or modeled.
- The only ollie manoeuvre considered was the rolling ollie - the ollie manoeuvre is performed on the ground while the skateboard is in motion. Ollie manoeuvres are typically performed onto and off of objects, as well as on the ground.

It is desirable to address these problems, and thus, generate results which more accurately replicate the real ollie manoeuvre. Therefore, drawing on the previous study by Kolev, the aim of this project is hereby to:

1. Decompose the ollie manoeuvre into phases of motion. This can be used to derive the discontinuous dynamics for the models involved in the manoeuvre.
2. Develop a skateboard model that is capable of encapsulating the key dynamics of a skateboard, and a skateboarder model that adequately replicates the essential dynamics of a skateboarder.
3. Choose and implement a method for modeling the various contacts during the skateboarding manoeuvre. The identified contacts are as follows:
 - (a) The contact between the skateboard wheels and the ground - this must be unscheduled and inelastic, involving a ground reaction force and friction.
 - (b) The contact between the skateboarder’s feet and the skateboard - this must be unscheduled and inelastic, involving a reaction force and friction, and the contact point must be able to vary along the length of the skateboard deck.
 - (c) The contact between the skateboard tail and the ground - this may be scheduled, and should be elastic.
4. Conclude whether, using trajectory optimization, the skateboard-skateboarder system’s motion was able to replicated four similar ollie manoeuvres: the standing ollie (SO), rolling ollie (RO), ollie up (OU) and ollie down (OD) manoeuvres.

1.3 Scope and Limitations

This study will go insofar as to develop a mathematical model that, using trajectory optimization, will be capable of performing a variety of ollie manoeuvres. Other methods

for simulating motion exist such as inverse simulation [24], predictive dynamics [25] and using genetic algorithms to generate optimal trajectories [26]. However, this study will be limited to trajectory optimization using nonlinear programming.

The dynamics of the skateboard-skateboarder system will be constrained to the two-dimensional coronal plane as shown in 1.1. Choosing this plane will allow the model to perform the ollie manoeuvre by translating in the global X and Y directions and rotating about the Z-axis, according to the coordinate conventions shown in 1.1. It has been shown that this restriction is still sufficient to replicate a simple ollie [14].

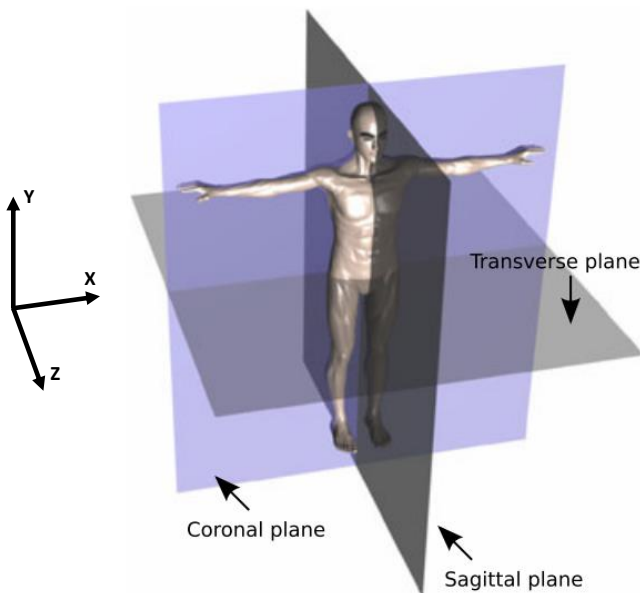


Figure 1.1: The ollie manoeuvre will be constrained to the XY-plane with the skateboarder model restricted to the coronal plane. Adapted from [1].

The skateboarder model can only interact with the skateboard and not the ground, thus, the skateboarder cannot propel the skateboard forward by pushing off the ground. This ensures that this study remains focused on the interaction between the skateboarder and skateboard, only.

A major limitation of this study, and of all trajectory optimization problems, is how computationally intensive the model and the trajectory optimization problem can be. A model that is extremely complex, or a transcription method which uses a high order polynomial or a large number of trajectory nodes will be highly computationally intensive. This leads to extensive solve times, or even cases where the machine does not have the computational power to solve the problem. Therefore, the trajectory optimization problem posed will be simple enough to solve on a middle-range laptop. This is another justification for choosing to model the system in the coronal-plane exclusively.

Finally, since the project was a final year undergraduate project, the time constraint

given to the project was approximately 12 weeks. Upon reaching the time limit, no further development was possible.

1.4 Report Outline

Due to this project's exploratory nature, the aim of the project could not be clearly defined until the capabilities of the skateboard-skateboarder system and the trajectory optimization problem became known through iterative stages of development. Therefore, since the nature of this study is iterative and developmental by nature, the report structure reflects this.

Firstly, the typical literature review and theory of development sections are combined to investigate the science of the ollie, modeling and trajectory optimization. This includes defining the motion of the ollie manoeuvre and the physical properties and dynamics of the skateboard. Then, techniques for modeling multi-body systems are introduced. An overview of trajectory optimization is then given in its application to biomechanics.

The development plan for the skateboard-skateboarder model is then outlined in the methodology chapter, along with an introduction to the formulation of the trajectory optimization problem. The means by which the results of this study would be validated are then presented.

In an extensive design chapter, the important aspects of the skateboard-skateboarder system, focusing on the contacts, are developed using simple examples. Drawing on these simple examples, the skateboarder model is developed in conjunction with the ollie manoeuvre and the trajectory optimization problem.

In the results, discussion and conclusion chapters, the results from the SO, RO, OU and OD manoeuvres are presented, analysed and discussed. Finally, recommendations are given for future work and development on this project.

Chapter 2

Science of the Ollie

The most important aspect of this study is to replicate the ollie manoeuvre using modeling and trajectory optimization. In order to accurately model the skateboarder and skateboard, and the ollie manoeuvre itself, the manoeuvre needs to be understood in terms of the discrete phases and general properties of the motion, and the limits to the manoeuvre. These aspects are not necessarily described in scientific literature, and thus, the sources of information were often relevant skateboarding websites and articles, and videos of skateboarding.

2.1 Understanding the Ollie

The ollie is a fundamental skateboarding manoeuvre that can be performed while stationary or moving, onto or off of objects. At a technical level, the ollie motion is well understood and described [2][4][27]. Using the diagram provided by [2] shown in Figure 2.1, the ollie can be divided into the following phases:

- A. **Crouching:** The skateboarder places his back foot on the tail of the skateboard and his front foot roughly midway down the skateboard, ensuring his stance is still balanced. His knees are bent to prepare to rapidly jump upwards.
- B. **Pre-“pop”:** The skateboarder accelerates himself upwards by extending his legs and pushing down with his back foot to accelerate the tail of the skateboard downwards. This causes the board to pivot about the back wheel in a counter-clockwise direction. The skateboarder can raise his arms to get additional upward acceleration.
- C. **The “pop”:** The tail of the skateboard is slammed into the ground while the skateboarder lifts his back foot from the skateboard. When the tail strikes the ground, the tail bounces off the ground, propelling the skateboard into the air. Simultaneously, the skateboarder slides his front foot forward along the skateboard, using the friction between the foot and the skateboard to “pull” the board into the air.
- D. **Airborne:** The skateboarder and skateboard are in the air. The skateboarder continues to slide his front foot forward and uses their back foot to level the skateboard.

board out in the air. The skateboarder can tuck their legs in to achieve maximum skateboard height - this will be discussed further below.

- E. **Landing:** The skateboarder aims to position his front and back feet on the wheel bearings of the skateboard. The skateboarder bends his knees upon landing to cushion his landing, while using his arms to keep balanced. Both wheels are on the ground.
- F. **Post-Landing** The skateboarder has both feet on the bearings of the wheels and has extended his legs to a comfortable height. Both the wheels of the skateboard are on the ground and the skateboarder is standing still. The skateboarder and skateboard could be described as being in steady-state.

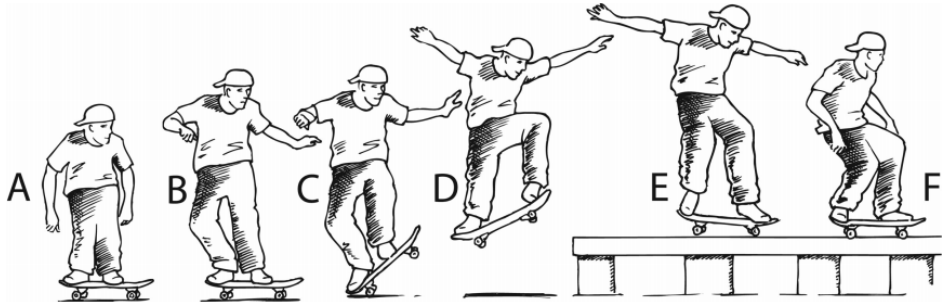


Figure 2.1: The discrete phases of a skateboarder completing the OU manoeuvre [2].

Upon watching videos of skateboarders performing the ollie in slow motion [28], it was found that the average time it takes for a skateboarder to complete the manoeuvre - from both wheels on the ground before the “pop” to both wheels on the ground after the landing - was approximately 0.6s. This is an important consideration for creating a feasible trajectory for the skateboard model.

In 2011, the world record for the highest off-ground ollie was set by Aldrin Garcia at 114.3cm [29]. The ollie, shown in Figure 2.2, was performed over a rigid bar and the height was measured by the clearance over the bar at the apex. Although this paper does not aim to maximize the height an ollie can achieve, it is important to recognize the maximum feasible height that a skateboarder can ollie. Another interesting aspect of this ollie manoeuvre worth noting is how Garcia tucks his legs into his body to allow the board to reach maximum height. This provides insight into the manner in which the skateboarder model can increase board-clearance height.



Figure 2.2: Aldrin Garcia reaching the official world record off ground ollie height of 114.3cm in 2011. Garcia tucks his legs in to achieve maximum board height [3].

2.2 Dynamics of the Ollie

Qualitative, high-level descriptions of the forces involved in the ollie manoeuvre have been described by the Exploratorium [4] and Batia [16]. These descriptions are written by skateboarders, and thus, their insight is valuable. However, their scientific credibility is up to question. For one, these descriptions do not adequately describe the nature of the friction force between the foot and the skateboard.



Figure 2.3: Quantitative description of the forces involved in four phases of the ollie manoeuvre. The red arrows represent applied forces by the skateboarder's feet on the board, the blue arrows represent ground reaction forces on the skateboard, and the black arrows represents the weight of the skateboard [4].

Kolev [14] described the forces qualitatively and also, through the application of trajectory optimization, quantitatively. However, similarly to Batia, Kolev does not adequately consider the friction force between the skateboarder's foot and the skateboard. The underlying principles from all three of these descriptions of the forces involved in the ollie manoeuvre will be considered when designing the models for the skateboarder and skateboard.

In response to the growing popularity and participation of skateboarding globally, clinicians have published papers detailing the musculoskeletal injuries associated with the sport [30][31]. However, studies detailing the biomechanical factors that may be causing these injuries are still few and far between. To date, two studies have comprehensively investigated, measured and quantified the forces involved in performing the ollie manoeuvre [2][32].

The first study by Frederick et al. [2] quantified the vertical ground reaction forces (VGRF) experienced by a force plate during the take-off of an OU manoeuvre onto a 45.7cm high platform, and during the landing of an OD manoeuvre from the same platform. The seven participants in the study were males of mean body mass 72.7kg ($BW = 713 \pm 83\text{N}$) between the ages of 17 and 25. The study found that the mean impulsive peak VGRF for the OU manoeuvre was 2.2 ± 0.22 BW which occurred upon slamming the tail of the board into the ground to propel the skateboard and skateboarder into the air. The mean peak VGRF for the OD manoeuvre was higher, at 4.74 ± 0.46 BW, occurring in the first 30-80ms of landing. The VGRF profile of the results for a single participant and all participants is shown in Figure 2.4.

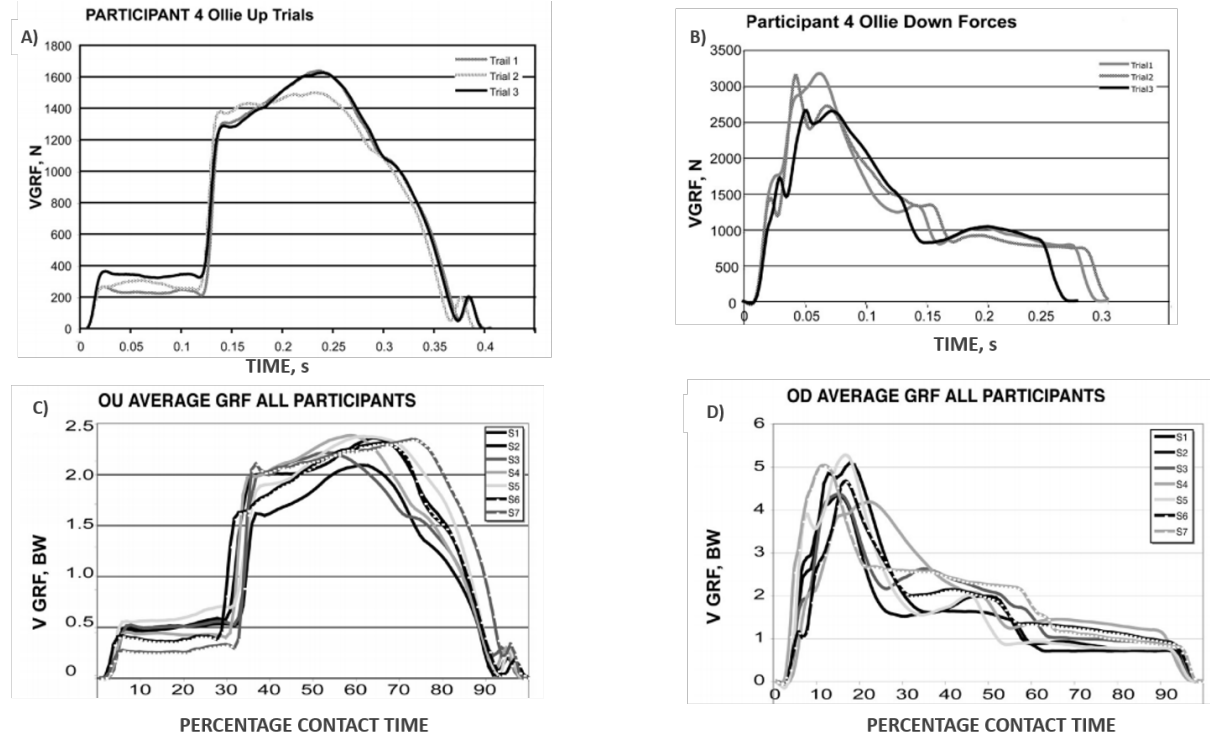


Figure 2.4: A VGRF profile from the study conducted by Frederick et al. [2] for an individual participant completing an (A) OU and (B) OD manoeuvre, and all participants completing an (C) OU and (D) OD manoeuvre. Adapted from [2].

This study by Frederick et al. only quantified two scenarios within the ollie manoeuvre - the take-off and landing of OU and OD manoeuvres respectively - and thus, Leuchanka et al. furthered this study to quantify the biomechanics of the ollie more completely [32].

In this study, the VGRFs of the OD from a height of 36 cm was again quantified, but two more tests were conducted: the standing ollie (SO) and rolling ollie (RO). Furthermore, the study utilized in-sole pressure sensors rather than force plates to measure the forces at take-off and landing. The study found that the mean peak VGRFs at take-off for the SO, RO and OD were 2.47 ± 0.38 BW, 2.55 ± 0.51 BW and 2.34 ± 0.32 BW respectively. On the landing, the peak VGRFs for the SO, RO and OD were 2.40 ± 0.33 BW, 2.71 ± 0.23 BW, and 3.15 ± 0.51 BW respectively.

Determan et al., also recognizing the scarcity of studies into the biomechanics of skateboarding, investigated another common skateboarding manoeuvre, the "Kickflip" [?]. The Kickflip involves an ollie-like jump with an added rotation of the skateboard along its long axis while the skateboard is airborne. The study involved seven skateboarders of mass 75.1 ± 11.40 kg performing a standing Kickflip over a force plate to measure the VGRFs experienced by the skateboard. Due to the similarities in the landing and take-off of the ollie and the kickflip manoeuvres, the results of this study by Determan et al. are relevant to this paper. The mean peak VGRFs recorded at take-off and landing were 2.05 ± 0.17 BW and 4.61 ± 1.19 BW respectively. It should be noted that the average jump height was 25.8 ± 9.1 cm with flight duration of 448 ± 30 ms between take-off and landing. The observed VGRF profile for a single participant is shown in Figure 2.5.

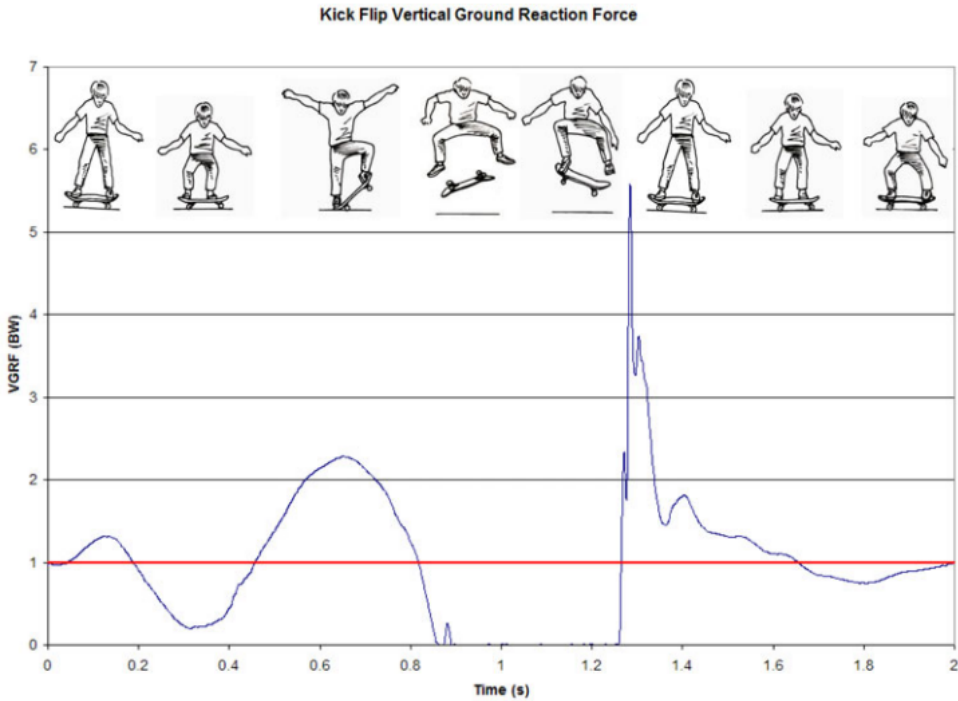


Figure 2.5: The VGRF profile for the kickflip corresponding with the phases of the kickflip [?].

The VGRF results from the three studies are summarized in Table 2.1. The results of the OD landing tests conducted by Leuchanka et al. [32] and Frederick et al. [2] vary by approximately 1 BW, which may be due to the fact that the platform used by Leuchanka

et al. was 4cm higher. In the SO tests, the take-off and landing results vary significantly between the study by Leuchanka et al. and Determan et al., which may be as a result of the studies analysing different skateboarding tricks. A limitation of this data set is that the peak VGRFs for the OU manoeuvre have only been quantified for take-off, and that the RO has only been quantified in one study.

Table 2.1: Summary of the results of previous studies focused on the VGRFs experienced by the skateboard upon take-off and landing for various ollie manoeuvres expressed in terms of BW.

	Study 1		Study 2		Study 3	
	Take-off	Landing	Take-off	Landing	Take-off	Landing
OU	2.2 ± 0.22	-	-	-	-	-
OD	-	4.74 ± 0.46	2.34 ± 0.32	3.15 ± 0.51	-	-
SO	-	-	2.47 ± 0.38	2.40 ± 0.33	2.05 ± 0.17	4.61 ± 1.19
RO	-	-	2.55 ± 0.51	2.71 ± 0.23	-	-

The VGRF profiles, shown in Figures 2.4 and 2.5, and the peak VGRF results, summarized in Table 2.1, will form the basis for the expected results that should be replicated by the trajectory of the model in this study. However, it would be misguided to not acknowledge that these tests were conducted by individuals of different masses and from differing heights. Thus, the results should be used as a guideline, but the comparison should account for these factors.

2.3 Physical Properties of the Skateboard

The skateboard, as might be guessed by the name skateboarding, is the essential piece of equipment used in the sport of skateboarding. The skateboard is made of a board or “deck” covered on the top side with “grip tape”, four wheels, and two metal “trucks” which are attached to the wheels using ball bearings. The deck is typically made of Maple wood with a polyurethane coating. The grip tape is a rough paper material, similar to that of fine sandpaper. The importance of the grip tape is that it provides insight into the maximum friction force between the front shoe and the skateboard used in the sliding motion described previously.

The convention for skateboard deck sizes are given in proportion to the width of the board. It is recommended that adults use 19 – 21cm decks similar to the skateboard shown in Figure 2.6 which is a 7.75 inch deck (19.7cm) [33]. Considering all the components of the complete skateboard mentioned previously, the mass of all the components comes to approximately 2kg. This total mass for the skateboard was confirmed upon weighing the author’s skateboard.

7.75

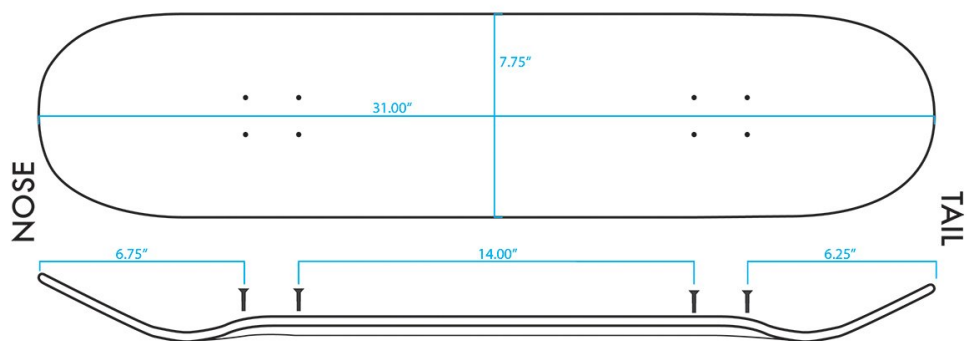


Figure 2.6: The dimensions of a full sized 7.75 inch skateboard showing the width, length, wheelbase, nose and tail measurements [5].

Chapter 3

Studying Motion with Trajectory Optimization

This chapter describes the essential concepts and theory required to perform the modeling of dynamic systems and to formulate and solve trajectory optimization problems. Examples of the application of the theory in current literature are also presented.

3.1 An Overview of Trajectory Optimization

Trajectory optimization is the process of obtaining locally optimal finite-time trajectories for both linear and nonlinear dynamic systems [13]. For any person that is new to this field, understanding the terminology and concepts of trajectory optimization is not only daunting, but extremely difficult. Thus, the aim of this overview is to describe trajectory optimization in a way which is understandable and applicable to this study.

3.1.1 The Trajectory Optimization Problem

The trajectory optimization problem aims to solve for a finite-time control trajectory, $u(t)$, $\forall t \in [0, T]$, given a dynamic system, $\dot{x} = f(x, u)$, while minimizing a cost function or objective function defined in terms of the decision variables of the system which are generally the control trajectories, \mathbf{u} , and state trajectories, \mathbf{x} [13][34]. Put simply by Kelly, [12], “A trajectory optimization problem seeks to find the trajectory for some dynamical system that satisfies some set of constraints while minimizing some cost functional.”

Before we dive any further into trajectory optimization, it is important to understand some of the terminology that will be used, as described by Kelly [34]:

Decision variables: variables which the optimizer can adjust to converge to an optimal solution.

State variables: variables which are defined through the 2nd order integration of the system dynamics using the chosen integration scheme.

Control variables: variables which appear algebraically in the dynamics equation of the system.

Transcription: the process of converting a optimal control problem into a constrained nonlinear program problem.

Back to the explanation, the general framework for a trajectory optimization problem is as follows [12]:

$$\text{Optimal Trajectory: } \{\mathbf{x}^*(t), \mathbf{u}^*(t)\} \quad (3.1)$$

$$\text{System Dynamics: } \dot{\mathbf{x}} = f(t, \mathbf{x}, \mathbf{u}) \quad (3.2)$$

$$\text{Constraints: } \mathbf{c}_{min} < \mathbf{c}(t, \mathbf{x}, \mathbf{u}) < \mathbf{c}_{max} \quad (3.3)$$

$$\text{Boundary Conditions: } \mathbf{b}_{min} < \mathbf{b}(t_0, \mathbf{x}_0, t_f, \mathbf{x}_f) < \mathbf{b}_{max} \quad (3.4)$$

$$\text{Cost Function: } J = \phi(t_0, \mathbf{x}_0, t_f, \mathbf{x}_f) + \int_{t_0}^{t_f} g(t, \mathbf{x}, \mathbf{u}) dt \quad (3.5)$$

The aspects of this framework will now be individually explained.

3.1.2 The Optimal Trajectory

The optimal trajectory refers to the discrete values of the state and control trajectories, \mathbf{x} and \mathbf{u} , which satisfy the constraints posed on the system while minimizing the objective function. It should be noted that the term “optimal” is dependent on the decision variables included in the formulated objective function. In the case of the skateboard-skateboarder system, the optimal state trajectories will be the variables describing the orientation and spacial positioning of the system, and the optimal control trajectories will include the forces and torques applied to the system in order to perform the ollie.

3.1.3 Constraints

The trajectory optimization problem is subject to a set of nonlinear or linear constraints and limits described in equations (3.6) - (3.13) [34]. The first constraint is the system dynamics, defined by the equations of motion of the system. This constraint simply ensures that the state trajectory obeys the dynamics of the system.

$$\text{System Dynamics: } \dot{\mathbf{x}} = f(t, \mathbf{x}(t), \mathbf{u}(t)) \quad (3.6)$$

The path constraints impose restrictions on the trajectory of the system.

$$\text{Path Constraints: } h(t, \mathbf{x}(t), \mathbf{u}(t)) \leq 0 \quad (3.7)$$

Boundary constraints enforce restrictions on the initial and final states of the system.

$$\text{Boundary Constraints: } g(t_0, t_F, \mathbf{x}(t_0), \mathbf{x}(t_F)) \leq 0 \quad (3.8)$$

Path bounds on state (3.9) and path bounds on control (3.9) are limits imposed on the discrete state or control variables.

$$\text{Path Bound on State: } x_{low} \leq x(t) \leq x_{upp} \quad (3.9)$$

$$\text{Path Bound on Control: } u_{low} \leq u(t) \leq u_{upp} \quad (3.10)$$

Finally, bounds can be included on the initial and final time and state. These are called bounds on initial and final time (3.11) and bounds on initial and final state (3.11,3.13).

$$\text{Bounds on Time: } t_{low} \leq t_0 \leq t_F \leq t_{upp} \quad (3.11)$$

$$\text{Bounds on Initial State: } x_{0,low} \leq x(t_0) \leq x_{0,upp} \quad (3.12)$$

$$\text{Bounds on Final State: } x_{F,low} \leq x(t_F) \leq x_{F,upp} \quad (3.13)$$

3.1.4 The Objective Function

The objective function defines some function of the decision variables which have been chosen to be minimized or maximized through the optimization process [34]. The objective function generally contains two terms, the boundary objective $J(\cdot)$, and a path integral along the entire trajectory $w(\cdot)$. The general form of the objective function is [34]:

$$\min_{t_0, t_F, \mathbf{x}, \mathbf{y}} J(t_0, t_F, \mathbf{x}(t_0), \mathbf{x}(t_F)) + \int_{t_0}^{t_F} w(\tau, \mathbf{x}(\tau), \mathbf{u}(\tau)) d\tau \quad (3.14)$$

Two commonly used objective functions for system with continuous dynamics are the minimum work objective function and minimum force objective function [34].

$$\text{Minimum force squared: } \min_{u, x, v} \int_0^1 u^2(\tau) d\tau \quad (3.15)$$

$$\text{Minimum absolute work: } \min_{u, x, v} \int_0^1 |u(\tau)v(\tau)| d\tau \quad (3.16)$$

It is important to note that there is no “best” objective function for a specific application, however, the objective function should be chosen to suit the problem and the desired outcome of the problem.

3.2 Modeling Dynamic Systems

In biomechanics, the biological systems vary from simple single body systems, to complex multi-body systems, depending on the complexity of the biological system under investigation. There are multiple methods and considerations that should be made when modeling these systems. These will be explored below.

3.2.1 Coordinates

Coordinates Systems

The concept of coordinate systems and reference frames are well explained by Diebel [6]. There are two coordinate systems: the world or inertial coordinate system and the body-fixed coordinate system. The world coordinate system is fixed in the inertial space, whereas the body-fixed coordinate system is rigidly attached to a body in the system. For the sake of ease of reading, these will be termed the inertial frame and the body frame.

Coordinate Frames and Transformations

In order to transform between coordinates systems, rotational matrices can be used. A rotation matrix is a matrix whose multiplication with a vector rotates the vector while preserving its length. Rotational matrices can be used to perform coordinate rotations, whereby a coordinate system is rotated into another. Enumerating a rotation about the z-axis with 3, the coordinate rotation by angle α about the z-axis is:

$$R_3(\alpha) = \begin{bmatrix} \cos(\alpha) & \sin(\alpha) & 0 \\ -\sin(\alpha) & \cos(\alpha) & 0 \\ 0 & 0 & 1 \end{bmatrix} \quad (3.17)$$

This is also called a direction cosine matrix. Given the world axes coordinates $x_w = [x, y, 0]^\top$ and the body axes coordinates $x_b = [x', y', 0]^\top$, a rotation from the inertial frame into the body frame by angle α is defined as:

$$x_b = R_3(\alpha)x_w \quad (3.18)$$

And a rotation from the body frame into the inertial frame is:

$$x_w = R_3(\alpha)^{-1}x_b \quad (3.19)$$

Two important properties of rotational matrices that should now be considered are:

$$\det(R) = \pm 1 \quad (3.20)$$

$$R^{-1} = R^\top \quad (3.21)$$

Applying these properties, equation (3.19) can be re-written as:

$$x_w = R_3(\alpha)^\top x_b \quad (3.22)$$

An example of a coordinate rotation from the inertial frame to the body frame by angle α is shown in Figure 3.1.

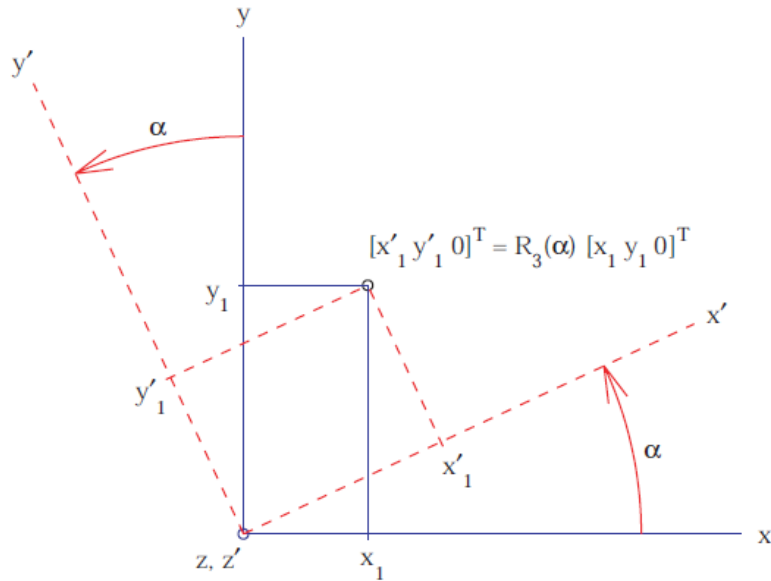


Figure 3.1: An illustration of a simple coordinate transformation from the inertial frame to the body frame [6].

Similarly, the position of a body in space can be described in terms of the inertial frame or the body frame. If the position of a body in the inertial frame is denoted p^0 , the position of the body in the body frame is denoted p^1 , and the coordinate rotation matrix rotating the world frame into the body frame is denoted as R_0^1 , the following relates the relative positions:

$$p^1 = R_0^1 p^0 \quad (3.23)$$

Therefore, using coordinate transformations, the position, velocity, or acceleration of one body can be expressed relative to another body in the system.

Generalized and Maximal Coordinates

Two concepts which are useful in defining the coordinate system which is used to describe the system's dynamics are generalized coordinates and maximal coordinates. These concepts are well described by Shield [7]. The generalized coordinates method uses the least amount of variables possible to capture the dynamics of a system completely. This method often defines the coordinates of one body relative to another body in the system. The maximal approach defines each member of the system individually in terms of the coordinates that describe its dynamics. The illustration below shown in Figure 3.2, provided by Shield [7] demonstrates both of these concepts for a double-link pendulum.

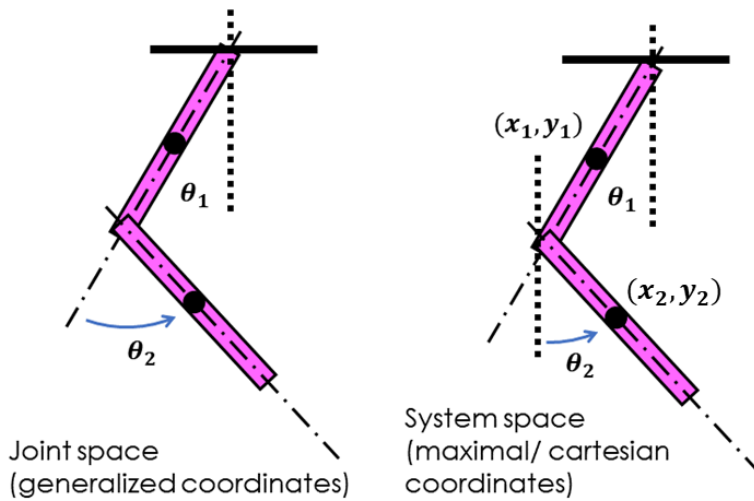


Figure 3.2: An example of using generalized coordinates (left) and maximal coordinates (right) to describe the dynamics of a double-link pendulum [7].

The benefits of using generalized coordinates is that the constraints of the system are simpler to define. For example, in Figure 3.2, if the double-link pendulum represented a human leg, one could use generalized coordinates in the joint space to restrict the relative angle of the lower limb to $0 \leq \theta_2 \leq \pi$, whereas restricting the motion of the lower limb in system space would not be as trivial. Using maximal coordinates is desirable for long open-chain systems, as the equations of motion of the members in the chain remain relatively simple regardless of how long the chain is, whereas using the generalized coordinates approach for long open-chain systems leads to increasing complexity of the equations of motions for the members near to the end of the chain as the chain increases in length.

Templates and Anchors

The skateboard-skateboarder system consists of a skateboard and skateboarder (human). In order to develop system which can be optimized and solved, a model must be created for the system. A method first proposed by Full and Koditschek [8] and used by Patel [35] is that of templates and anchors. Full and Koditschek describe templates as the “simplest model (least number of variables and parameters) that exhibits a targeted behavior” [8], whereas anchors are more elaborate models encompassing morphological and physiological properties of the real-world system. The general concept is that organisms or physical bodies are complex and can be reduced to simpler models with fewer degrees of freedom while still achieving the desired motion of the model. The concept of templates and anchors is shown in Figure 3.3 with the example of legged land locomotion.

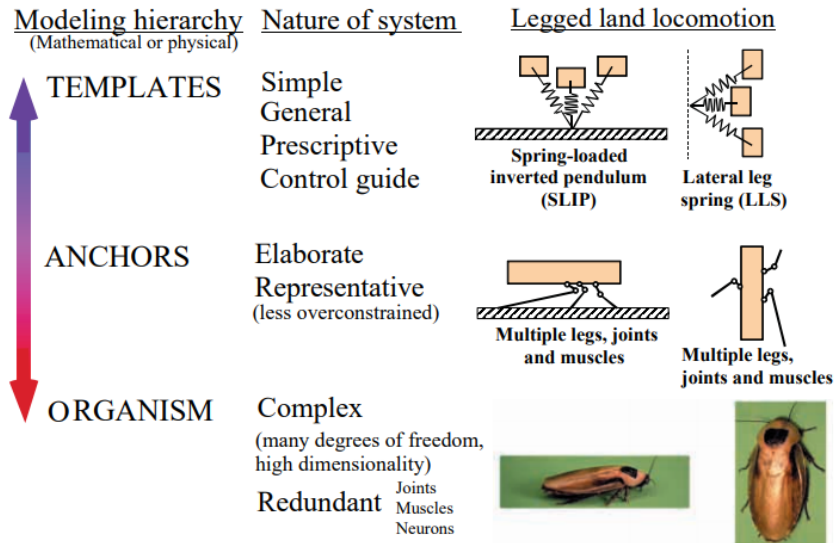


Figure 3.3: The concept of templates and anchors explained using the example of the cockroach’s legged land locomotion [8].

In his study of rapid maneuverability of the cheetah [35], Patel developed a template for a cheetah tail to test the implemented control systems on a reduced order robot model. This concept will be implemented in this project to develop the models of both the skateboard and the skateboarder to a level of complexity at which the targeted dynamics of the system are captured, while minimizing the order of the model to reduce computational intensity.

Humanoid Models

The skateboarder model needs to be able to encapsulate the key dynamics of a human, specifically, a human performing an ollie manoeuvre. Other than the study by Kolev [14],

there have been no studies into the biomechanics and the modeling of a skateboarder performing an ollie, or any other skateboarding manoeuvre in the coronal plane. Thus, a skateboarder modeled will have to be developed and tested in this study based on successful models that have been implemented in literature.

In a study into the factors that affect optimized simulation in a running jump for height [23], Wilson et al. used a planar torque activated eight-segment model to replicate the jumping motion of a human. This method involved modeling the system using rigid links which were activated at the joints by torques. Despite the success of this model in the application to high jump, this model is not directly applicable to the ollie manoeuvre since it is not posed in the coronal-plane. However, modeling the various extremities of the human body as rigid-links may be a useful approach to draw from in this study.

A common approach for designing simple human models for the application of understanding human locomotion is the spring-loaded inverted pendulum model (SLIP). This is often used as the template to describe a complex biological system [8]. Many simple modeling approaches are SLIP-variants, such as the approach used to model the human leg presented by Capi et al. [26]. This approach modelled the leg using a prismatic joint. A similar approach was used by Srinivasan et al. [36] in its application to creating a biped model that, through optimization, discovers walking and running. A prismatic joint is a connection between two rigid-bodies which allows linear sliding between the bodies. The joint can be actuated by a spring-dampener arrangement [26][36], or in simplistic cases, by internal forces and torques. Shield [7] describes a basic prismatic joint that can be used to model a leg in Figure 3.4.

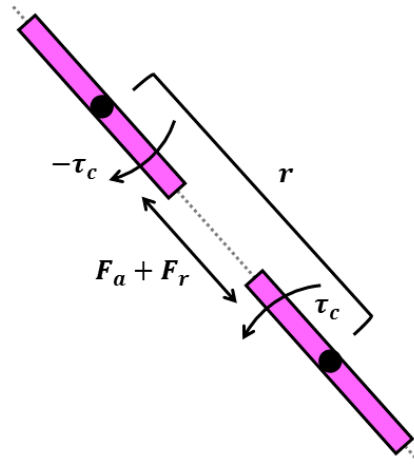


Figure 3.4: A simple prismatic joint with extension, r , an applied force, F_a , and a reaction force and torque, F_r and τ_c [7].

The advantage of using a prismatic joint to model simple human legs is that it decreases the degrees of freedom of the system while ensuring the key functionalities of the leg are

still captured. However, this approach may tend to oversimplify the model for the leg in applications where the system's motion is highly complex.

3.2.2 Skateboard Models

Modeling and deriving the dynamics of the skateboard with and without a rider has been an area of academic focus since as early as 1979 by Hubbard [37]. In order to derive the dynamics, physical mathematical models of the skateboard must first be created. Since 1979, this process of modelling and deriving the dynamics of the skateboard have been successfully implemented and expanded upon [9][10][11]. However, the focus of these papers is on the application of the dynamics on assessing the stability and steering of the skateboard.

Kuleshov et al. [9] defines the skateboard model in the global frame as shown in Figure 3.5. The model is defined in terms of the tilt angle, γ , the angle of rotation of the truck axles, δ_f and δ_r , the global position of the centre of mass of the board, X and Y , and the angle between the board centre line and the global X-axis, θ . The skateboarder is modelled as a rigid body fixed perpendicular to the board's centre of mass. This method for modelling the skateboard and skateboarder is common for [10][11].

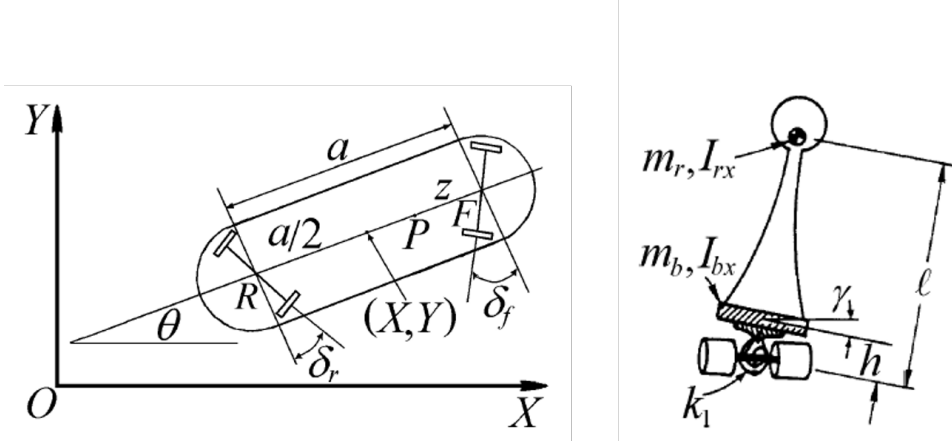


Figure 3.5: The skateboard model used in the study by Kuleshov et al. [9] similar to that of the other studies deriving the dynamics of the skateboard in the transverse plane [10][11].

Importantly, these papers only consider the motion of the skateboard in the transverse plane, whereas the scope of this research focuses on movement in the coronal plane exclusively. Therefore, however in depth this research may be, it provides no direct insight into the dynamics of the skateboard applicable in this study. However, considering the skateboard as a rigid-body may be an approach applicable to modeling the template of the skateboard.

Another key aspect of the dynamics of the skateboard performing an ollie that is not covered in current literature is that of the “pop” - when the skateboard tail strikes the ground. Therefore, based on the principles from current literature, this study will include modeling and deriving the dynamics of a simple skateboard model in the coronal plane, including the “pop”, from first principles.

3.2.3 Deriving the Equations of Motion

The Euler-Lagrange method can be used to derive the dynamics or equations of motion of a multi-body system defined using generalized coordinates. This method is well understood in its application to modeling mechanical systems [38][39] and has been successfully used to derive the dynamics of templates and anchors in previous biomechanical studies [35][14]. In order to use the method, a set of N generalized coordinates must be chosen to capture all the degrees of freedom of the multi-body system with the least number of variables:

$$\mathbf{q} = [q_1, \dots, q_N]^\top \quad (3.24)$$

where \mathbf{q} is the generalized coordinates vector and q_1, \dots, q_N is the set of the N generalized coordinates needed to completely describe the dynamics of the system. The first and second derivatives of the generalized coordinates are expressed as:

$$\dot{\mathbf{q}} = [\dot{q}_1, \dots, \dot{q}_N]^\top \quad (3.25)$$

$$\ddot{\mathbf{q}} = [\ddot{q}_1, \dots, \ddot{q}_N]^\top \quad (3.26)$$

Now, the position in the inertial frame of the i^{th} body’s centre of mass must be expressed in terms of the generalized coordinates.

$$\mathbf{r}_i = \begin{bmatrix} x_i(q) \\ y_i(q) \\ z_i(q) \end{bmatrix} \quad (3.27)$$

By taking the derivative of each position vector, the velocity vector for the i^{th} body, $\dot{\mathbf{r}}_i$, can be calculated:

$$\dot{\mathbf{r}}_i = \mathbf{J}(\mathbf{r}_i)\dot{\mathbf{q}} \quad (3.28)$$

where $\mathbf{J}(\mathbf{r}_i)$ is the Jacobian matrix of \mathbf{r}_i . Using the velocities of each body, the rotational and translational kinetic energy, $\mathbf{T}(\mathbf{q}, \dot{\mathbf{q}})$, and potential energy, $\mathbf{V}(\mathbf{q})$, of the i^{th} body in

the system can be expressed as:

$$T_i = \frac{1}{2}m_i(\dot{\mathbf{r}}_i)^\top \dot{\mathbf{r}}_i + \frac{1}{2}(\dot{\theta}_i)^\top I_i \dot{\theta}_i \quad (3.29)$$

$$V_i = m_i(\mathbf{g})^\top \mathbf{r}_i \quad (3.30)$$

With

$$\mathbf{g} = \begin{bmatrix} 0 \\ 0 \\ g \end{bmatrix} \quad (3.31)$$

where m_i and I_i describe the mass and moment of inertia of the i^{th} body respectively in the body frame, v_i , $\dot{\theta}_i$, and r_i describe the velocity, angular velocity and position, respectively of the i^{th} body's centre of mass in the inertial frame, and \mathbf{g} is the gravity vector expressed in the inertial frame. These can then be used to derive the Lagrangian, \mathcal{L} , using Lagrange's equations, written in vector form below:

$$\mathcal{L}(\mathbf{q}, \dot{\mathbf{q}}) = \mathbf{T}(\mathbf{q}, \dot{\mathbf{q}}) - \mathbf{V}(\mathbf{q}) \quad (3.32)$$

The non-conservative forces and torques must now be considered. Given m generalized forces, these are formulated as follows:

$$Q_i = \sum_{j=1}^m \mathbf{f}_j \cdot \frac{\partial \mathbf{r}_j}{\partial q_i} \quad (3.33)$$

where \mathbf{Q} is the generalized force vector containing the generalized forces for each generalized coordinate. Finally, the Lagrangian and the generalized forces are related as follows:

$$\frac{d}{dt} \frac{\partial \mathcal{L}}{\partial \dot{\mathbf{q}}} - \frac{\partial \mathcal{L}}{\partial \mathbf{q}} = \mathbf{Q} \quad (3.34)$$

The dynamics of the system can now be derived in terms of each generalized coordinate by solving for $\ddot{\mathbf{q}}$. Furthermore, equation 3.34 can be extended to include constraints and input forces:

$$\frac{d}{dt} \frac{\partial \mathcal{L}}{\partial \dot{\mathbf{q}}} - \frac{\partial \mathcal{L}}{\partial \mathbf{q}} = \mathbf{B}\boldsymbol{\tau} + \mathbf{Q} + \mathbf{A}^\top \boldsymbol{\lambda} \quad (3.35)$$

where \mathbf{B} is the input mapping matrix, $\boldsymbol{\tau}$ is the generalized input force vector, \mathbf{Q} is the generalized force vector, \mathbf{A} is the constraint Jacobian and $\boldsymbol{\lambda}$ is the constraint force vector.

Alternatively, the terms calculated above can be used to derive the dynamics of the

system in the manipulator form using the method described in [40].

$$\mathbf{M}\ddot{\mathbf{q}} + \mathbf{C}\dot{\mathbf{q}} + \mathbf{G} = \mathbf{B}\boldsymbol{\tau} + \mathbf{Q} + \mathbf{A}^\top \boldsymbol{\lambda} \quad (3.36)$$

where \mathbf{M} is the mass matrix, \mathbf{C} is the Centrifugal and Coriolis matrix, and \mathbf{G} is the gravitational matrix, defined as follows:

$$\text{The mass matrix: } M_{i,j} = \frac{\partial^2 \mathbf{T}}{\partial \dot{q}_i \dot{q}_j} \quad (3.37)$$

$$\text{The Centrifugal and Coriolis Matrix: } \mathbf{C} = \dot{\mathbf{M}}\dot{\mathbf{q}} - \frac{\partial \mathbf{T}}{\partial \mathbf{q}} \quad (3.38)$$

$$\text{The gravitational matrix: } \mathbf{G} = \frac{\partial \mathbf{V}}{\partial \mathbf{q}} \quad (3.39)$$

The dynamics of the system can thus be derived as:

$$\ddot{\mathbf{q}} = \mathbf{M}^{-1}(\mathbf{B}\boldsymbol{\tau} + \mathbf{Q} + \mathbf{A}^\top \boldsymbol{\lambda} - \mathbf{C}\dot{\mathbf{q}} - \mathbf{G}) \quad (3.40)$$

In summary, this method can be used to describe the dynamics of a system in terms of the generalized coordinates and the non-conservative forces and torques acting on the system. As an example of the application of this method, the dynamics of a simple skateboard model have been derived using the Euler-Lagrange method in appendix A.1.

3.3 Integrating the Dynamics

The techniques used to solve trajectory optimization problems are often classified by the transcription method used to convert the trajectory optimization problem into the general constrained optimization form [12]. Most techniques can be described as either direct methods, or indirect methods [41][42], with some techniques combining aspects of the two methods. According to Kelly, indirect methods are numerically unstable and difficult to initialize [12]. Therefore, this study will focus on direct methods. Importantly, a key feature of direct methods is the chosen integration scheme, which, in the case of mechanics, determines the method for integrating the system dynamics.

3.3.1 Shooting and Direct Methods

Shooting methods are similar to direct methods in the property that both methods transcribe the optimization problem into nonlinear program (NLP), however the difference between the methods is that shooting methods use simulation to approximate the trajectory [34]. Within shooting methods, there exists single shooting methods and multiple shooting methods. Single shooting methods approximate the entire trajectory using simulation, whereas multiple shooting methods divide the trajectory into segments and approximate each segment using simulation. Multiple shooting is more robust and better suited for complex problems [34].

Direct methods, as described by Kelly [34], are methods that attempt to discretize a continuous trajectory optimization problem through the use of polynomial splines to approximate the continuous functions in the problem statement. Discretizing a continuous trajectory involves dividing the trajectory into N nodes. Naturally, when a continuous trajectory is discretized, there will be an error in the discretization. The error between the polynomial spline approximations and the continuous trajectory is known as the defect.

Most direct methods transcribe a continuous-time trajectory optimization problem into a NLP which can then be solved - much like shooting methods. A direct transcription method is shown in Figure 3.6, where a piecewise-linear polynomial is used to discretize the state trajectory between the nodes, and a piecewise-constant function is used to represent the control trajectory.

Direct methods can further be classified as h-methods or p-methods as described by Kelly [12]. Methods classified as h-methods use lower order polynomials and a higher number of trajectory segments for interpolation. Transcription methods which generally use h-methods are direct transcription and direct collocation. Methods classified as p-methods on the other hand use high order polynomials and less trajectory segments for interpolation. An example of a p-method is orthogonal collocation. Each method is better than the other for certain problems. Problems with smooth analytical solutions are best described with h-methods, and problems with any discontinuities in the solution are best suited to be solved with p-methods.

3.3.2 Numerical Approaches for ODEs

As motioned previously, the integration scheme chosen for the optimization problem is a key feature of any direct method. The integration scheme converts a continuous ordinary differential equation (ODE) into a discrete numerical approximation.

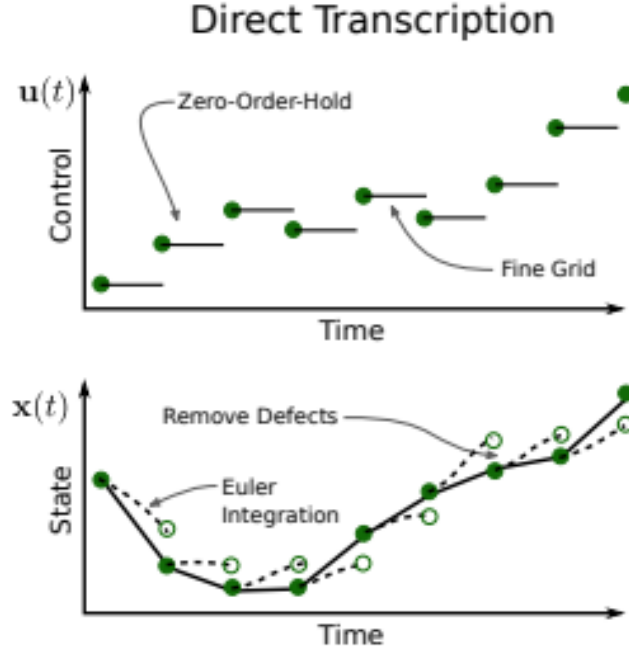


Figure 3.6: Direct transcription methods represent the control as a piecewise-constant trajectory and the state as a piecewise-linear trajectory [12].

Numerical approaches for ODEs range from simple first order implicit integration methods, such as the Euler method, to higher order implicit methods such as Runge-Kutta and Gauss-Radau methods. Another method common in classical mechanics is the semi-implicit Euler method. Given a system with differential equations of the form:

$$\frac{dx}{dt} = f(t, v) \quad (3.41)$$

$$\frac{dv}{dt} = g(t, x) \quad (3.42)$$

The semi-implicit Euler method is expressed as:

$$v_{n+1} = v_n + g(t_n, x_n)\Delta t \quad (3.43)$$

$$x_{n+1} = x_n + f(t_n, v_{n+1})\Delta t \quad (3.44)$$

where Δt is the time step and $t_n = t_0 + n\Delta t$ is the time after n nodes. This numerical approach can be used to simplify the implementation the implementation of the contact-implicit method, as demonstrated by Shield [7]. Further details of this will be given under the contacts section.

3.4 Modeling Collisions

3.4.1 Elastic and Inelastic Collisions

Collisions between objects are defined according to the relationship between the total kinetic energy of the objects before and after a collision. Perfectly elastic collisions are collisions between multiple bodies in which there is no loss of kinetic energy and momentum as a result of the collision. Inelastic collisions are those which have a complete loss of total kinetic energy as a result of the collisions (perfectly inelastic) or which some kinetic energy is lost as a result of the collision. If we denote the time step before the collision as n and the time step after the collision as $n+1$, an inelastic and elastic collision between bodies A and B can be expressed in terms of the kinetic energy and velocities of the bodies involved in the collision, as well as the coefficient of restitution:

$$T_n = e^2 T_{n+1} \quad (3.45)$$

$$e = \frac{v_{B,n+1} - v_{A,n+1}}{v_{A,n} - v_{B,n}} \quad (3.46)$$

where T_n and T_{n+1} are the total kinetic energies before and after the collision respectively, $v_{A,n}$ and $v_{B,n}$ are the velocities of object A and B before the collision, and $v_{A,n+1}$ and $v_{B,n+1}$ are the velocities of object A and B after the collision. The coefficient of restitution, e , is a property of the objects involved in the collision which relates the initial and final velocities and kinetic energies of the objects before and after the collision, classifying the collision on the scale between perfectly elastic, $e = 1$, and perfectly inelastic, $e = 0$. For collision between an object and the ground, it can be shown that the following relationship is true:

$$v_{A,n+1} = ev_{A,n} \quad (3.47)$$

3.4.2 Hybrid-Dynamic Systems

Hybrid-Dynamic systems, put simply, are systems which have continuous dynamics up until certain events, at which there is a discontinuous switching in the states of the system [13]. A basic example of this is a bouncing ball. When the ball strikes the ground, an impulsive force acts on the ball which causes the velocity of the ball to discontinuously change from negative (towards the ground) to positive (away from the ground). These systems can be described with discrete continuous dynamics called “modes”, activated in a prescribed order called the “mode sequence”, separated by specific events or condi-

tions called “guard conditions” [13][43]. The concepts of modes, guard conditions and discontinuous state mappings are shown in Figure 3.7.

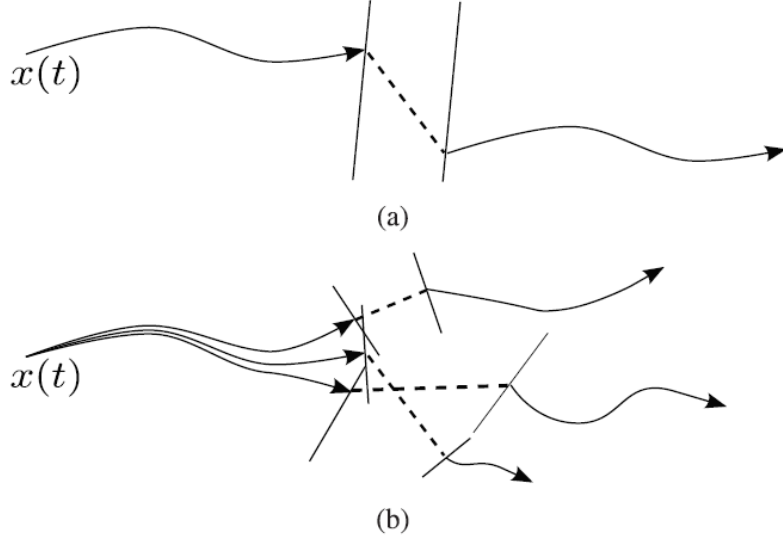


Figure 3.7: A visual description of hybrid-dynamic system state trajectories - the initial state trajectories are continuous until the guard condition is met, then a discontinuous change in state occurs. A simple example of a single discontinuous state mapping is shown in (a) and a complex example with multiple discontinuous state mappings is shown in (b) [13].

Often, as in the bouncing ball case, these discontinuities in the state trajectory of the system are created by collisions with the external environment. These collisions can be described as either elastic or inelastic collisions, as explained previously. There are two common methods for handling discontinuous state changes and collisions: the hybrid modeling method and the contact-implicit method. The hybrid modeling method can be used to model elastic and inelastic collisions, whereas the contact-implicit method is limited to modeling inelastic collisions. Each will be explained briefly.

3.4.3 Hybrid Dynamics Method

One of such methods that handles the discontinuous dynamics created through collisions with the external environment is the hybrid modeling method. In order to generate the mode schedule, knowledge of the contact order must be known and added as a constraint to the optimization problem, and discontinuous mapping between states before and after the guard condition is met must be specified. [13]. This concept of modes, guard conditions and discontinuous dynamics are shown in Figure 3.7.

Applying this method to a bouncing ball, it is trivial that when the ball is in contact with the ground, the ground can exert a force on the ball, but when the ball is in the air, the ground cannot. This produces two hybrid models for the system: when the ball is in

the air, \ddot{y}_{air} , and when the ball is in contact with the ground, $\ddot{y}(G_y)_{gnd}$, where G_y is the ground reaction force on the ball.

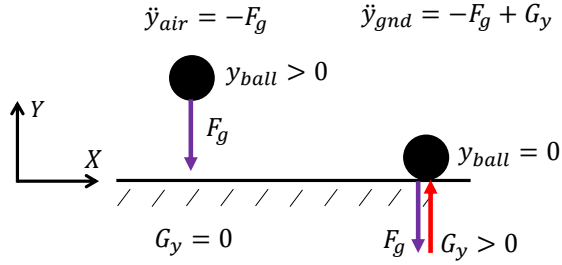


Figure 3.8: An illustration of the hybrid models of the ball - when it is in contact with the ground, \ddot{y}_{gnd} , and when it is above the ground, \ddot{y}_{air} .

Continuing this example, in order to formulate the bouncing ball as a trajectory optimization problem, the time or node at which the ball makes contact with the ground must be specified. For a trajectory optimization problem with nodes $n = 1, \dots, N_1, \dots, N$, given that the ball-ground contact is perfectly inelastic, and the contact is prescribed to occur at $n = N_1$, the hybrid model would be as follows:

$$\ddot{y} = \ddot{y}_{air} \quad \text{for } n < N_1 \quad (3.48)$$

$$\ddot{y} = \ddot{y}_{gnd} \quad \text{for } N_1 \leq n \leq N \quad (3.49)$$

This method has been successfully implemented for many complex biomechanical problems, including those involving walking gaits of humanoid robots where the contact order is already intuitively known [44][43]. It was also successfully implemented in a previous study of the ollie manoeuvre [14] as shown in Figure 3.9, where the dynamics of the skateboard undergoing an ollie manoeuvre are discretized and handled as discontinuous functions.

The limitation of this method is that the contact order or mode schedule of the trajectory must be specified, even if the contact order is not known. Problems such as a hand gripping a ball [13] where the contact order are not fully known cannot be solved using this method. This may be a problem for this study of the ollie since, upon landing, the contact order of the wheels can alternate between front wheel or back wheel landing first, or both wheels landing at the same time. However, this method may be applicable to modeling the collision between the skateboard tail and the ground.

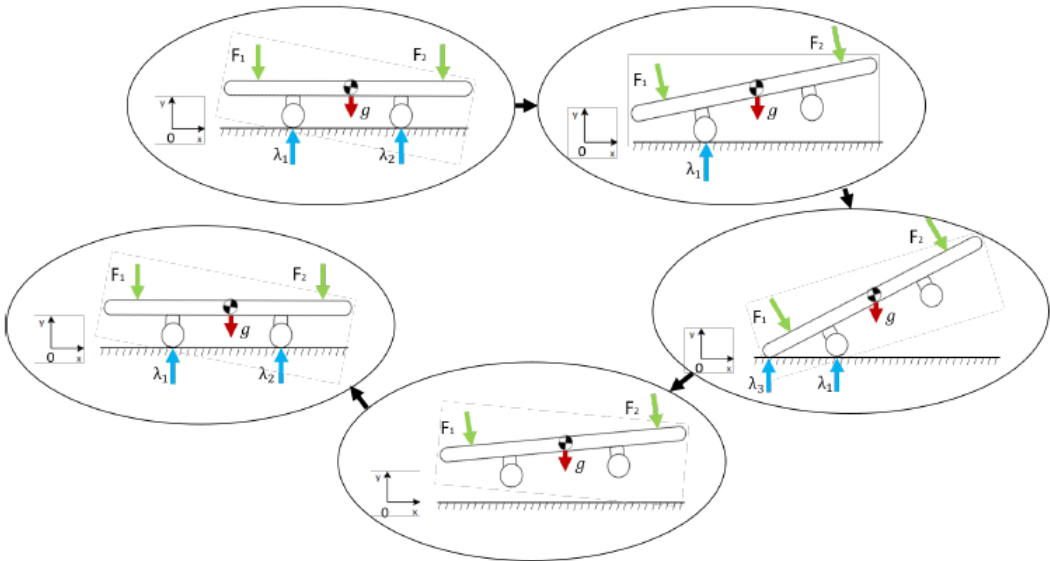


Figure 3.9: The ollie manoeuvre was posed as discrete hybrid dynamic models in the study by Kolev [14].

3.4.4 Contact-Implicit Method

Another method for modeling contacts in rigid-body systems was proposed by Posa et al. [13] to overcome the problem of having to specify the mode schedule of the system. The limitation to this method is that it is only applicable to inelastic collisions. Using this method, the issue of having to specify the mode sequence is removed, which is highly desirable for problems where the contact order is not intuitively defined. This method has been successfully implemented for previous biomechanical studies involving unscheduled contacts such as fingers gripping a ball [13] and the human motions of crawling, climbing and acrobatics [15].

This method defines complementary relationships between the state or control trajectories to model inelastic collisions and Coulomb friction to formulate a problem with continuous system dynamics. To understand the constraint equations used to produce continuous dynamics, complementary relationships should be defined. Given two events A and B that cannot occur simultaneously, the complementary relationship between the events is defined as follows:

$$AB = 0 \quad (3.50)$$

This means that if event A is active ($A > 0$), event B must not be active ($B = 0$). For example, referring back to the bouncing ball, if event A is the ground reaction force and event B is the y-position of the ball, complementing the two events would ensure that

the ground cannot exert a force on the ball if it is not on the ground.

$$y_{ball}G_y = 0 \quad (3.51)$$

Now that the complementarity relationship has been described, the set of constraint equations provided by Posa et al. are as follows:

$$\phi(q_k) \geq 0 \quad (3.52)$$

$$\lambda_{k,z}, \lambda_{k,x}^+, \lambda_{k,x}^-, \gamma_k \geq 0 \quad (3.53)$$

$$\mu\lambda_{k,z} - \lambda_{k,x}^+ - \lambda_{k,x}^- \geq 0 \quad (3.54)$$

$$\gamma_k + \psi(q_k, \dot{q}_k) \geq 0 \quad (3.55)$$

$$\gamma_k - \psi(q_k, \dot{q}_k) \geq 0 \quad (3.56)$$

$$\phi(q_k)^\top \lambda_{k,z} = 0 \quad (3.57)$$

$$(\mu\lambda_{k,z} - \lambda_{k,x}^+ - \lambda_{k,x}^-)^\top \gamma_k = 0 \quad (3.58)$$

$$(\gamma_k + \psi(q_k, \dot{q}_k))^\top \lambda_{k,x}^+ = 0 \quad (3.59)$$

$$(\gamma_k - \psi(q_k, \dot{q}_k))^\top \lambda_{k,x}^- = 0 \quad (3.60)$$

where $\phi(q_k)$ is the perpendicular distance between the body and the ground; $\lambda_{k,z}$ is the vertical ground reaction force, and $\lambda_{k,x}^+$ and $\lambda_{k,x}^-$ are the ground friction force resolved into positive and negative components; γ_k is a slack variable; μ is the coefficient of static friction; and $\psi(q_k, \dot{q}_k)$ is the tangential velocity of the body relative to the ground. These equations will be discussed further in the Model Design and Development chapter. In summary, these constraints define the characteristics of the friction and reaction force that is induced when a body makes contact with the ground, or with another body.

It is noticeable that this set of constraints are of the form:

$$G(x) \geq 0 \quad (3.61)$$

$$H(x) \geq 0 \quad (3.62)$$

$$G(x)^\top H(x) = 0 \quad (3.63)$$

According to (Luo et al., 1996), this set of constraints creates a NLP which is difficult to solve due to the ill-posed nature of the constraints. Thus, to increase the solvability of the problem, Mordatch et al. [15] introduces the contact forces as optimization parameters with the feasibility of the contact used as a penalty term in the cost function rather than

as a constraint.

$$\alpha, \beta \geq 0 \quad (3.64)$$

$$G(x) = \alpha \quad (3.65)$$

$$H(x) = \beta \quad (3.66)$$

where α and β are introduced as penalty variables to improve the solving feasibility of the optimization problem [45]. These variables are included in the objective function to ensure they are minimized to below an acceptable upper bound.

If a hybrid-dynamic system interacts with another body or the ground, it is likely that a frictional force will be induced between the two-bodies or the body and the ground, unless it is acceptable to assume the contact is frictionless. The characteristics of this friction force are defined by the friction cone given in equation 3.54.

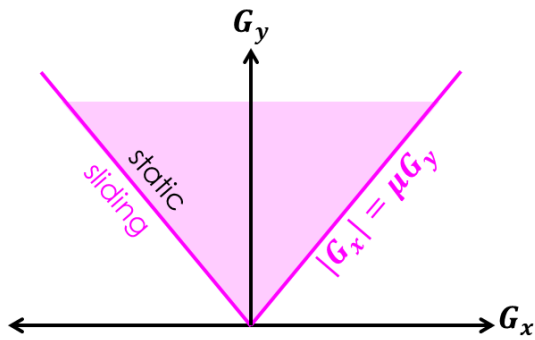


Figure 3.10: A visual depiction of the friction cone created in the implementation of the contact-implicit method [7].

3.5 Solving Trajectory Optimization Problems

3.5.1 Initialization

As stated previously, a trajectory optimization problem aims to minimize a given objective function to converge to an optimal solution. However, due the complex multi-dimensional nature of the problems, the objective function is a n-dimensional surface with local and global minima. Therefore, optimality can either be local or global. This concept is shown with a simple two-dimensional example in Figure 3.11. This is where the importance of initialization is realized. A problem which is posed with poor initialization has the potential to be infeasible, or produce a solution which is locally optimal, but far from the globally optimal solution [12].

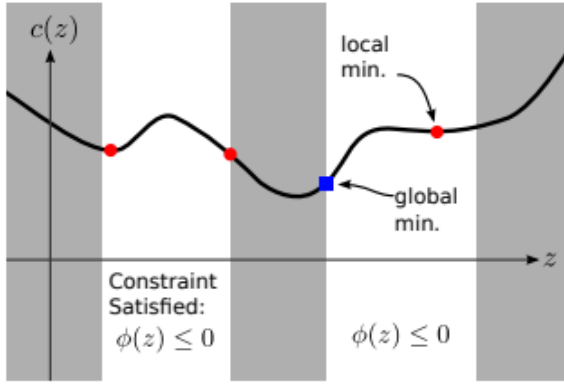


Figure 3.11: An illustration of local and global minima in an optimization problem, with the shaded area representing conditions where the constraints are not satisfied [12].

3.6 The Use of Trajectory Optimization in Motion Studies

In recent times, trajectory optimization has gained traction as a method to generate, simulate and analyse specific motions - be that in robotics, classical mechanics studies, or more specifically, in biomechanics studies. A study by Mordatch et al. [15] used trajectory optimization to develop a synthesis framework to generate a set of complex human motions. The generated motions are shown in Figure 3.12. The synthesis framework developed in this study has applications in biomechanics and robotics. Focusing on biomechanics, a study by Wilson et al. [23] explored the effects that arms have on performing a running jump using trajectory optimization.

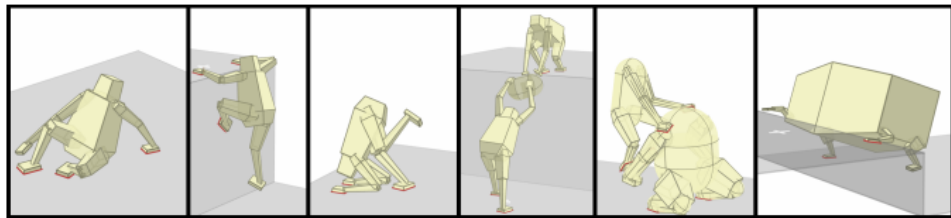


Figure 3.12: Results from the study by Mordatch et al. which used trajectory optimization to generate human manoeuvres [15].

These studies both aim to replicate and generate human motion for the purpose of studying the aspects of the motion. This principle of using trajectory optimization for motion studies is at the core of this project, and thus, these studies will be drawn upon in formulating the trajectory optimization problem and design of the system.

Chapter 4

Methodology

This chapter describes the process of development for the system, as well as the aspects of the trajectory optimization problem which are constant across all of the tests. Furthermore, the conventions and notation used for the remainder of the report are described.

4.1 Conventions and Notation

Due to the multiple bodies involved in the systems that will be developed in this study, it is important that the notation used for the remainder of the report is established for ease of reading. The notation follows the conventions shown in Figure 4.1.



Figure 4.1: The notation adopted for this study to describe the variables in the systems.

where “body” refers to a body in the system, “reference frame” describes the reference frame of the variable, “direction” gives the direction of the force, when applicable, and “index” indicates the discrete index of a variable. For example, if, at the 3rd node a force is acting on the back of the skateboard in the y-direction in the skateboard reference frame, the variable would be given as: ${}^bF_{y,3}^s$.

4.2 Development of the Trajectory Optimization Problem

An iterative approach was used to develop the skateboard-skateboarder system. The system was partitioned into individual features such as the various contacts and the skateboard and skateboarder subsystems. These features were implemented in isolation using simple modeling. Once each feature had been successfully implemented, they were integrated, initially with a simple model. The integrated design was then iteratively developed until a final system design was decided upon.

4.3 Formulating the Trajectory Optimization Problem

This section details the general decisions made in formulating the trajectory optimization problem in terms of the modeling of the skateboard-skateboarder system, the integration scheme, the objective function, the initialization technique and the software implementation.

4.3.1 Modeling Approach

The coordinates used to describe the skateboard and skateboarder models were chosen using the generalized coordinates method. This allowed the equations of motion of the models to be derived using the Euler-Lagrange method, specifically in the manipulator equation form (equation 3.36). Furthermore, the generalized coordinates method was chosen to simplify the constraints on the state of the system, such as the angle between leg and pelvis.

The skateboarder model will developed as a planar kinematic chain, with each link connected with an ideal revolute joint. The actuators of the skateboarder model were modelled as ideal actuators with no limit on the power or work of the actuator, but a limit on the upper and lower bound of the force and torque that can be applied. Furthermore, the skateboarder model will be under-actuated. The skateboarder model was designed to replicate the most basic characteristics of the skateboarder, and thus, this simplification was deemed reasonable for the sake of this study.

4.3.2 Transcription Method and Integration Scheme

The transcription method chosen for this study was the direct collocation method. The optimization problem was formulated with N trajectory segments or elements, such that each finite element in the trajectory, n , could be expressed as:

$$n = 1, \dots, N \quad (4.1)$$

In conjunction with the direct collocation method, the integration scheme chosen was implicit semi-Euler. This integration scheme was chosen to reduce the complexity of the trajectory optimization problem by using a first order polynomial spline, while ensuring

the dynamics of the rigid-bodies involved are adequately captured. It was shown in the study by Kolev [14] that this integration scheme was sufficient to replicate a basic ollie manoeuvre. Furthermore, using the semi-Euler scheme reduces the number of redundant generalized coordinates and actuators in the control and state trajectories.

The integration schemes for the position and velocity of the generalized coordinates are therefore defined as:

$$q_n = q_{n-1} + h_m h_n \dot{q}_n \quad (4.2)$$

$$\dot{q}_n = \dot{q}_{n-1} + h_m h_n \ddot{q}_{n-1} \quad (4.3)$$

where h_m is the master time step and h_n is a decision variable defining the lower and upper bounds of the master time step. For the sake of ease of reading, the time step was defined using the following definition:

$${}^m h_n = h_m h_n \quad (4.4)$$

The master time step, h_m , and the bounds on the decision variable h_n were chosen as follows:

$$h_m = 0.01s \quad (4.5)$$

$$0.8 \leq h_n \leq 1.2 \quad (4.6)$$

Choosing these bounds on h_n allows the effective time step of the system to be in the range $0.008s \leq {}^m h_n \leq 0.012s$ while ensuring the scaling of the decision variable h_n is within the desirable range. Furthermore, a master time step of $0.01s$ is considered short enough to capture the dynamics of a biomechanical system.

4.3.3 The Objective Function

The objective function was chosen to minimize the forces, ${}^i F$, and torques, ${}^i \tau$, applied to the system using discrete integration. Additionally, in the case when complementary relationships were implemented (the contact-implicit method), a penalty term, ${}^i p$, was included to ensure the magnitude of the complementary constraints were minimized to below a threshold of feasibility of 10^{-6} . For a system with m_1 applied forces, m_2 applied torques, and m_3 penalties, the general form of the objective function was formulated as

follows:

$$\text{Minimum force squared: } J_1 = \sum_{n=1}^N ({}^i F_n^2 + \dots + {}^{m_1} F_n^2) h_m h_n \quad (4.7)$$

$$\text{Minimum torque squared: } J_2 = \sum_{n=1}^N ({}^i \tau_n^2 + \dots + {}^{m_2} \tau_n^2) h_m h_n \quad (4.8)$$

$$\text{Minimum complimentarity penalty: } J_3 = \sum_{n=1}^N {}^i p_n + \dots + {}^{m_3} p_n \quad (4.9)$$

$$\text{The objective function: } J = \sum_{n=1}^N \alpha_1 J_1 + \alpha_2 J_2 + \alpha_3 J_3 \quad (4.10)$$

where α_1 , α_2 and α_3 are scalar values used to weight the individual costs. For each test, the values of α_1 , α_2 and α_3 were adjusted to enable the solver to converge on a locally optimal and feasible solution.

4.3.4 Initialization

The method for initializing the trajectory optimisation problem had two stages:

- A. **Developing the trajectory:** The trajectory for the ollie manoeuvre was initialized iteratively by solving the phases of the manoeuvre (e.g. the pre-“pop” phase) to the desired penalty with the cost of the forces and torques removed. Then, the solution was used as the seed for the next phase of the manoeuvre. This was repeated until the entire manoeuvre was completed.
- B. **Optimal control of the trajectory:** Once the entire trajectory been solved using step 1, the cost associated with forces and torques was added back to the objective function, and the solved trajectory was used as the seed for the optimization problem.

4.3.5 Software Implementation

The trajectory optimization problem was implemented in Python using Pyomo - collection of open-source Python software packages for formulating optimization models - with IPOPT’s MA86 linear solver [46]. The tolerance of the solver was set to 10^{-5} . The Python program was run on a 64-bit i-5 Lenova laptop with 8GB of RAM.

4.4 Validation of Results

In order to conclude to what extent the simulation was able to replicate the chosen ollie manoeuvres, a method for validation of the simulated results must be decided upon.

It would be desirable to compare the trajectory of the skateboard-skateboarder simulation to the trajectory of a real-life skateboarder performing an ollie. However, a technical analysis of the trajectory of the skateboard performing an ollie could only be found for the RO manoeuvre (see Figure 4.2). Thus, the RO manoeuvre trajectory will be compared to Figure 4.2 to assess the similarities of the two trajectories.

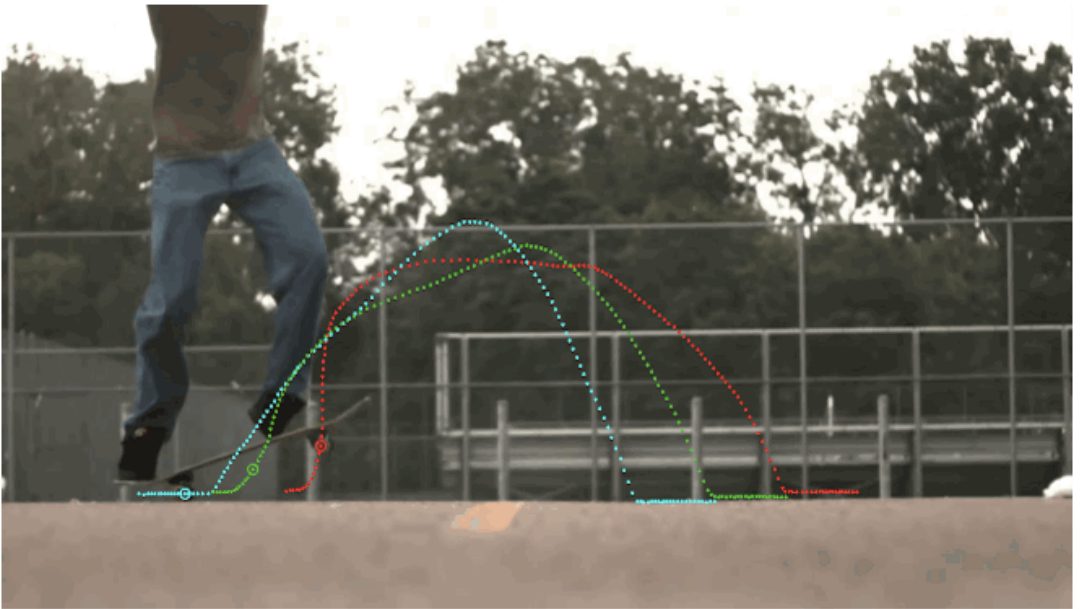


Figure 4.2: The trajectory of the front (red) and back (blue) wheels, and the centre of mass (green) of the skateboard performing an ollie. Adapted from Bhatia [16].

The SO manoeuvre has been captured in videos online, therefore, segmenting the video into snapshots at given times will provide a visual display of the trajectory of a skateboarder performing a SO. Snapshots of the chosen video are shown in Figure 4.3, which will be used to perform a high-level comparison of the simulated SO to the real-life SO to assess the extent at which the trajectories are similar.



Figure 4.3: Snapshots of a skateboarder performing a SO manoeuvre [17].

The ground reaction forces (GRF) for the SO, RO, OU and OD manoeuvres have been quantified in literature, in terms of the force profiles shown in Figures 2.4 and 2.5, and the

peak reaction forces, summarised in Table 2.1. These measured results will be compared to the simulated GRFs acting on the skateboard wheels. Using this comparison, it can be seen whether the simulated results fall within the standard deviation of the recorded results, and thus, whether the simulation has accurately replicated the GRFs involved in the ollie.

Chapter 5

Model Design and Development

This chapter details the development and implementation of isolated aspects of the ollie manoeuvre individually, then the iterative design stages used to develop the skateboard-skateboarder system to perform the ollie are described. The skateboard-skateboarder system as a whole is complex, involving various contacts and models. Therefore, the system should be broken down into definable, isolated aspects which can be developed individually, and integrated once successfully tested. The isolated aspects of the skateboard-skateboarder system that are to be developed are shown in Figure 5.1 in the chosen order of development.

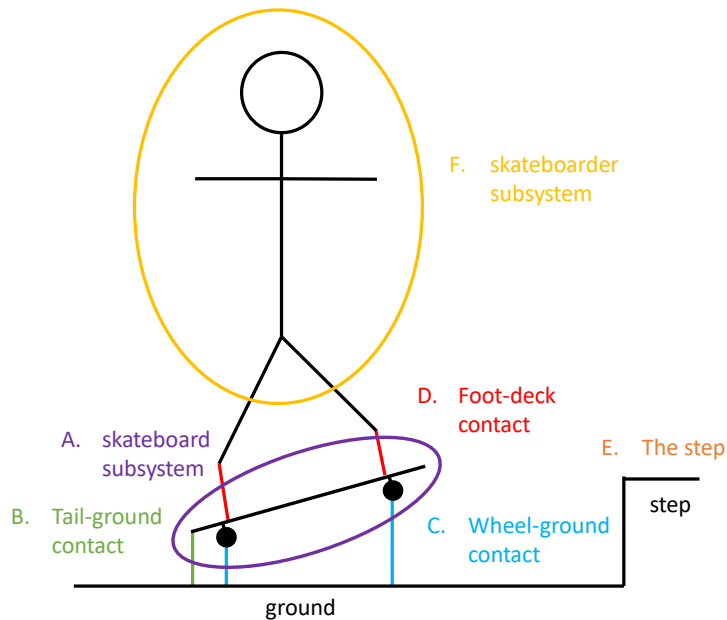


Figure 5.1: A basic description of the skateboard-skateboarder system and the identified problems under investigation.

In order to explore many of these isolated aspects, it was useful to draw on a simplistic example to implement the relevant theory. The example chosen was the simple bouncing ball.

5.1 The Bouncing Ball Model

The simple example of the bouncing ball was used to demonstrate inelastic and elastic collisions - the basis of the modeling of the contact with the wheels and the ground

(the landing), the skateboarder's feet and the skateboard, and the collision between the skateboard tail and the ground (the “pop”). The ball was modeled as a point mass of mass $2kg$, defined with one generalized coordinate, the position of the ball in the inertial y -frame, ${}^B y$.

Two different ball models were created to test the methods for handling the inelastic and elastic collisions. The models are largely the same, however, the model used for the inelastic collision, shown in Figure 5.2B, includes a GRF, G_y , and the model for the elastic collision, shown in Figure 5.2A, does not.

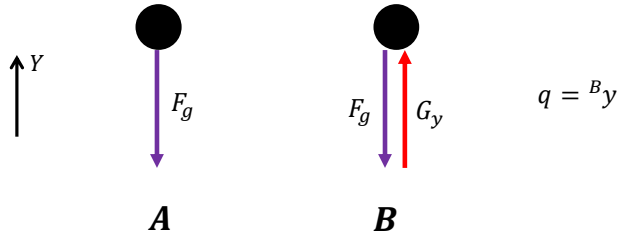


Figure 5.2: The two ball models used to demonstrate the elastic tail and ground collision (A) and the inelastic wheel on ground collision (B).

5.2 Modeling the Skateboard

The skateboard model needed to encompass the key components and dynamics of a skateboard using valid assumptions that ensure that the physical integrity of the model is still intact. The chosen key physical components were the deck, the wheels and the trucks. The deck was modelled as a rigid-beam of length l_d and mass m_d . The wheels and trucks were considered to be of negligible mass with a wheel base of l_w and a board clearance of h_d measured from the ground to the deck of the board. An illustration of these dimensions is shown in Figure 5.3A. Based on the physical properties of the skateboard, these values were chosen as follows:

$$l_d = 80\text{cm} \quad (5.1)$$

$$l_w = 45\text{cm} \quad (5.2)$$

$$h_d = 9\text{cm} \quad (5.3)$$

$$m_d = 2\text{kg} \quad (5.4)$$

5.2.1 Summary of Assumptions for the Skateboard Model

To reduce the complex system of the skateboard to a simplistic functional model, valid modeling assumptions needed to be made. The assumptions made and the justifications of the assumptions are detailed below.

Friction between the wheels and the ground

The friction force between the skateboard wheels and the ground were considered frictionless for the purpose of this study. This assumption was made as this friction force is considerably lower in magnitude to the other forces involved in the system and the wheels were considered to operate in a region where they rolled and did not slide. Therefore, the friction force was considered negligible.

Friction between the foot and the skateboard deck

As described previously, the skateboarder's underside of the shoe was considered to be made of rubber, and the deck of the skateboard was considered to be made of a fine sand-paper like material. Therefore, the coefficient of static friction was chosen to be 0.78 based on the study by Bani et al. [47] that calculated the coefficient of static friction between different sized rubber granules from used tires and different surfaces.

The coefficient of restitution between the ground and the skateboard tail

The tail of the skateboard was assumed to be made of wood and the ground was assumed to be concrete. Based on a study by Bennett and Meepegala [48], the coefficient of restitution between these two materials was found to be 0.6.

The pop-angle and skateboard flex

The curve of the tail and front of the skateboard deck, also known as the pop-angle, was excluded to simplify the collision between the ground and the tail of the board. Furthermore, any flex or spring in the board was discarded when the board was considered as a rigid-body. This assumption was made as the skateboard did not appear to flex in the slow motion videos analysed of the manoeuvre.

5.2.2 Generalized Coordinates

The generalized coordinates chosen to represent the skateboard model are as follows:

$${}^s\mathbf{q} = [{}^s x, {}^s y, {}^s \theta]^\top \quad (5.5)$$

where $({}^s x, {}^s y)$ is the position of the centre of mass of the skateboard model and ${}^s \theta$ is the angle of the skateboard deck defined counter-clockwise relative to the inertial frame. The choice of these generalized coordinates is shown in Figure 5.3B.

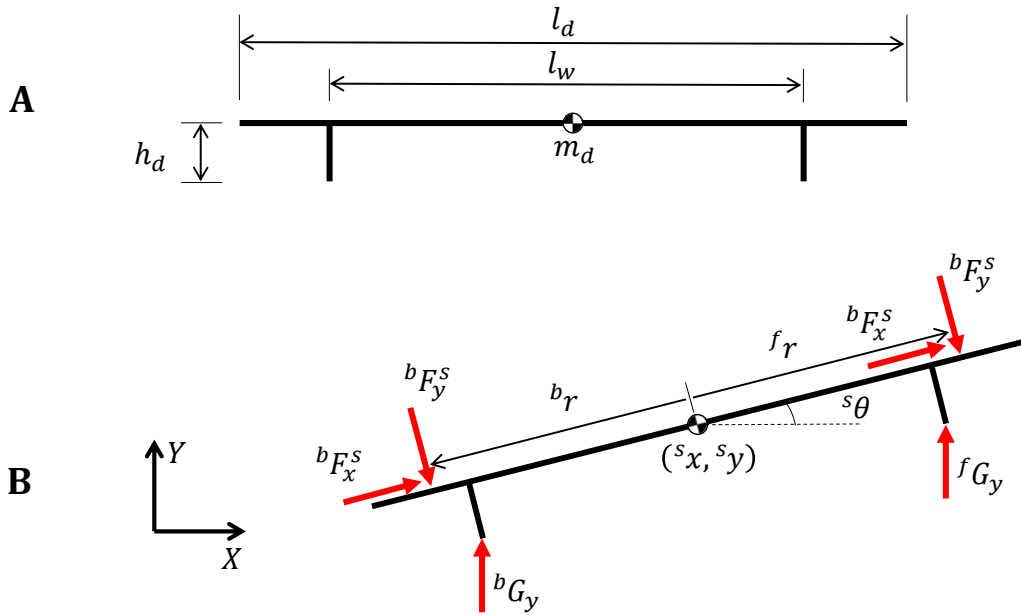


Figure 5.3: The skateboard model used in all stages of development, described in terms of its physical properties (A), and the chosen generalized coordinates and forces (B).

It is useful to define auxiliary variables for the skateboard model. The auxiliary variables of interest are the positions of the tail, $({}^t x, {}^t y)$, and nose, $({}^n x, {}^n y)$, of the skateboard, and the positions of the back wheels, $({}^{bw} x, {}^{bw} y)$, and front wheels, $({}^{fw} x, {}^{fw} y)$, of the skateboard. These are shown in Figure 5.4.

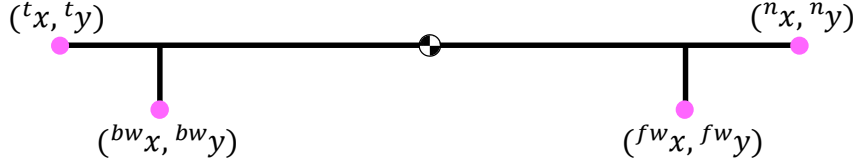


Figure 5.4: An illustration of the auxiliary variables chosen for the skateboard model.

These auxiliary variables are defined using the generalized coordinates as follows:

$$\begin{bmatrix} {}^t x \\ {}^t y \end{bmatrix} = \begin{bmatrix} {}^s x - 0.5l_d \cos({}^s \theta) \\ {}^s y - 0.5l_d \sin({}^s \theta) \end{bmatrix} \quad (5.6)$$

$$\begin{bmatrix} {}^n x \\ {}^n y \end{bmatrix} = \begin{bmatrix} {}^s x + 0.5l_d \cos({}^s \theta) \\ {}^s y + 0.5l_d \sin({}^s \theta) \end{bmatrix} \quad (5.7)$$

$$\begin{bmatrix} {}^{bw} x \\ {}^{bw} y \end{bmatrix} = \begin{bmatrix} {}^s x - 0.5l_w \cos({}^s \theta) + h_d \sin({}^s \theta) \\ {}^s y - 0.5l_w \sin({}^s \theta) + h_d \cos({}^s \theta) \end{bmatrix} \quad (5.8)$$

$$\begin{bmatrix} {}^{fw} x \\ {}^{fw} y \end{bmatrix} = \begin{bmatrix} {}^s x + 0.5l_w \cos({}^s \theta) - h_d \sin({}^s \theta) \\ {}^s y + 0.5l_w \sin({}^s \theta) - h_d \cos({}^s \theta) \end{bmatrix} \quad (5.9)$$

Using these auxiliary variables, constraints will be able to placed on the position of the auxiliary variables. For example, y-position of the wheels of the skateboard should always be greater than zero.

5.2.3 Applied Forces and Ground Reaction Forces

A skateboarder is able to use their legs and feet to apply forces on the deck of the skateboard. These forces were included in the skateboard model for both the front and back feet as forces acting normal to the deck of the board, ${}^b F_y^s$, and parallel to the deck of the board, ${}^b F_x^s$, at a parallel distance of ${}^b r$ from the centre of the deck of the skateboard.

The vertical GRFs considered for the skateboard model were modelled as forces normal to the ground on the front wheels, ${}^f G_y$, and the back wheels, ${}^b G_y$ of the skateboard.

5.3 The Skateboard Tail and Ground Contact

The collision between the tail of the skateboard and the ground (the “pop”), is elastic by nature since the skateboard appears to ”bounce” off the ground. The tail-ground contact

was developed in two stages: 1) an elastic collision between the simple ball model and the ground was developed, 2) this behaviour was transferred to the skateboard model.

Using the principles of elastic collisions expressed in equation (3.47), the velocity of the ball before and after making contact with the ground can be expressed with the following relationship:

$$\dot{q}_{n+1} = e\dot{q}_n \quad (5.10)$$

Applying the hybrid dynamics method to the bouncing ball trajectory optimization problem using the model shown in Figure 5.2A, equation (5.10) could be implemented as a discontinuous switch in the velocity state. Choosing the guard condition as the ball making contact with the ground at $n = n_1$, the elastic collision could be described as follows:

$$q_{n_1} = 0 \quad (5.11)$$

$$\dot{q}_{n_1+1} = e\dot{q}_{n_1} \quad (5.12)$$

The results of the elastic bouncing ball test are shown in Figure 5.5. It is evident that as the coefficient of restitution is decreased from 1, the observed response moves from perfectly elastic to inelastic.

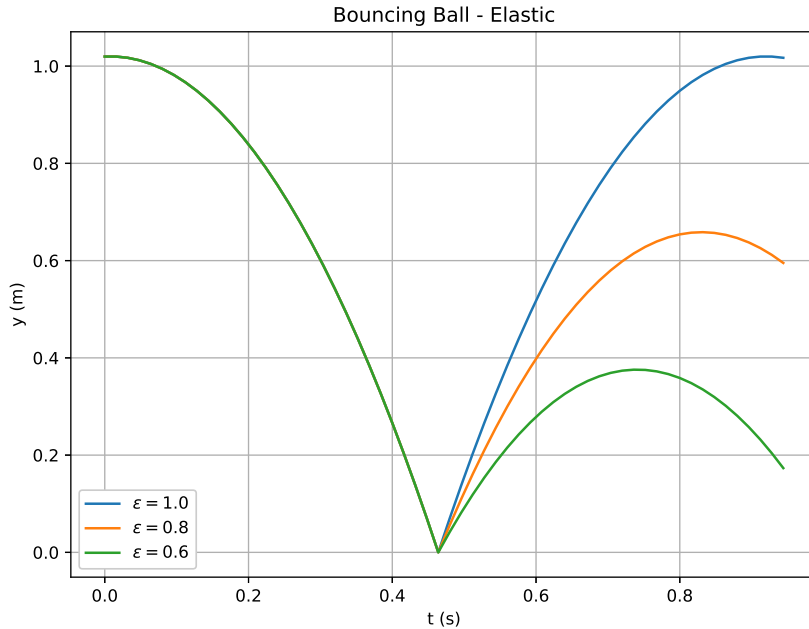


Figure 5.5: Plot of the y-position of the bouncing ball against time showing that as the coefficient of restitution is decreased, the ball loses more energy at impact and subsequently bounces to a lower height.

During the ollie “pop” phase, the skateboard’s tail effectively bounces off the ground, therefore, these results appear to prove that this method is indeed suitable for modeling tail-ground contact. It should be noted that a limitation of this method is that the guard condition, $y_{n_1} = 0$, must be specified, and thus, the moment when the ball strikes the ground must be specified.

In order to transfer this implementation to the skateboard model, the kinetic energy of the skateboard before the collision must be defined. The conventions used for the skateboard model are shown in Figure 5.6.

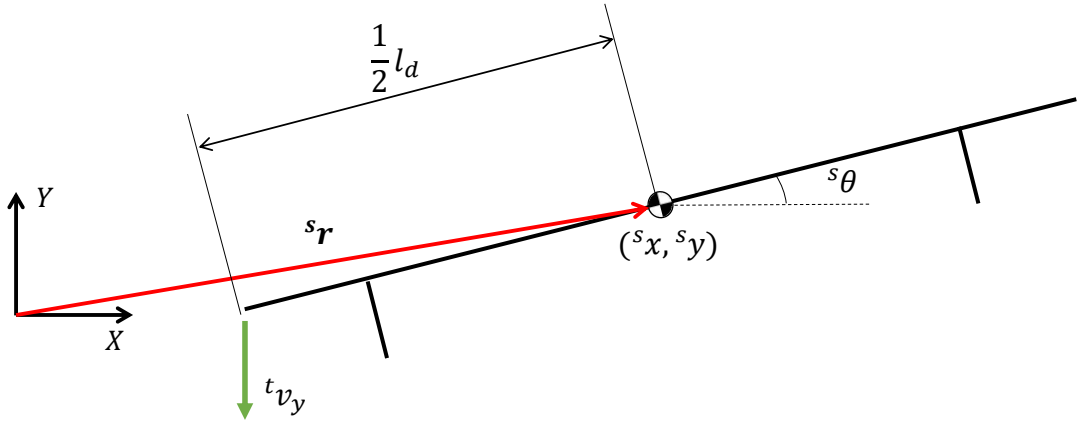


Figure 5.6: The conventions used for the skateboard model to model the elastic collision between the skateboard tail and the ground, or the ”pop”.

The translational energy, sT_t , and kinetic energy, sT_r , of the skateboard before the collision are defined as follows:

$${}^sT_t = \frac{1}{2}m_s {}^s\dot{\mathbf{r}}^T {}^s\dot{\mathbf{r}} \quad (5.13)$$

$${}^sT_r = \frac{1}{2}I_s {}^s\dot{\theta}^2 \quad (5.14)$$

where m_s is the mass of the skateboard, I_s is the moment of the inertia of the skateboard, ${}^s\dot{\mathbf{r}}$ is the translational velocity of the skateboard and ${}^s\dot{\theta}$ is the angular velocity of the skateboard. In order to quantify the collision between the tail and ground, the velocity of the tail normal to the ground, ${}^t v_y$, must be calculated:

$${}^t v_y = {}^s\dot{y} - \frac{1}{2}l_d {}^s\dot{\theta} \cos({}^s\theta) \quad (5.15)$$

where l_d is the length of the deck of the skateboard as defined previously. Denoting the node before and after the collision as $n = n_1$ and $n = n_1 + 1$ respectively, the principles of the conservation of energy in an inelastic collision can be applied to the velocity of the

tail normal to the ground:

$${}^t v_{y,n_1+1} = -e {}^t v_{y,n_1} \quad (5.16)$$

Assuming that the skateboard is still able to rotate about the tail of the skateboard when it is on the ground, it is assumed that there is no loss in rotational kinetic energy during the collision. Using this assumption, the mapping between the velocity state values before and after the collision can be described:

$${}^s \dot{y}_{n_1+1} = -e {}^t v_{y,n_1} + {}^s \dot{y}_{n_1} \quad (5.17)$$

However, using this equation alone to govern the velocity state before and after the collision removes the dependency of \dot{y} on applied forces. This allows the other degrees of freedom of the skateboard, \ddot{x} and $\ddot{\theta}$, to be controlled without affecting the \dot{y} . Therefore, dependence on the applied force is added as follows:

$${}^s \dot{y}_{n_1+1} = -e {}^t v_{y,n_1} + {}^s \dot{y}_{n_1} + {}^m h_n \ddot{y}_{n_1} \quad (5.18)$$

5.4 The Skateboard Wheels and Ground Contact

The aim of developing a method to handle inelastic collisions is to enable the use trajectory optimization to model the contact between the skateboard wheels and the ground. Since this collision is inelastic, the contact-implicit method can be used. This method defines the discontinuities in the problem in terms of complementary relationships. This method can be applied to the inelastic bouncing ball model shown in Figure 5.2B using the following constraints:

$${}^b G_{y,n} {}^B y_{n+1} = p_n \quad (5.19)$$

$${}^B y[n] \geq 0 \quad (5.20)$$

This constraint ensures that the GRF, G_y , can only be applied on the ball when the ball will make contact with the ground in the following node, ensuring that the y-position of the ball will remain above the ground. This is used in conjunction with semi-Euler integration scheme to bring the ball to rest on the ground. The results of the tests of the inelastic bouncing ball dropped from varying heights are shown in Figure 5.7.

It is clear from the results in Figure 5.7 that varying the height of the drop did not effect the overall inelastic response of the ball. However, a very important take-away from this

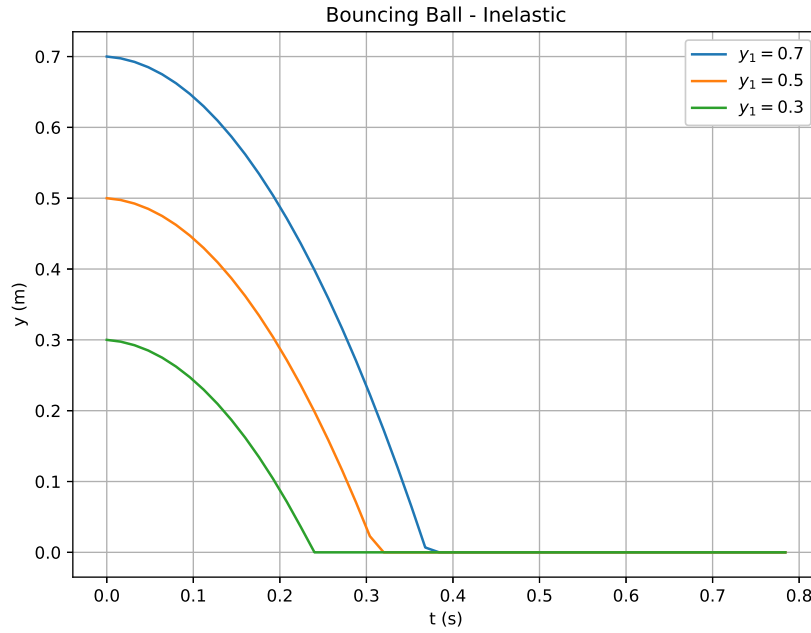


Figure 5.7: The test results of dropping the ball from varying heights using the contact-implicit method. These results are inelastic by nature.

test is that the contact between the ball and the ground did not need to be scheduled. From these results, it is proven that the contact-implicit method can be used to model inelastic collision between the wheels of the skateboard and the ground.

5.5 The Foot and Deck Contact

As has been described previously, the contact between the skateboarder's foot and the skateboard has two defined properties:

1. The skateboarder's foot can exert a force on the skateboard normal to the skateboard at varying positions along the skateboard deck.
2. The skateboarder can slide his foot, generating a friction force between the foot and the deck of the skateboard, parallel to the skateboard deck.

These properties will be developed as follows:

1. The foot-deck normal reaction force was developed using the simple ball model dropping onto the skateboard deck.

2. The reaction force model was then transferred into the skateboard reference frame.
3. The foot-deck friction force was then added to the simple bouncing ball model landing on the skateboard deck.

5.5.1 The Skateboard-Foot Reaction Force

It is trivial to understand that, during the ollie, the skateboarder is able to exert a force downward on the skateboard which, depending where the force is applied, can cause the skateboard to rotate. It should be noted that upon pressing down on the skateboard with one's foot, the foot does not bounce, and thus, this collision appears to be inelastic.

In order to simplistically model this inelastic collision, the familiar bouncing ball model was again used with the contact-implicit method. However, this time, the skateboard was used as the effective “ground” for the ball. The model for the ball-skateboard system is shown in Figure 5.8, where $(^c x, ^c y)$ is the contact point of the ball and the skateboard.

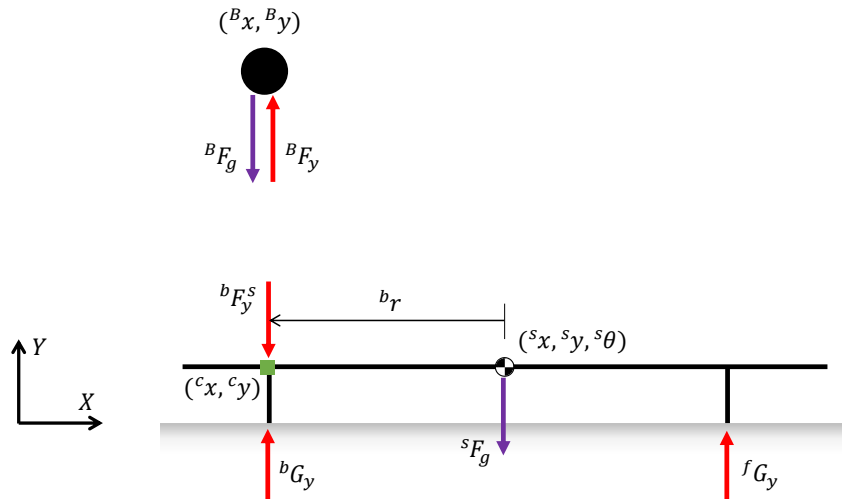


Figure 5.8: The ball-skateboard model used to develop the theory for the reaction force between the skateboard and the ball.

The first test that was conducted involved dropping the ball on the deck of the skateboard with the position of the ball directly above the position of the back wheel, such that $^B x = ^{bw} x$. It is expected that the skateboard should not rotate and the ball should come to rest on the deck of the skateboard.

The complementary constraints and path constraints used for this test are as follows:

$${}^bF_{y,n} = {}^BF_{y,n} \quad (5.21)$$

$${}^bF_{y,n} {}^B y_{n+1} = p_{1,n} \quad (5.22)$$

$${}^bG_{y,n} {}^{bw} y_{n+1} = p_{2,n} \quad (5.23)$$

$${}^fG_{y,n} {}^{fw} y_{n+1} = p_{3,n} \quad (5.24)$$

$${}^Bx_n \leq {}^cx_n \quad (5.25)$$

$${}^By_n \geq {}^cy_n \quad (5.26)$$

The results of the test are shown in Figures 5.9. The ball comes to rest on the deck of the skateboard and the skateboard does not rotate, both of which were desired outcomes.

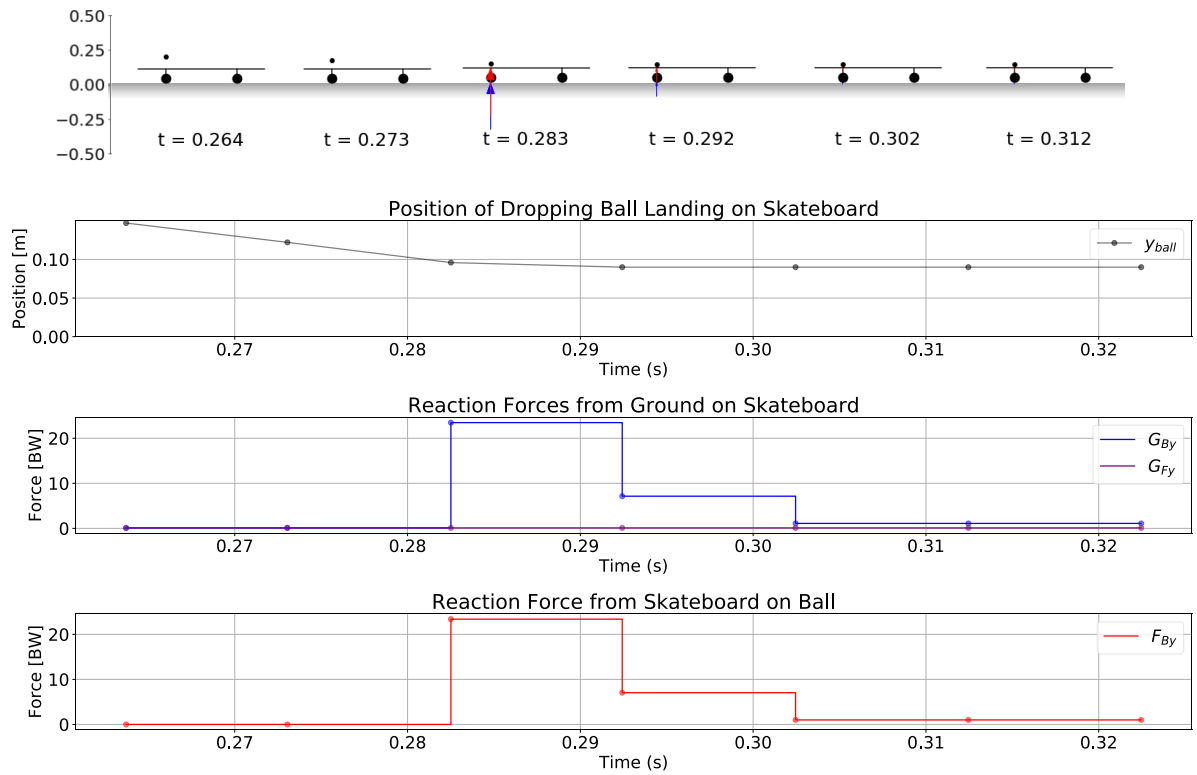


Figure 5.9: Snapshots of the animation of the skateboard-ball test with the corresponding plots of the position of the ball (black), the GRFs on the skateboard (blue and purple) and the reaction force from the skateboard on the ball (red) showing that the contacts are behaving as expected.

But what happens if the ball is dropped closer to the tail of the skateboard? As was mentioned previously, it is intuitive that the skateboard should rotate and the ball should remain on the deck of the skateboard. However, when the skateboard rotates, the point of contact on the skateboard rotates, and thus, finding cx and cy was not as trivial as in the first test, and equation needs to be redefined. To achieve this, the concept of reference

frames needs to be applied to the model.

5.5.2 The Skateboard Reference Frame

The ball-skateboard system has two useful reference frames - the inertial or global reference frame and the skateboard reference frame as shown in Figure 5.10. The method for transforming the coordinates of the ball from the inertial frame, $(^Bx, ^By)$ to the skateboard frame $(^sx, ^sy)$ is detailed below.

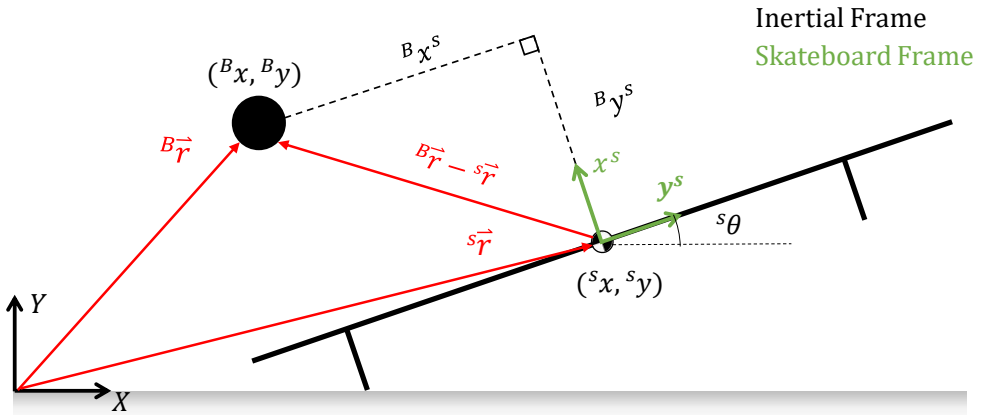


Figure 5.10: A simple diagram of the inertial and skateboard reference frames for the ball-skateboard model. The skateboard frame coordinates are shown in green and the inertial coordinates in black.

The position of the centres of mass of the ball and the skateboard must be expressed in terms of the inertial frame:

$${}^B\vec{r} = \begin{bmatrix} {}^Bx \\ {}^By \end{bmatrix} \quad (5.27)$$

$${}^s\vec{r} = \begin{bmatrix} {}^sx \\ {}^sy \end{bmatrix} \quad (5.28)$$

Now, the difference vector, ${}^3\vec{r}$, can be calculated:

$${}^3\vec{r} = {}^B\vec{r} - {}^s\vec{r} = \begin{bmatrix} {}^Bx - {}^sx \\ {}^By - {}^sy \end{bmatrix} \quad (5.29)$$

The vector ${}^3\vec{r}$ must be rotated by ${}^s\theta$ to transform it into the skateboard frame. This is achieved by applying the rotation matrix:

$${}^3\vec{r}^s = R_z({}^s\theta) {}^3\vec{r} = \begin{bmatrix} \cos({}^s\theta) & \sin({}^s\theta) \\ -\sin({}^s\theta) & \cos({}^s\theta) \end{bmatrix} \begin{bmatrix} {}^Bx - {}^sx \\ {}^By - {}^sy \end{bmatrix} \quad (5.30)$$

$${}^B\vec{r}^s = \begin{bmatrix} ({}^Bx - {}^sx)cos({}^s\theta) + ({}^By - {}^sy)sin({}^s\theta) \\ -({}^Bx - {}^sx)sin({}^s\theta) + ({}^By - {}^sy)cos({}^s\theta) \end{bmatrix} = \begin{bmatrix} {}^Bx^s \\ {}^By^s \end{bmatrix} \quad (5.31)$$

Using this method gives the position of the ball in the skateboard reference frame, ${}^B\vec{r}^s$.

Returning back to the foot-on-deck contact problem simplified to the ball-skateboard model, the perpendicular position of the board, ${}^By^s$, can be used to alter equation for the rotating skateboard problem.

$${}^bF_{y,n}^s {}^B y_{n+1}^s = p_{1,n} \quad (5.32)$$

Furthermore, it can be seen that ${}^cx = {}^Bx^s$ and cy corresponds with ${}^By^s = 0$.

5.5.3 The Skateboard-Foot Friction Force

The next defined foot-deck interaction is the friction force. The model shown in Figure 5.8 can be developed to include the friction force and the normal reaction force. The model is shown in Figure 5.11, where $\phi = {}^By^s$ and ${}^br = {}^Bx^s$.

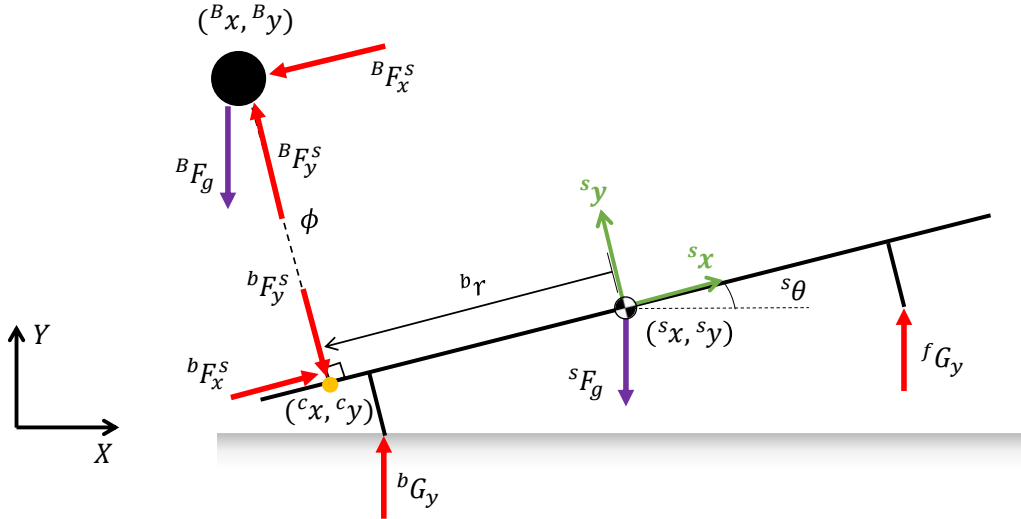


Figure 5.11: The ball-skateboard model with the friction force, ${}^B F_x^s$ and the perpendicular distance between the ball and the skateboard in the skateboard frame, ϕ , added.

The generalized coordinates chosen for the system shown in Figure 5.11 were:

$$q = [{}^Bx, {}^By, {}^sx, {}^sy, {}^s\theta]^\top \quad (5.33)$$

Using these equations, the dynamics of the system were calculated using the Lagrangian

method described previously.

In order to model the ball-deck friction force and the normal reaction force, the contact-implicit method was again used [13]. The first two constraints are imposed on the position of the ball relative to the skateboard deck, and the position of the skateboard wheels relative to the ground. This prevents the skateboard wheels from moving below the ground, and the ball from going through the skateboard deck.

$${}^{bw}\phi_n \geq 0 \quad (5.34)$$

$${}^{fw}\phi_n \geq 0 \quad (5.35)$$

$${}^B\phi_n^s \geq 0 \quad (5.36)$$

where ${}^{bw}\phi_k$ and ${}^{fw}\phi_k$ are the perpendicular distances between the skateboard wheels and the ground, and ${}^B\phi_k^s$ is the perpendicular distance between the ball and the skateboard deck. Conveniently, this can be simplified in the ball-skateboard example to:

$${}^{bw}y_n \geq 0 \quad (5.37)$$

$${}^{fw}y_n \geq 0 \quad (5.38)$$

$${}^B y_n^s \geq 0 \quad (5.39)$$

Since

$${}^{bw}\phi_n = {}^{bw}y_n \quad (5.40)$$

$${}^{fw}\phi_n = {}^{fw}y_n \quad (5.41)$$

$${}^B\phi_n^s = {}^B y_n^s \quad (5.42)$$

where ${}^{bw}y_n$ and ${}^{fw}y_n$ are the y-positions of the wheels in the inertial frame, and ${}^B y_n^s$ is the y-position of the ball in the skateboard frame. In order to implement this constraint, the bounds on the skateboard wheels and y-position of the ball must be enforced by a reaction force. This produces the following constraints:

$${}^{bw}y_n {}^b G_{y,n} = p_{1,n} \quad (5.43)$$

$${}^{fw}y_n {}^f G_{y,n} = p_{2,n} \quad (5.44)$$

$${}^B y_n^s {}^B F_{y,n}^s = p_{3,n} \quad (5.45)$$

where ${}^b G_{y,n}$ and ${}^f G_{y,n}$ are the GRFs acting on the skateboard wheels, and ${}^B F_{y,n}^s$ is the reaction force between the skateboard deck and the ball acting on the ball in the

skateboard frame. The next constraints limit the magnitude of the friction force between the ball and the skateboard deck using the coefficient of static friction and slack variables. The friction force can be resolved into the following slack variables:

$${}^B F_{x,n}^s = {}^B F_{x,n}^{s+} - {}^B F_{x,n}^{s-} \quad (5.46)$$

$${}^B F_{x,n}^{s+}, {}^B F_{x,n}^{s-} \geq 0 \quad (5.47)$$

where ${}^B F_{x,n}^s$ is the friction force on the ball in the skateboard frame, and ${}^B F_{x,n}^{s+}$ and ${}^B F_{x,n}^{s-}$ result from resolving the friction force into positive and negative components. Applying the principles of the coefficient of static friction, the following constraints are derived to create a friction cone:

$$\mu_s {}^B F_{y,n}^s - {}^B F_{x,n}^{s+} - {}^B F_{x,n}^{s-} \geq 0 \quad (5.48)$$

$${}^B F_{y,n}^s \geq 0 \quad (5.49)$$

where μ_s is the coefficient of static friction and ${}^B F_{y,n}^s$ is the reaction force between the ball and the skateboard, acting on the ball. The tangential velocity of the ball in the skateboard frame can be resolved into positive and negative components:

$${}^B \dot{x}_{x,n}^s = {}^B \dot{x}_{x,n}^{s+} - {}^B \dot{x}_{x,n}^{s-} \quad (5.50)$$

where ${}^B \dot{x}_{x,n}^s$ is the x-velocity of the ball in the skateboard frame. Using equations (5.50), the relationship between the friction cone and the tangential velocity of the ball can be defined by the following constraints:

$${}^B \dot{x}_{x,n}^{s+}, {}^B \dot{x}_{x,n}^{s-} \geq 0 \quad (5.51)$$

$$(\mu_s {}^B F_{y,n}^s - {}^B F_{x,n}^{s+} - {}^B F_{x,n}^{s-})({}^B \dot{x}_{x,n}^{s+} + {}^B \dot{x}_{x,n}^{s-}) = p_{4,n} \quad (5.52)$$

$${}^B \dot{x}_{x,n}^{s+} {}^B F_{x,n}^{s+} = p_{5,n} \quad (5.53)$$

$${}^B \dot{x}_{x,n}^{s-} {}^B F_{x,n}^{s-} = p_{6,n} \quad (5.54)$$

These equations ensure that the ball's tangential velocity can only be non-zero if there is a normal force and if the friction force is greater than the maximum static friction force - Equation (5.52) - and that the friction can only act in the opposite direction to the tangential velocity of the ball - Equations (5.53-5.54).

It can be seen from the animation snapshots and the plots in Figure 5.12 that all of the above mentioned constraints are indeed working:

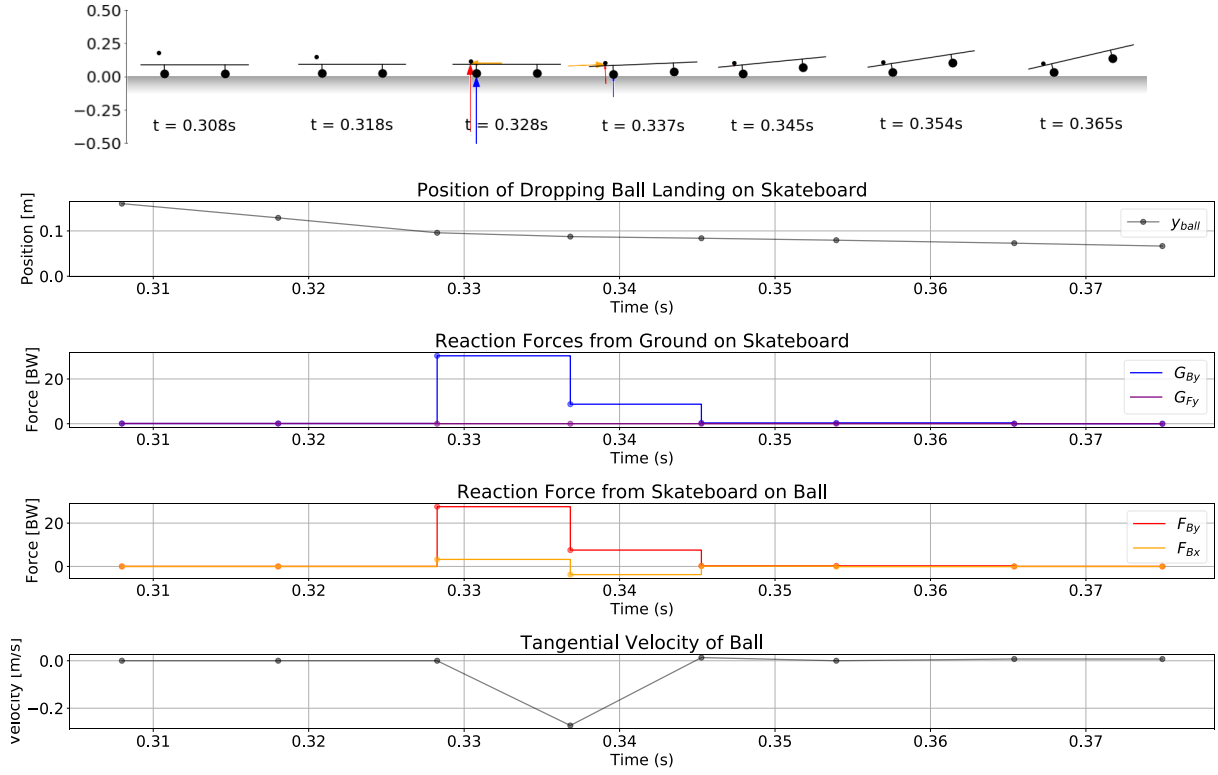


Figure 5.12: Snapshots of the dropping ball test with the corresponding plots of the position and tangential velocity of the ball (black), the GRFs (blue and purple), the skateboard reaction force on the ball (red) and the friction force between the skateboard and the ball (orange) showing that all the contacts are behaving as expected.

- the reaction force between the skateboard and the ball becomes non-zero at the node immediately before the ball lands on the board,
- the GRF acting on the wheels is equal to the weight of the skateboard until the ball makes contact with the skateboard, at which point it increases to remain on the ground.
- the friction force is only non-zero when there is a normal force between the ball and the skateboard,
- the ball has no tangential velocity on the skateboard when the friction force is less than the maximum static friction force,
- the friction force on the skateboard is in the same direction as the skateboard's relative velocity and in the opposite direction to the ball's tangential velocity when the ball is sliding.

5.6 The Ground Function

For the SO and RO manoeuvres, it is sufficient to model the ground as the global position which corresponds with $Y = 0$. However, for the OU and OD manoeuvres, this simplification is not applicable - a ground function of sorts is needed to be introduced in order to model a step in the ground.

Denoting the height of the step as Y_s and the position of the step as X_s , a complementary relationship can be formulated to create a ground function. Firstly, the x-position of the ball should be resolved into positive and negative components as follows:

$${}^Bx^+, {}^Bx^- \geq 0 \quad (5.55)$$

$${}^Bx - X_s = {}^Bx^+ - {}^Bx^- \quad (5.56)$$

Now, the ground function, G_F , bounds can be defined:

$$0 \leq G_F \leq Y_s \quad (5.57)$$

A complementary relationship can now be formulated to set the value of the ground function depending on the x-position of the ball:

$$G_{F,n} {}^Bx_n^- = p_{1,n} \quad (5.58)$$

$$(Y_s - G_{F,n}) {}^Bx_n^+ = p_{2,n} \quad (5.59)$$

This complementary relationship ensures that, when ${}^Bx \leq X_s$, $G_{F,n} = 0$, and when ${}^Bx \geq X_s$, $G_{F,n} = Y_s$. A new complementary relationship should also be formulated to ensure the ball does not drop below the ground function. Defining the position of the ball above the ground function as ${}^By^G$, the following complementary relationship can be defined:

$${}^By_{n+1}^G G_{y,n} = p_{3,n} \quad (5.60)$$

These complementary relationships were formulated into the optimization problem in order to test whether this method would indeed model a ground-step. The results of the ground-step test are shown in Figure 5.13.

It is evident from the results shown in Figure 5.13 that the ground function has been implemented correctly. The GRF acts on the node before the ball reaches the ground function which brings the ball to rest on the ground and on the step.

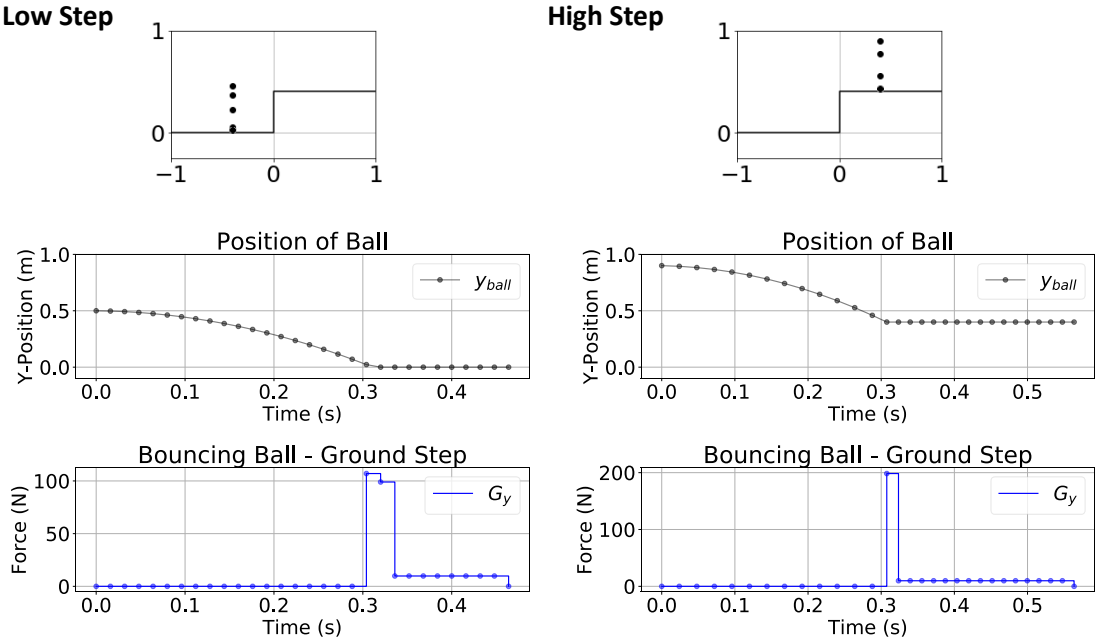


Figure 5.13: The results of the ball-ground drop test showing the simulated results and trajectories of the low-step and high-step.

This test proves that the ground function can be modelled using the complementary constraints implemented in this problem. This will be useful for modelling the wheel-ground contact during the OU and OD manoeuvres.

Using the contact-implicit and hybrid dynamic methods that have been developed, implemented and successfully tested over various tests for the interaction of multi-body systems using the bouncing ball and skateboard model, the mathematical models of the skateboard and skateboarder, and the trajectory optimization problem can be developed.

5.7 Development of the Skateboarder Model and the Ollie

Now that the different contact methods have been explored for the interaction between the skateboard and skateboarder, a model for the skateboarder-skateboard system can be developed to encapsulate the key elements of a skateboarder. The trajectory optimization problem can also be developed to generate a trajectory that replicates the ollie manoeuvre.

Developing models for the skateboard and skateboarder is a vital aspect of this project. The models need to encompass the physical dynamics of the real-world bodies while ensuring the complexity of the models is minimized. An iterative design approach was

5.7. DEVELOPMENT OF THE SKATEBOARDER MODEL AND THE OLLIE

used to develop the models and the desired trajectory. For every iteration, a model was developed, a trajectory optimization problem was posed, and the results were recorded. An overview of the iterative stages of development of the skateboarder-skateboard system is shown in Figure 5.14.

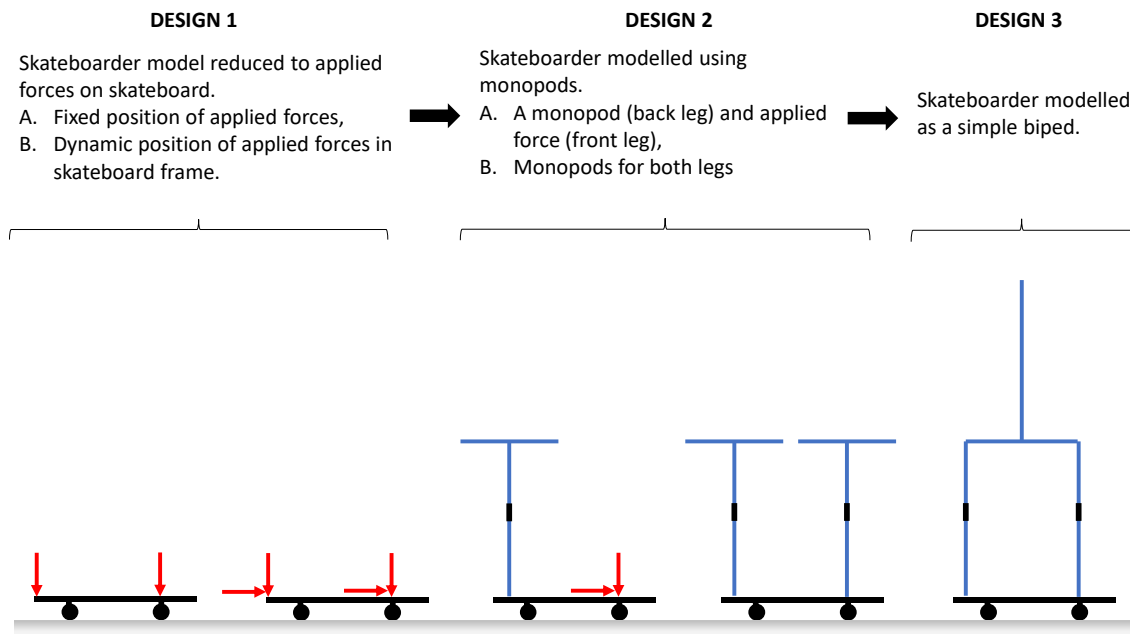


Figure 5.14: Stages of development of the skateboarder-skateboarder model used to generate the ollie manoeuvre using trajectory optimization.

5.7.1 Design 1: Fixed Position of the Applied Forces on the Skateboard

Aim of Design

The aim of the first design iteration of the skateboard-skateboarder system was to determine whether, through the application of trajectory optimization, the trajectory of the most basic model of the system could indeed replicate the ollie. The aspects of the system that were to be isolated and tested are:

1. The applied forces on the back and front of the skateboard.
2. The contact between the ground and the skateboard wheels.

Modeling the System

To achieve this aim, the system model was simplified using the following design decisions:

1. The skateboarder-skateboard interaction was reduced to applied forces acting on the skateboard representing the interactions between the skateboarder's feet and the skateboard. Forces in both the inertial x and y directions were considered.
2. The positions of the applied forces along the skateboard were fixed.

The simplified system is shown in Figure 5.15, where bF_x and bF_y are the back-foot applied forces acting at fixed position b_r . fF_x and fF_y are the front-foot applied forces acting at fixed position f_r , and bG_y and fG_y are the GRFs acting on the back and front wheels. The positions of the back and font-foot forces were fixed relative to the centre of the skateboard as follows:

$${}^b_r = 0.5 {}^d l = 40\text{cm} \quad (5.61)$$

$${}^f_r = 0.5 {}^d l = 40\text{cm} \quad (5.62)$$

This corresponds with the positions of the tail and the nose relative to the skateboard, respectively. The generalized coordinates of the system were chosen as:

$${}^s\mathbf{q} = [{}^s x, {}^s y, {}^s \theta]^\top \quad (5.63)$$

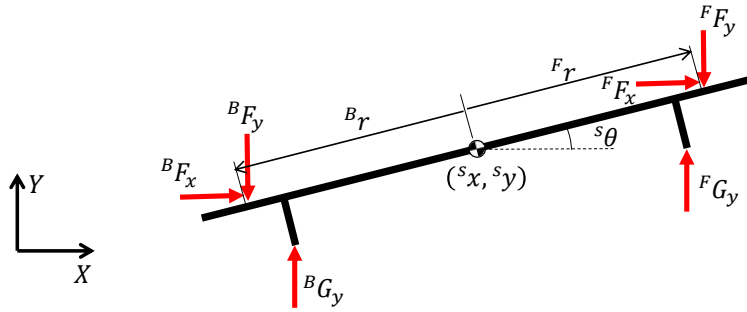


Figure 5.15: Design 1: the skateboarder is modelled as applied forces on the skateboard acting in the inertial reference frame. The positions of the applied forces are fixed at the nose and tail of the skateboard.

The Trajectory Optimization Problem

The trajectory optimization problem was formulated for the design with $N = 50$ nodes with $h_m = 0.01s$. The dynamics were integrated using the semi-Euler method.

Contacts

The discontinuous state mapping that occurs when the tail strikes the ground was designated to occur at $n = 10$. The state mapping was defined as follows:

$${}^s \dot{y}_{10} = e {}^t v_{y,9} + {}^s \dot{y}_9 + {}^m h_{10} {}^s \ddot{y}_9 \quad (5.64)$$

where ${}^t v_y$ is the y-velocity of the tail in the inertial frame, and $e = -0.6$.

The inelastic collision between the wheels and the ground was modeled using the contact-implicit method developed previously. The complementary relationships were specified as:

$${}^{bw} y_{n+1} {}^b G_{y,n} = p_{1,n} \quad (5.65)$$

$${}^{fw} y_{n+1} {}^f G_{y,n} = p_{2,n} \quad (5.66)$$

where ${}^{bw} y_{n+1}$ and ${}^{fw} y_{n+1}$ are the positions of the back and front wheels above the ground in the next node respectively.

Variable Bounds

The variable bounds used for the optimization problem for design 1 are shown in Table 5.1 below.

Table 5.1: The variable bounds for design 1. S=100N.

Variable	Lower Bound	Upper Bound	Unit
$^s x$	-	0.5	m
$^{bw} y, ^{fw} y$	0.0	-	m
$^n y, ^t y$	0.0	-	m
$^s \theta$	$-\frac{\pi}{2}$	$\frac{\pi}{2}$	rad
$^b F_x, ^f F_x$	0.0	5.0	S
$^b F_y, ^f F_y$	0.0	5.0	S
$^b G_y, ^f G_y$	0.0	20.0	S
$p_{1,n}, p_{2,n}$	0.0	-	-

The bound on $^s x$ ensures that $^b F_x$ and $^f F_x$ do not overpower the motion of the system; the bounds on $^{bw} y$, $^{fw} y$, $^n y$, $^t y$ restrict the position of the wheels, nose and tail of the skateboard to above the ground; $^s \theta$ is bounded to ensure the skateboard does not rotate past $\pi/2$; the applied forces, $^b F_x$, $^f F_x$ and $^b F_y$, $^f F_y$, are bounded to replicate how a skateboarder can only push down and forward on the skateboard with his feet; and the bounds were placed on $^b G_y$ and $^f G_y$ since the ground reaction should only act away from the ground.

The Objective Function

The objective function needed include both the force and penalty terms to ensure the applied force and penalty terms were optimally minimised. Therefore, the objective function was chosen as follows:

$$J_F = \sum_{n=1}^N ((^b F_{x,n})^2 + (^b F_{y,n})^2 + (^f F_{x,n})^2 + (^f F_{y,n})^2) \ ^m h_n \quad (5.67)$$

$$J_P = \sum_{n=1}^N p_{1,n} + p_{2,n} \quad (5.68)$$

$$J = J_F + 1000J_P \quad (5.69)$$

The penalty scaling factor was chosen as 1000 to ensure the penalty was sufficiently minimized in the cost function.

Path Constraints:

Considering phases of the ollie manoeuvre described previously, and the expected timing of when the transitions between the phases should occur, the path constraints, shown in Table 5.2 below, were generated. The phases of the ollie were broken down into a standing phase (prior to the “pop”), a “pop” phase (when the skateboard tail strikes the ground), an apex phase (when the skateboard reaches maximum height), a landing phase (when

the skateboard wheels make contact with the ground), and finally a steady phase (when the skateboarder's feet are on the skateboard and the skateboard is on the ground). The steady phase will be further considered when a skateboarder model is introduced.

Table 5.2: The path constraints for designs 1 and 2.

Phase	Node	Variable Constraints	Unit
Standing	1	$^{bw}x = 0.0$	m
		$^{bw}y = 0.0$	m
		$^s\theta = 0.0$	rad
		$^s\dot{q} = 0.0$	-
“Pop”	9	$^t y = 0.0$	m
Apex	27	$^{bw}y \geq 0.5$	m
		$^{fw}y \geq 0.5$	m
Landing	45	$^{bw}y = 0.0$	m
		$^s\theta = 0.0$	m
Steady	50	$^{bw}y = 0.0$	m
		$^s\theta = 0.0$	rad

Results and Discussion

The results of the test are shown in Figure 5.16, displaying both the observed simulation results and various force profiles.

It can be seen from the snapshots of the observed simulation results that the state trajectory of the skateboard was roughly what was expected. The skateboard rotates about its back wheel, then “pops” off the ground, steadies the skateboard in the air, and then lands. It should also be noted that the simulated manoeuvre is 0.48s in length, which is approximately the expected time to perform the manoeuvre. Interestingly, the front and back wheels of the skateboard do not land on the ground at the same time. The force profiles shown serve to show the forces involved in performing the ollie. The profiles will not be closely analysed for this test, however, it is worth noticing that the complementary relationship between the ground and the wheels is working as desired.

These results, therefore, demonstrated that:

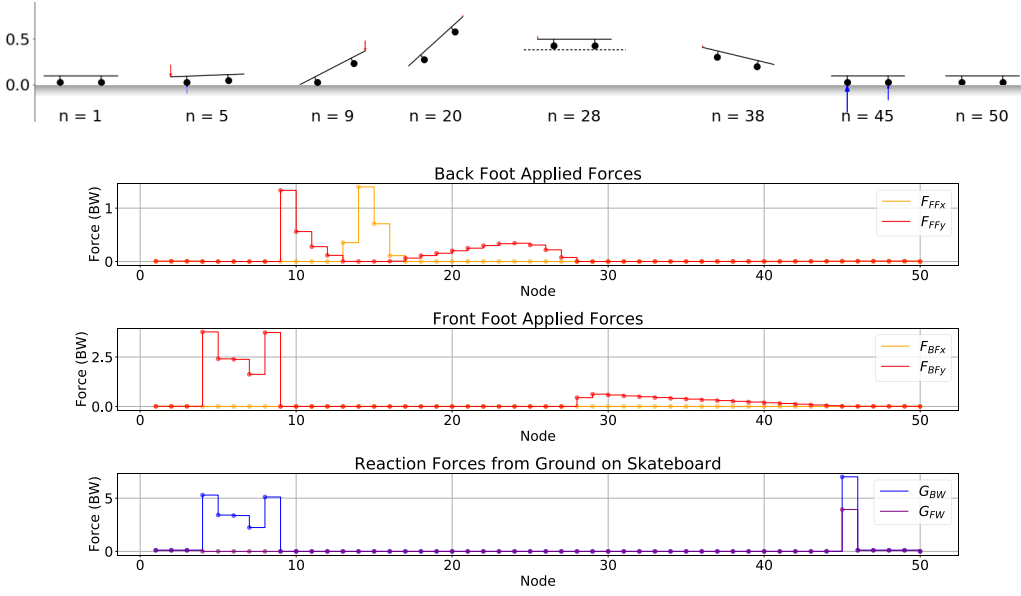


Figure 5.16: The solved results for the first design, showing the visual simulation results and force profiles.

1. The basic skateboard-skateboarder model, where the skateboard-skateboarder interaction is reduced to fixed position applied forces on the skateboard, is able to replicate the ollie manoeuvre.
2. The tail-ground contact and wheel-ground contacts have been successfully implemented.

However, there are limitations of this model that should be considered in the next design iteration in order to develop a more complete skateboard-skateboarder system. These are as follows:

1. The applied forces are at a fixed position on the skateboard. The model should be developed to allow the applied forces to move along the length of skateboard.
2. The applied forces act in the inertial frame. In order to model the foot-deck reaction force and friction force, the applied forces should be transformed into the skateboard frame.

5.7.2 Design 2: Dynamic Position of the Applied Forces on Skateboard

Aim of Design

The aim of the second design iteration is to allow the applied forces on the skateboard to move along the surface of the skateboard and to resolve the forces into the skateboard frame. The forces should be resolved into the skateboard frame to model the foot-deck reaction force and the foot-deck friction force. It is expected that the position of the applied forces should move towards the tail and nose of the skateboard when maximum rotation is required in the manoeuvre. The aspects of the system that are to be isolated and tested are:

1. The friction and reaction forces between the skateboarder's feet and the deck of the skateboard.
2. The movement of the applied forces along the skateboard as the skateboarder moves their feet.

Modeling the System

The overall simplification of the skateboard-skateboarder system is similar to design 1, however the following alterations were made:

1. The applied forces representing the skateboarder-skateboard interaction were defined in the skateboard reference frame.
2. The positions of the applied forces along the skateboard were not fixed, however, they were constrained to move over the length of the skateboard.

The simplified system is shown in Figure 5.17, where ${}^bF_x^s$ and ${}^bF_y^s$ are the back-foot applied forces acting at variable position b_r , ${}^fF_x^s$ and ${}^fF_y^s$ are the font-foot applied forces acting at variable position f_r , and bG_y and fG_y are the GRFs on the front and back wheels of the skateboard.

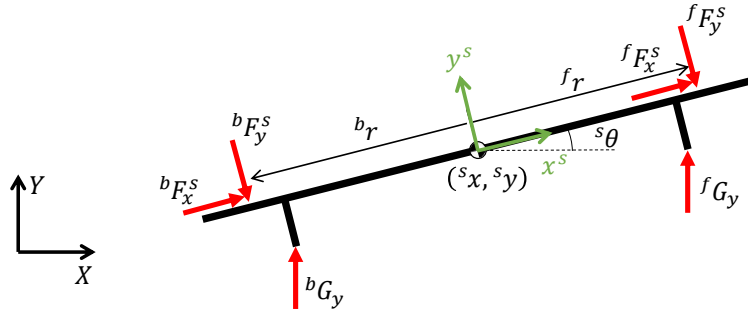


Figure 5.17: Design 2: the skateboard-skateboarder system is modelled as applied forces on the skateboard acting in the skateboard reference frame which are constrained to move along the length of the skateboard.

The Trajectory Optimization Problem

The same initial setup of the optimization problem described in design 1 was used for this problem, in terms of the number of nodes, discontinuous state mapping and generalized coordinates. Furthermore, the path constraints used were the same as the path constraints used in design 1 (Table 5.2) and the ground-wheel contact was handled using the same through-contact method.

Variable Bounds

The same variable bounds were used for design 2 as were used in design 1 (Table 5.1), however an additional constraint was added to constrain the position of the applied forces on the skateboard between the centre of the skateboard and the length of the skateboard. The additional constraint is shown below in Table 5.1.

Table 5.3: The variable bounds for design 2. S=100N.

Variable	Lower Bound	Upper Bound	Unit
b_r, f_r	0	0.4	m

The Objective Function

The objective function is similar to the objective function used in design 1, however, the force term has been redefined in the skateboard frame. Therefore, the objective function was chosen as follows:

$$J_F = \sum_{n=1}^N (({}^b F_{x,n}^S)^2 + ({}^b F_{y,n}^S)^2 + ({}^f F_{x,n}^S)^2 + ({}^f F_{y,n}^S)^2) {}^m h_n \quad (5.70)$$

$$J = J_F + 1000J_P \quad (5.71)$$

Results and Discussion

The solver converged to a locally optimal solution with the total penalty violation at 5.86×10^{-9} . The results for the second design, shown in Figure 5.18, are exceedingly similar to the results obtained for the first design when comparing the observed trajectory of the model, but relatively different in the force profiles. It is still evident that the trajectory of the model clearly replicates trajectory that the skateboard would follow while performing an ollie.

It can also be seen in Figure 5.18 that the force is able to move along the skateboard between between the given bounds. It should also be noted that, in order to be optimal, the position of the applied force is usually on the tail or nose of the skateboard when there is a large force being applied.

Again, the force profiles are not the focus of this test, but rather, they confirm that the ground-wheel contact has again been implemented correctly.

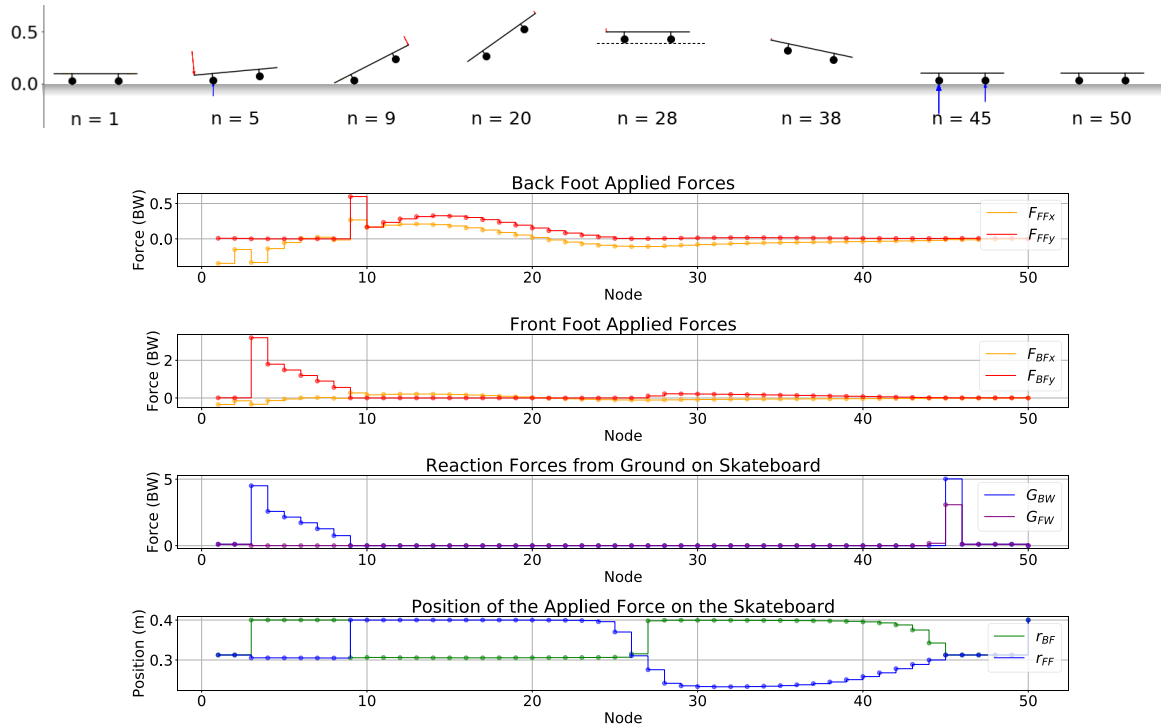


Figure 5.18: The solved results for the second design, showing the visual simulation results and force profiles.

It has been demonstrated in this test that:

1. The trajectory of the ollie manoeuvre can be replicated using a simple skateboard model with applied forces acting perpendicular and parallel to the skateboard.

5.7. DEVELOPMENT OF THE SKATEBOARDER MODEL AND THE OLLIE

2. The position of the front and back-foot applied forces can be defined as decision variables which are constrained to move along the length of the skateboard.

The limitations of this design and aspects that should be developed are as follows:

1. This model has used applied forces to model the foot-deck contact, however, the force between the skateboarder's feet and the deck of the skateboard are reaction forces and friction forces, and thus, a model of the skateboarder should be developed that can induce these forces.
2. The position of the applied forces was defined as a decision variable, however, it is desirable that this position is defined as the contact position between the skateboarder's foot and the skateboard deck.

5.7.3 Design 3: Monopods on Skateboard

Aim of Design

Since the skateboard model has been proven to replicate the ollie, focus should be shifted onto modeling the skateboarder. Thus, the aim of the third design iteration is to model a basic actuated skateboarder that is able to apply forces on the skateboard deck which induce a reaction force on the skateboard and the foot of the model. Furthermore, the skateboarder model should be able to move along the skateboard and leave the deck of the skateboard. The aspects of the system that are to be isolated and tested are:

1. The reaction forces between the skateboarder's feet and the deck of the skateboard which are induced through actuation of the skateboarder's feet onto the skateboard.
2. The friction forces between the skateboarder's feet and the deck of the skateboard which are induced by the movement of the skateboard model's foot.
3. The position of the skateboarder model's feet should be able to leave the skateboard and move along the length of the skateboard.

Modeling the System

The skateboard model used in design 2 (Figure 5.17) has successfully proven that it has the capabilities of replicating the ollie, thus, this model was used as the skateboard model. The skateboarder was modelled initially as a monopod representing the skateboarder's back leg and an applied force on the skateboard, and then, once that had been successfully implemented, as two monopods representing the skateboarder's back and front legs. Both monopods were modelled as a kinematic chain of rigid-links with a prismatic joint at the knee. The physical properties of the model is shown in Figure 5.19, and the chosen actuators and coordinates are shown in Figure 5.20.

The physical properties of the monopod were chosen to, on a basic level, encompass the properties of the human leg of the the skateboarders that participated in the studies by Frederick, Determan and Leuchanka [2][?][32] in terms of the dimensions and masses of the links. The chosen physical properties of the monopods are shown below in Table 5.4.

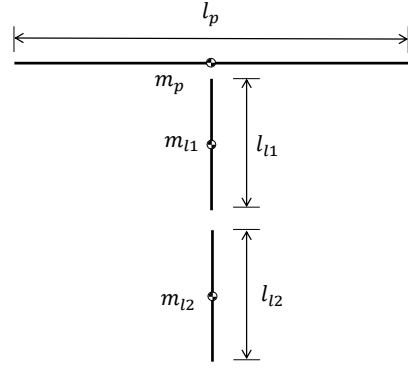


Figure 5.19: The dimensions and mass conventions of design 3.

Table 5.4: The chosen variable values of the monopod model.

Variable	Value	Unit
m_p	5.0	kg
m_{l1}	2.5	kg
m_{l2}	2.5	kg
l_p	1.0	m
l_{l1}	0.5	m
l_{l2}	0.5	m

The skateboarder's back and front legs were modeled as independent monopods. To model the hip joint of the human, the monopod has an actuator at the pelvis-leg joint, $p_1\tau$ and $p_2\tau$, which can apply a torque on the links. The human knee was modeled as a prismatic joint which can adjust the leg length, $^b r_k$ and $^f r_k$, by applying a force, $^b F_a$ and $^f F_a$, at the knee joint. A reaction force, $^b F_r$ and $^f F_r$ was added to the prismatic joint to enforce a hard-stop on the knee joint when the leg extends or retracts to its length limits. The position of the front and back feet were defined as $(^b x, ^b y)$ and $(^f x, ^f y)$, shown in pink in Figure 5.20.

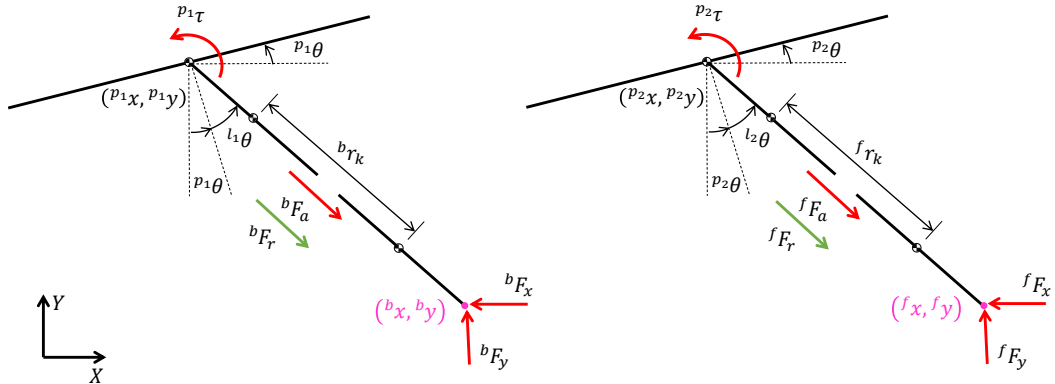


Figure 5.20: The coordinates and actuators of the monopods used in design 3 to model the skateboarder. The positions of the front and back feet are shown in pink, and the hard-stop reaction forces in the prismatic joints are shown in green.

The Trajectory Optimization Problem

The trajectory optimization problem has two new aspects that must be formulated into the problem: 1) the skateboarder subsystem modelled as two monopods, and 2) the foot-deck contact. For this problem, it was chosen that $N = 60$ with $h_m = 0.01s$. The generalized coordinates chosen to describe the skateboard-skateboarder system shown in Figure 5.17 and 5.20 are as follows:

$$\mathbf{q} = [{}^s x, {}^s y, {}^s \theta, {}^{p_1} x, {}^{p_1} y, {}^{p_1} \theta, {}^{l_1} \theta, {}^b r_k, {}^{p_2} x, {}^{p_2} y, {}^{p_2} \theta, {}^{l_2} \theta, {}^f r_k]^\top \quad (5.72)$$

Since the trajectory optimization problem has now been setup, the contacts can now be formulated.

Contacts

The contacts involved within the system as it has been modeled are 1) the contacts between the skateboard wheels and the ground, 2) the contact between the skateboard tail and the ground, 3) the contact between the back and front feet and the skateboard deck, and 4) the hard-stop enforced at the knee joint of the monopod. Both contact (1) and (2) have been implemented successfully in design 1 and 2, however, contact (3) and (4) have not been implemented as of yet.

The foot-deck contact can be broken into two parts - foot-deck reaction force, and the friction force opposing the motion of the foot on the deck. In order to model these contacts, the contact-implicit method, as explained in equations (3.54 - 3.60) provided by Posa [13], was implemented. This has already been successfully implemented for the ball-deck contact detailed previously, and thus, the same steps will be taken.

Before continuing, it is worth stating a basic principle of bodies interacting with each other. When two bodies make contact, the forces experienced by the one body is equal in magnitude and opposite in direction to the force experienced by the other body. This is shown in Figure 5.21 where this relationship is explained with the foot-deck reaction and friction forces.

Denoting the velocity of the back and front feet relative to the skateboard (in the skateboard frame) as ${}^b v^s$ and ${}^f v^s$, it is shown in Figure 5.21 that the following relationship is evident:

$${}^b v^s = {}^b \dot{x}^s \quad (5.73)$$

$${}^f v^s = {}^f \dot{x}^s \quad (5.74)$$

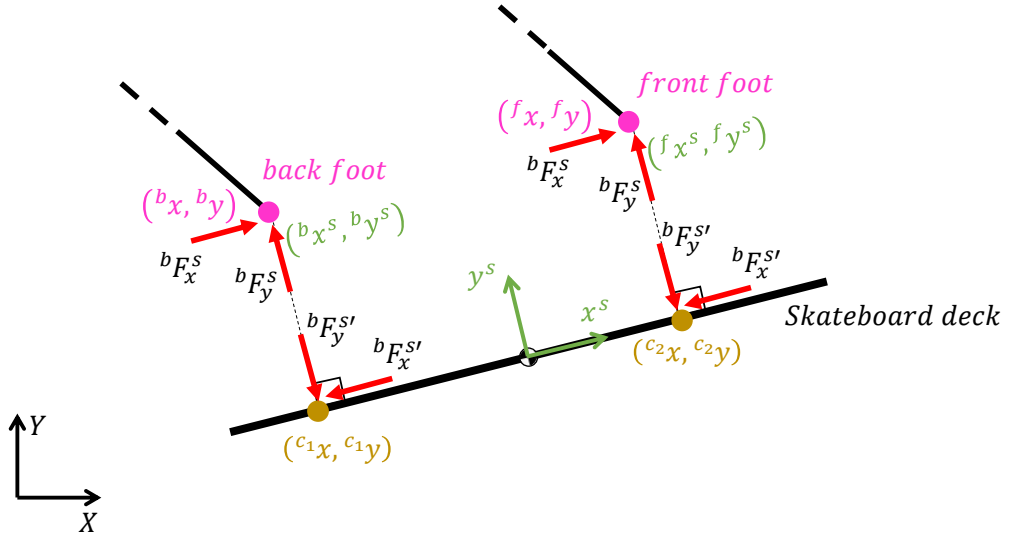


Figure 5.21: An illustration of the monopods' feet and the foot-deck contact: the positions of the feet are shown in pink; the position of the feet in the skateboard frame is shown in green; the expected position of contact of the foot on the deck is shown in yellow; and the foot deck reaction forces are shown in red.

Using this relationship, the relative velocities can be decomposed into positive and negative components at each node:

$${}^b\dot{x}_n^{s+}, {}^b\dot{x}_n^{s-}, {}^f\dot{x}_n^{s+}, {}^f\dot{x}_n^{s-} \geq 0 \quad (5.75)$$

$${}^b\dot{x}_n^s = {}^b\dot{x}_n^{s+} - {}^b\dot{x}_n^{s-} \quad (5.76)$$

$${}^f\dot{x}_n^s = {}^f\dot{x}_n^{s+} - {}^f\dot{x}_n^{s-} \quad (5.77)$$

Similarly, the foot-deck friction force can be segmented into positive and negative components:

$${}^bF_{x,n}^{s+}, {}^bF_{x,n}^{s-}, {}^fF_{x,n}^{s+}, {}^fF_{x,n}^{s-} \geq 0 \quad (5.78)$$

$${}^bF_{y,n}^{s+}, {}^bF_{y,n}^{s-}, {}^fF_{y,n}^{s+}, {}^fF_{y,n}^{s-} \geq 0 \quad (5.79)$$

$${}^bF_{x,n}^s = {}^bF_{x,n}^{s+} - {}^bF_{x,n}^{s-} \quad (5.80)$$

$${}^fF_{x,n}^s = {}^fF_{x,n}^{s+} - {}^fF_{x,n}^{s-} \quad (5.81)$$

$${}^bF_{y,n}^s = {}^bF_{y,n}^{s+} - {}^bF_{y,n}^{s-} \quad (5.82)$$

$${}^fF_{y,n}^s = {}^fF_{y,n}^{s+} - {}^fF_{y,n}^{s-} \quad (5.83)$$

Furthermore, since the reaction force normal to the skateboard can only act away from the skateboard deck, the following simplification can be made:

$${}^bF_{y,n}^{s-} = 0 \quad (5.84)$$

$${}^fF_{y,n}^{s-} = 0 \quad (5.85)$$

The friction cone can now be added as a constraint to define the relationship between the maximum static friction and the friction force:

$$\mu {}^b F_{y,n}^{s+} - {}^b F_{x,n}^{s+} - {}^b F_{x,n}^{s-} \geq 0 \quad (5.86)$$

$$\mu {}^f F_{y,n}^{s+} - {}^f F_{x,n}^{s+} - {}^f F_{x,n}^{s-} \geq 0 \quad (5.87)$$

where the coefficient of static friction, μ , was chosen as 0.78 as justified previously. Using this friction cone, a complementary constraint can be added to ensure the foot can only slide along the skateboard deck if the friction force is greater than the maximum static friction:

$$(\mu {}^b F_{y,n}^{s+} - {}^b F_{x,n}^{s+} - {}^b F_{x,n}^{s-})({}^b \dot{x}_n^{s+} + {}^b \dot{x}_n^{s-}) = p_{3,n} \quad (5.88)$$

$$(\mu {}^f F_{y,n}^{s+} - {}^f F_{x,n}^{s+} - {}^f F_{x,n}^{s-})({}^f \dot{x}_n^{s+} + {}^f \dot{x}_n^{s-}) = p_{4,n} \quad (5.89)$$

Furthermore, the friction force should only be able to act in the opposite direction to the relative motion of the foot and the skateboard, therefore another complementary constraint should be added:

$$({}^b \dot{x}_n^{s+})({}^b F_{x,n}^{s+}) = p_{5,n} \quad (5.90)$$

$$({}^b \dot{x}_n^{s-})({}^b F_{x,n}^{s-}) = p_{6,n} \quad (5.91)$$

$$({}^f \dot{x}_n^{s+})({}^f F_{x,n}^{s+}) = p_{7,n} \quad (5.92)$$

$$({}^f \dot{x}_n^{s-})({}^f F_{x,n}^{s-}) = p_{8,n} \quad (5.93)$$

This set of constraints is sufficient to model the foot-deck friction force. To model the reaction force between the foot and deck, normal to the skateboard deck, the contact-implicit method, as used for the ball-deck example previously, was again implemented.

The first variable needed is the perpendicular distance between the foot and the skateboard. By transforming the position of the foot into the skateboard reference frame, this distance simply becomes ${}^b y^s$ and ${}^f y^s$, as shown in Figure 5.21. Applying the constraint given in equation (3.57) to this problem, the following constraint is created:

$$({}^b y_{n+1}^s)({}^b F_{y,n}^{s+}) = p_{9,n} \quad (5.94)$$

$$({}^f y_{n+1}^s)({}^f F_{y,n}^{s+}) = p_{10,n} \quad (5.95)$$

Critically, it should be noted that, since the integration method that was chosen was semi-Euler, the back foot-deck reaction force, ${}^b F_y^{s+}$, must be indexed the node before the

back foot is going to strike the deck (i.e. when ${}^b y^s = 0$) to enable the force to cause the back foot to decelerate to land on the deck. The same applies for the front foot.

Finally, since the point of contact on the skateboard occurs at the point $({}^{c_1}x, {}^{c_1}y)$ and $({}^{c_2}x, {}^{c_2}y)$ as shown in Figure 5.21, the position of the reaction forces on the skateboard are now defined as follows:

$${}^b r_n = |{}^b x_n^s| \quad (5.96)$$

$${}^f r_n = |{}^f x_n^s| \quad (5.97)$$

To model the prismatic joint, it is necessary to include the hard-stop constraint at the knee. This constraint uses the reaction forces at the knee, ${}^b F_r$ and ${}^f F_r$, to enforce variable bounds on the length of ${}^b r_k$ and ${}^f r_k$. Denoting the upper and lower bounds of ${}^b r_k$ and ${}^f r_k$ as ${}^b r_{k(upp)}$ and ${}^b r_{k(low)}$, and ${}^f r_{k(upp)}$ and ${}^f r_{k(low)}$, a complementary relationship can be introduced to enforce the hard-stop constraint:

$$({}^b r_{k(upp)} - {}^b r_{k,n+1})({}^b F_{r,n}^-) = p_{11,n} \quad (5.98)$$

$$({}^b r_{k,n+1} - {}^b r_{k(low)})({}^b F_{r,n}^+) = p_{12,n} \quad (5.99)$$

$$({}^f r_{k(upp)} - {}^f r_{k,n+1})({}^f F_{r,n}^-) = p_{13,n} \quad (5.100)$$

$$({}^f r_{k,n+1} - {}^f r_{k(low)})({}^f F_{r,n}^+) = p_{14,n} \quad (5.101)$$

where the hard-stop reaction force is decomposed into positive and negative components:

$${}^b F_{r,n}^+, {}^b F_{r,n}^-, {}^f F_{r,n}^+, {}^f F_{r,n}^- \geq 0 \quad (5.102)$$

$${}^b F_{r,n} = {}^b F_{r,n}^+ - {}^b F_{r,n}^- \quad (5.103)$$

$${}^f F_{r,n} = {}^f F_{r,n}^+ - {}^f F_{r,n}^- \quad (5.104)$$

Variable Bounds

The variable bounds used for the optimization problem for design 3 are shown in Table 5.1 below. The variable bounds needed to implement the contact-implicit method for the foot-deck contact are the bounds on ${}^b y_n^s$ and ${}^f y_n^s$ which restrict the feet trajectories to above the skateboard deck, and ${}^b x_n^s$ and ${}^f x_n^s$ which restrict the motion of the feet to the length of the skateboard. Additionally, the bounds used to enforce the hard-stop within the prismatic joint are the bounds on ${}^b r_{k,n}$ and ${}^f r_{k,n}$.

Table 5.5: The variable bounds for design 3. BW=196N.

Variable	Lower Bound	Upper Bound	Unit
${}^s x_n$	-	-	m
${}^{bw} y_n, {}^{fw} y_n$	0.0	-	m
${}^n y_n, {}^t y_n$	0.0	-	m
${}^s \theta_n$	$-\frac{\pi}{2}$	$\frac{\pi}{2}$	rad
${}^n y_n, {}^t y_n$	0.0	-	m
<hr/>			
${}^{p_1} \theta_n, {}^{l_1} \theta_n, {}^{p_2} \theta_n, {}^{l_2} \theta$	$-\frac{\pi}{2}$	$\frac{\pi}{2}$	rad
${}^b x_n^s, {}^f x_n^s$	0.0	0.4	m
${}^b y_n^s, {}^f y_n^s$	0.0	-	m
${}^b r_{k,n}, {}^f r_{k,n}$	0.0	0.5	m
<hr/>			
${}^b F_{a,n}, {}^f F_{a,n}$	-5.0	5.0	BW
${}^{p_1} \tau_n, {}^{p_2} \tau_n$	0.0	1.0	BW
${}^b F_{x,n}^s, {}^f F_{x,n}$	-20.0	20.0	BW
${}^b F_{y,n}^s, {}^f F_{y,n}$	0.0	20.0	BW
${}^b G_{y,n}, {}^f G_{y,n}$	0.0	20.0	BW
$p_{1,n}, \dots, p_{14,n}$	0.0	-	-
<hr/>			

The Objective Function

The objective function was chosen to minimize the applied forces and torques from the monopods, and ensure the penalty variables were minimized below the acceptable threshold for feasibility.

$$J_F = \sum_{n=1}^N (({}^b F_{a,n})^2 + ({}^f F_{a,n})^2) {}^m h_n \quad (5.105)$$

$$J_\tau = \sum_{n=1}^N (({}^{p_1} \tau_n)^2 + ({}^{p_2} \tau_n)^2) {}^m h_n \quad (5.106)$$

$$J_P = \sum_{n=1}^N p_{1,n} + \dots + p_{14,n} \quad (5.107)$$

$$J = J_F + J_\tau + 1000 J_P \quad (5.108)$$

The penalty scaling factor was again chosen as 1000 to ensure the penalty was sufficiently minimized in the cost function.

Path Constraints

In order to simplify the expression for the path constraints shown in Table 5.6, let:

$${}^m\boldsymbol{q} = [{}^{p_1}\theta, {}^{l_1}\theta, {}^{p_2}\theta, {}^{l_2}\theta] \quad (5.109)$$

The path constraints for the skateboard are largely similar to the path constraints used for design 1 and 2 (Table 5.2 and Table 5.2), however, an extra 5 nodes have been added to allow for the inertia in the monopods' movement. Furthermore, the steady-state constraints have been extended to include a path constraint on the angular velocity of the joints of the monopods. Since a skateboarder is stationary relative to the skateboard upon completing the ollie, this constraint was added.

Table 5.6: The path constraints for design 3.

Phase	Node	Variable Constraints	Unit
Standing	1	${}^{bw}x = 0.0$ ${}^{bw}y = 0.0$ ${}^s\theta = 0.0$	m m rad
		${}^b y^s = 0.0$ ${}^f y^s = 0.0$ ${}^m \mathbf{q} = 0.0$	m m rad
		$\dot{\mathbf{q}} = 0.0$	-
“Pop”	14	${}^t y = 0.0$	m
Apex	33	${}^{bw}y \geq 0.4$ ${}^{fw}y \geq 0.4$	m m
Landing	50	${}^{bw}y = 0.0$ ${}^{fw}y = 0.0$ ${}^b y^s = 0.0$ ${}^f y^s = 0.0$	m m m m
Steady	60	${}^{bw}y = 0.0$ ${}^{fw}y = 0.0$ ${}^b y^s = 0.0$ ${}^f y^s = 0.0$ ${}^m \mathbf{q} = 0.0$ ${}^m \dot{\mathbf{q}} = 0.0$ ${}^b \dot{r} = 0.0$ ${}^f \dot{r} = 0.0$	m m m m m rad/s m/s m/s

Results and Discussion

The solver converged to a locally optimal solution with the highest penalty violation at 1.16×10^{-8} . The simulated trajectory and chosen key decision variable values from the solution are shown in Figure 5.22.

First, looking at the simulated trajectory, the simulated model was able to replicate the ollie, given the limited fixed path constraints. The penalty violation allocated to the wheel-ground and foot-deck contact was also significantly lower than the threshold feasibility value, thus the penalty constraints were not violated in performing the ollie.

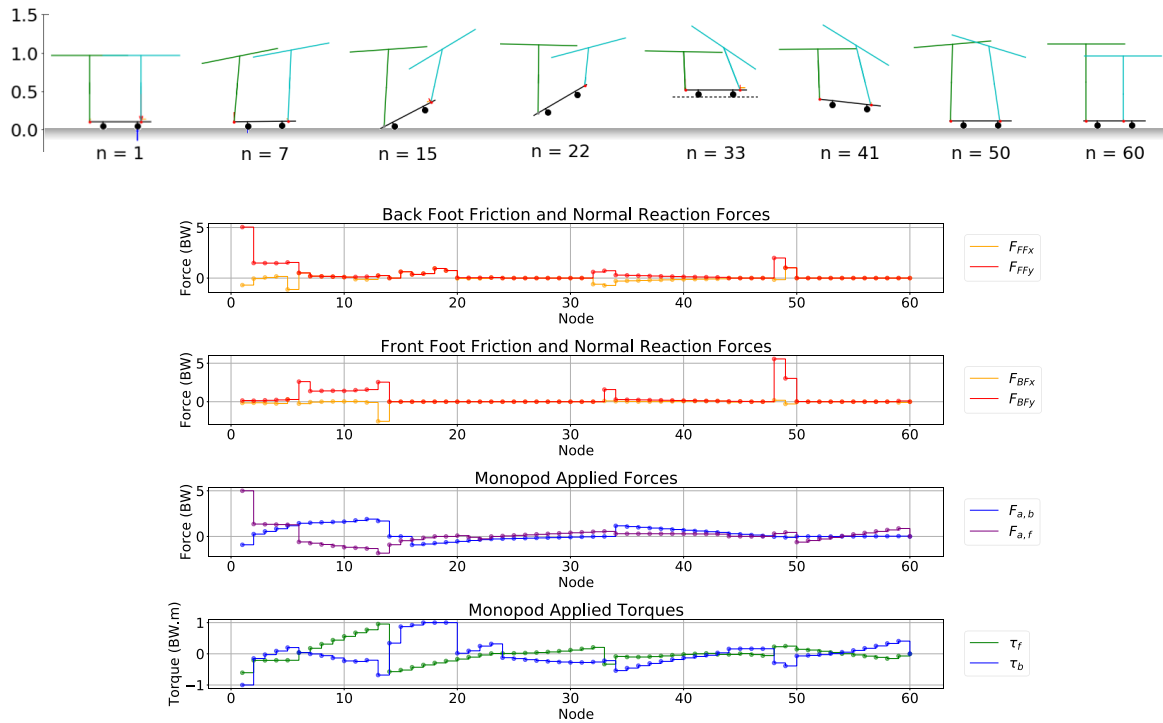


Figure 5.22: The simulated results of design 3 showing snapshots of the system performing the ollie, and the corresponding force and torque profiles.

The simulated model had some further surprising results that were extremely promising for the aim of this study. It can be seen that at $n = 15$, the front-leg-monopod slides its foot up the nose section of the skateboard, effectively pulling the skateboard into the air using the friction force. This is exceedingly similar to the sliding motion that skateboarders use during the “pop” phase of the ollie. Furthermore, both monopods retract their prismatic joints when reaching the apex of the flight phase. This motion is similar to how skateboarders “tuck” their legs close to their body to maximize their board-clearance height. Already, these results suggest that the simplified system may be able to replicate the ollie manoeuvre.

The plots of the force profiles, and applied torques and forces are shown to give an

indication of the forces and torques that the monopods use to perform the simulated manoeuvre. It can be noted that the friction force is only non-zero when there is a normal force, and it is never greater than the maximum static friction. From this, it is clear that both of these contacts have been handled successfully.

Therefore, this test demonstrated that:

1. The foot-deck reaction force - both friction and the force normal to the deck of the skateboard - can be implemented using the contact-implicit method, and has been successfully implemented using two monopods to model the skateboarder.
2. The skateboarder model is able interact with and leave the surface of the skateboard in performing the ollie. The model is also able to exert forces on the skateboard at positions along the length of the skateboard.

This test has been successful in all of the aims it was trying to achieve. However, the limitations to the monopod model were as follows:

1. The monopods used to model the skateboarder's legs were independent and not scaled up to the full mass of a skateboarder. Also, the model only considered the skateboarder's legs. Therefore, the model should be developed to include dependent legs and an upper body, and it should be scaled to full mass.
2. The simulated model is only performing a SO from and onto the ground. The trajectory optimization problem should be developed to simulate movement of the skateboard-skateboarder system, and to model a step-up and step-down ground functions.

5.8 Final Design: Biped with Torso on Skateboard

Through the iterative design process, all of the defined aspects of the ollie manoeuvre have been successfully implemented in the bouncing ball examples, and in designs 1, 2 and 3. A skateboard and skateboarder model has been developed from the simplest model, and now, the final design aims to propose a model which is able to capture all of the key dynamics of the skateboard-skateboarder system. The aim of the final design is, therefore, to:

1. Design a skateboarder model which is able to encapsulate the key dynamics of a skateboarder, including an upper body, and dependent links.
2. Formulate a trajectory optimization problem using the skateboard-skateboarder model which will generate the SO, RO, OD and OU manoeuvres.

5.8.1 Modeling the System

The results from design 1, 2 and 3 suggest that the skateboard model, shown in Figure 5.17, has the required complexity to model the key dynamics of the skateboard, thus, it will again be used as the model for the skateboard.

The skateboarder model should, however, be developed to include an upper body. Furthermore, the upper body, pelvis and legs should be dependent bodies. The chosen model design is shown in Figure 5.23. The chosen biped model was constructed as a four-link kinematic chain with a torso link, pelvis link, and two prismatic joints connected to the pelvis link to represent the legs of the skateboarder. The generalized coordinates used to model the system dynamics were chosen as:

$$\mathbf{q} = [{}^s x, {}^s y, {}^s \theta, {}^p x, {}^p y, {}^p \theta, {}^t \theta, {}^b \theta, {}^b r_k, {}^f \theta, {}^f r_k]^T \quad (5.110)$$

Similarly to the monopod model, the front and back feet of the biped are defined as $({}^b x, {}^b y)$ and $({}^f x, {}^f y)$ respectively.

The prismatic joint was chosen to replicated the human leg in terms of the contraction of the leg when a human crouches down, and extension when a human stands upright, and the propulsion force created by the muscles in the upper and lower legs such as the quadriceps and calf muscles. The links are actuated at the knee of the prismatic joint by forces ${}^b F_a$ and ${}^f F_a$, and the prismatic joints can extend to lengths ${}^b r_k$ and ${}^f r_k$. A

5.8. FINAL DESIGN: BIPED WITH TORSO ON SKATEBOARD

hard-stop reaction force, bF_r and fF_r , was added to each prismatic joint to enforce the limits of the extension of the joints.

The leg-pelvis connection was chosen to replicate the human “hip”. It is actuated by torques ${}^b\tau$ and ${}^f\tau$ which are able to rotate the leg link about the hip joint.

The pelvis-torso connection was chosen to replicate the connection between the upper and lower bodies of the human, which is actuated by the lower back muscles and abdominal muscles. To model this, the torso and pelvis links were modeled as rigid-bodies with actuation ${}^p\tau$ at the pelvis-torso connection which enabled the torso to rotate about the pelvis link.

The torso link adds an extra degree of complexity to the problem. It can be seen that ensuring the torso link is upright at the end of the simulation (the skateboarder is upright) is similar to the commonly known “inverted pendulum” problem. This extra degree of complexity is necessary to model the balance of a skateboarder.

The physical properties of the biped model were based on the study by Plagenhoef et al. [19] regarding the mean mass and lengths of the human male body, in conjunction with the average mass of the skateboarders that participated in the biomechanical studies of the ollie. The dimensions of the biped model are shown in Figure 5.24 and the chosen variable values are shown in Table 5.7.

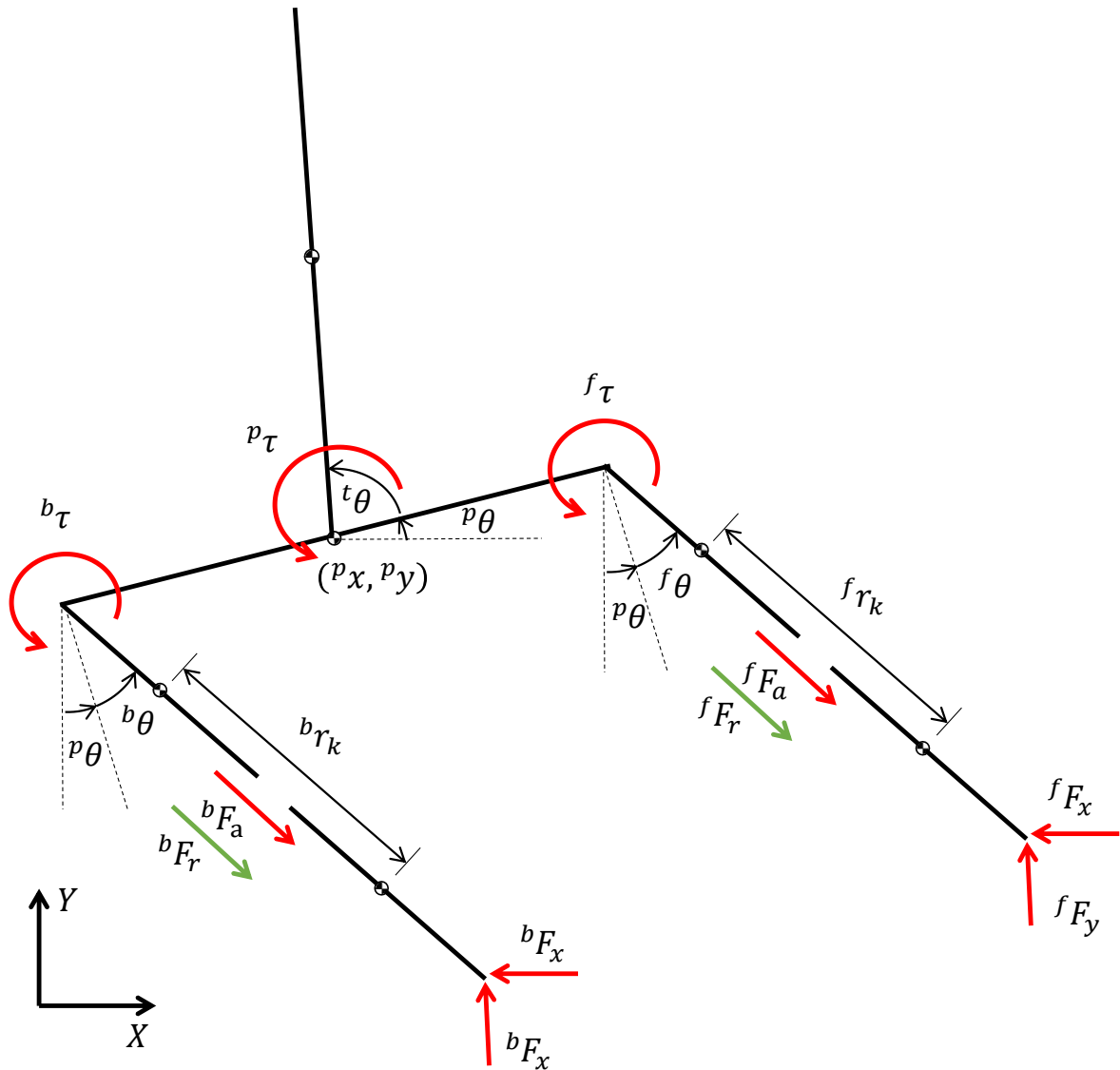


Figure 5.23: The coordinates and actuators of the final design - a biped model with a torso, pelvis and two legs.

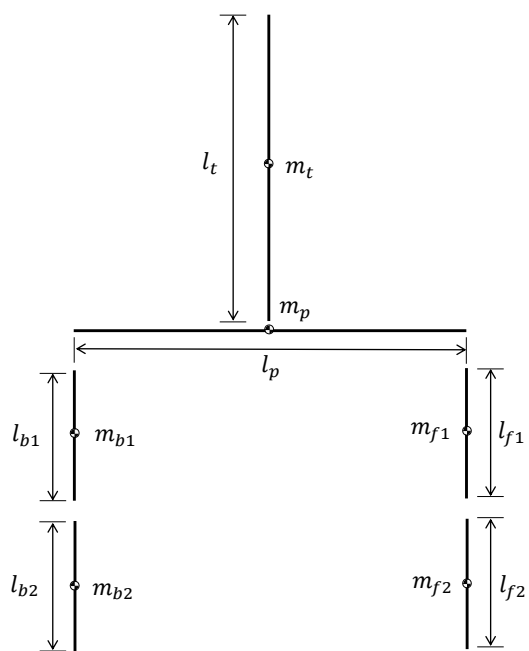


Figure 5.24: The dimensions and mass conventions of the final design.

Table 5.7: The chosen variable values of the biped model, based on the study by Plagenhoef et al. [19].

Variable	Value	Unit
m_t	36.5	kg
m_p	7.3	kg
m_{b1}	7.3	kg
m_{b2}	7.3	kg
m_{f1}	7.3	kg
m_{f2}	7.3	kg
l_t	0.8	m
l_p	0.4	m
l_{b1}	0.45	m
l_{b2}	0.45	m
l_{f1}	0.45	m
l_{f2}	0.45	m

It was decided, due to the physical properties and dynamics of this design, that this model was sufficiently complex to model the skateboarder for the purposes of this study.

5.8.2 The Trajectory Optimization Problems

The trajectory optimization problem was formulated for the four manoeuvres: the SO, RO, OD and OU manoeuvres. Due to the nature of these manoeuvres, there were underlying consistencies in the formulated trajectory optimization problem for each manoeuvre. For each manoeuvre, the problem was formulated using $N = 65$ nodes with $h_m = 0.01s$. The dynamics of the system were integrated using the semi-Euler method described previously.

The Ground Function

Similarly to the bouncing ball ground-step example explained previously, the ground function can be implemented using the complementary relationships between the x-position of the wheels and the ground function. Both step-up and step-down ground functions, as shown in Figure 5.25 will be developed now for the skateboard system.

The position of the wheels, ^{bw}x and ^{fw}x , can be resolved into positive and negative components relative to the position of the step, X_s :

$$^{bw}x - X_s = ^{bw}x^{G+} - ^{bw}x^{G-} \quad (5.111)$$

$$^{fw}x - X_s = ^{fw}x^{G+} - ^{fw}x^{G-} \quad (5.112)$$

$$^{bw}x^{G+}, ^{bw}x^{G-}, ^{fw}x^{G+}, ^{fw}x^{G-} \geq 0 \quad (5.113)$$

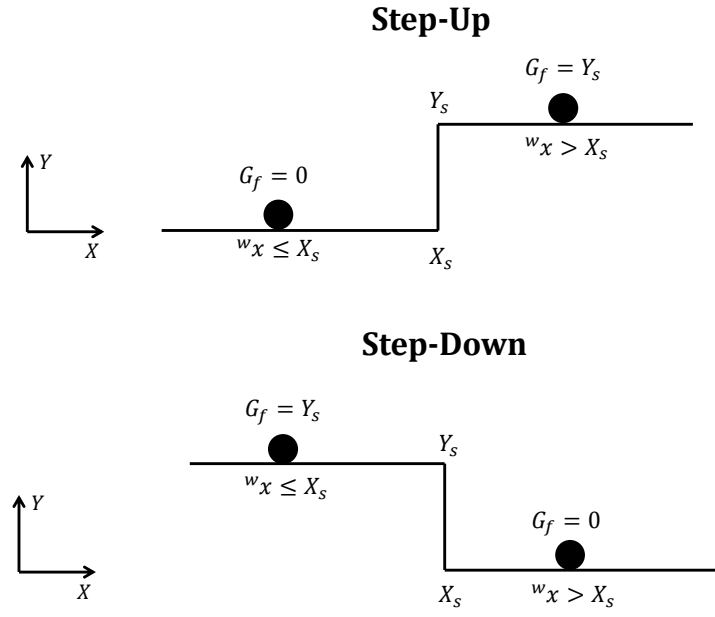


Figure 5.25: A simple illustration of the formulation of the step-up and step-down ground functions.

The ground function for the front and back wheels, ${}^{bw}G_F$ and ${}^{fw}G_F$, should be bound as follows:

$$0 \leq {}^{bw}G_F \leq Y_s \quad (5.114)$$

$$0 \leq {}^{fw}G_F \leq Y_s \quad (5.115)$$

Now, the step-up and step-down ground functions can be defined using complementarity:

Step-up:

$${}^{bw}G_{F,n} {}^{bw}x_n^{G-} = p_{1,n} \quad (5.116)$$

$$(Y_s - {}^{bw}G_{F,n}) {}^{bw}x_n^{G+} = p_{2,n} \quad (5.117)$$

$${}^{fw}G_{F,n} {}^{fw}x_n^{G-} = p_{3,n} \quad (5.118)$$

$$(Y_s - {}^{fw}G_{F,n}) {}^{fw}x_n^{G+} = p_{4,n} \quad (5.119)$$

Step-down:

$$(Y_s - {}^{bw}G_{F,n}) {}^{bw}x_n^{G-} = p_{1,n} \quad (5.120)$$

$${}^{bw}G_{F,n} {}^{bw}x_n^{G+} = p_{2,n} \quad (5.121)$$

$$(Y_s - {}^{fw}G_{F,n}) {}^{fw}x_n^{G-} = p_{3,n} \quad (5.122)$$

$${}^{fw}G_{F,n} {}^{fw}x_n^{G+} = p_{4,n} \quad (5.123)$$

Contacts

The contacts involved in the skateboard-skateboarder system are the tail-ground contact, wheel-ground contact, foot-deck contact and the prismatic joint hard-stop contact. The tail-ground contact was scheduled to occur at $n = 20$ with ${}^t y_{20} = 0$. The state mapping was given using $e = -0.6$ as:

$${}^s\dot{y}_{20} = e {}^t v_{y,19} + {}^s\dot{y}_{19} + {}^m h_{20} {}^s\ddot{y}_{19} \quad (5.124)$$

The complete set of constraints defining contacts in the system, which has been developed extensively previously, were defined as follows:

The wheel-ground contact (with ground function):

$${}^{bw}y_{n+1}^G {}^bG_{y,n} = p_{5,n} \quad (5.125)$$

$${}^{fw}y_{n+1}^G {}^fG_{y,n} = p_{6,n} \quad (5.126)$$

The foot-deck contact:

$$(\mu {}^b F_{y,n}^{s+} - {}^b F_{x,n}^{s+} - {}^b F_{x,n}^{s-})({}^b \dot{x}_n^{s+} + {}^b \dot{x}_n^{s-}) = p_{7,n} \quad (5.127)$$

$$(\mu {}^f F_{y,n}^{s+} - {}^f F_{x,n}^{s+} - {}^f F_{x,n}^{s-})({}^f \dot{x}_n^{s+} + {}^f \dot{x}_n^{s-}) = p_{8,n} \quad (5.128)$$

$$({}^b \dot{x}_n^{s+})({}^b F_{x,n}^{s+}) = p_{9,n} \quad (5.129)$$

$$({}^b \dot{x}_n^{s-})({}^b F_{x,n}^{s-}) = p_{10,n} \quad (5.130)$$

$$({}^f \dot{x}_n^{s+})({}^f F_{x,n}^{s+}) = p_{11,n} \quad (5.131)$$

$$({}^f \dot{x}_n^{s-})({}^f F_{x,n}^{s-}) = p_{12,n} \quad (5.132)$$

$$({}^b y_{n+1}^s)({}^b F_{y,n}^{s+}) = p_{13,n} \quad (5.133)$$

$$({}^f y_{n+1}^s)({}^f F_{y,n}^{s+}) = p_{14,n} \quad (5.134)$$

The prismatic joint hard-stop contact:

$$({}^b r_{k(upp)} - {}^b r_{k,n+1})({}^b F_{r,n}^-) = p_{15,n} \quad (5.135)$$

$$({}^b r_{k,n+1} - {}^b r_{k(low)})({}^b F_{r,n}^+) = p_{16,n} \quad (5.136)$$

$$({}^f r_{k(upp)} - {}^f r_{k,n+1})({}^f F_{r,n}^-) = p_{17,n} \quad (5.137)$$

$$({}^f r_{k,n+1} - {}^f r_{k(low)})({}^f F_{r,n}^+) = p_{18,n} \quad (5.138)$$

Variable Bounds

The complete set of variable bounds used for the various ollie manoeuvres is shown in Table 5.8. The variable bounds are necessary to implement the contact constraints and ensure the trajectory is realistically feasible.

Table 5.8: The variable bounds for the final design. BW=716N.

Variable	Lower Bound	Upper Bound	Unit
${}^s x_n$	-	-	m
${}^{bw} y_n^G, {}^{fw} y_n^G$	0.0	-	m
${}^n y_n^G, {}^t y_n^G$	0.0	-	m
${}^s \theta_n$	$-\frac{\pi}{2}$	$\frac{\pi}{2}$	rad
${}^t \theta_n$	$\frac{\pi}{4}$	$\frac{3\pi}{4}$	rad
${}^p \theta_n, {}^b \theta_n, {}^f \theta$	$-\frac{\pi}{2}$	$\frac{\pi}{2}$	rad
${}^b x_n^s$	0.0	0.4	m
${}^f x_n^s$	-0.4	0.0	m
${}^b y_n^s, {}^f y_n^s$	0.0	-	m
${}^b r_{k,n}, {}^f r_{k,n}$	0.0	0.45	m
${}^b F_{a,n}, {}^f F_{a,n}$	-3.0	3.0	BW
${}^p \tau_n, {}^b \tau_n, {}^f \tau_n$	0.0	1.0	BW.m
${}^b F_{x,n}^s, {}^f F_{x,n}^s$	-20.0	20.0	BW
${}^b F_{y,n}^s, {}^f F_{y,n}^s$	0.0	20.0	BW
${}^b G_{y,n}, {}^f G_{y,n}$	0.0	20.0	BW
$p_{1,n}, \dots, p_{18,n}$	0.0	-	-

The Objective Function

The objective function chosen minimized the force and torque squared, as well as the penalty variables. It has been shown in the previous designs that, using this objective

function, the simulation is able to generate the ollie. Thus, a similar objective function to design 3 was chosen:

$$J_F = \sum_{n=1}^N (({}^b F_{a,n})^2 + ({}^f F_{a,n})^2) {}^m h_n \quad (5.139)$$

$$J_\tau = \sum_{n=1}^N (({}^b \tau_n)^2 + ({}^f \tau_n)^2 + ({}^p \tau_n)^2) {}^m h_n \quad (5.140)$$

$$J_P = \sum_{n=1}^N p_{1,n} + \dots + p_{18,n} \quad (5.141)$$

$$J = J_F + J_\tau + 1000J_P \quad (5.142)$$

The penalty scaling factor was again chosen as 1000 to ensure the feasibility penalty was sufficiently minimized in the cost function.

The SO Manoeuvre

Since the SO is performed from the ground, onto the ground, the height of the ground function was set to zero such that $Y_s = 0\text{m}$.

In order to simplify the path constraints shown in Table 5.9, the following definitions were made:

$${}^{m_1} \mathbf{q} = [{}^p \theta, {}^b \theta, {}^f \theta] \quad (5.143)$$

$${}^{m_2} \mathbf{q} = [{}^t \theta, {}^p \theta, {}^b \theta, {}^b r_k, {}^f \theta, {}^f r_k] \quad (5.144)$$

Since the skateboard was modeled as a rigid body, it would not bend or break when the biped lands on it. Therefore, in order to ensure the biped lands above the wheel bearings of the skateboard, this was enforced as a path constraint.

The RO Manoeuvre

Similarly to the SO, the ground function was set to zero, $Y_s = 0\text{m}$. The following variable was defined to represent the set of generalized coordinates, excluding ${}^p x$ and ${}^s x$.

$${}^{m_3} \mathbf{q} = [{}^s y, {}^s \theta, {}^p y, {}^p \theta, {}^t \theta, {}^b \theta, {}^b r_k, {}^f \theta, {}^f r_k] \quad (5.145)$$

Importantly for the RO manoeuvre, the initial x-velocity of the skateboard and the biped pelvis were not fixed to zero. This allowed the model to reach the final path constraint that ${}^{bw}x \geq 2.0m$.

The OD Manoeuvre

This manoeuvre involves moving the skateboard from a raised level to the ground level. This is captured by the step-down ground function. The position of the step was chosen as $X_s = 1.2m$. In order to replicate the study by Leuchanka et al. [32] where the step was $0.36m$ high, and the study by Frederick et al. [2] where the step was $0.457m$ high, the step heights were chosen as $Y_s = 0.36m$ and $Y_s = 0.45m$ respectively.

Upon further investigation into the OD manoeuvre, it was found that skateboarders often did not “pop” the skateboard when performing the manoeuvre, but rather, they shift their weight onto the back of the skateboard and ride off the edge of the step. Thus, the “pop” path constraint was removed.

The OU Manoeuvre

The OU manoeuvre entail jumping off the ground up onto a step. This involves the step-up ground function. Again, it was chosen that $X_s = 1.2m$, $Y_s = 0.36m$ and $Y_s = 0.45m$ to replicate the previous studies.

Table 5.9: The path constraints for the SO manoeuvre.

Phase	Node	Variable Constraints	Unit
Standing	1	${}^{bw}x = 0.0$ ${}^{bw}y^G = 0.0$ ${}^{fw}y^G = 0.0$	m m m
		${}^b y^s = 0.0$ ${}^f y^s = 0.0$ ${}^t \theta = \frac{\pi}{2}$ ${}^{m_1} \mathbf{q} = 0.0$	m m rad rad
		$\dot{\mathbf{q}} = 0.0$	-
“Pop”	19	${}^t y = 0.0$	m
Apex	38	${}^{bw}y \geq 0.5$ ${}^{fw}y \geq 0.5$	m m
Biped Landing	60	${}^{bw}y^G = 0.0$ ${}^{fw}y^G = 0.0$ ${}^b x^s = -0.225$ ${}^f x^s = 0.225$ ${}^b y^s = 0.0$ ${}^f y^s = 0.0$	m m m m m m
Steady	65	${}^{bw}y^G = 0.0$ ${}^{fw}y^G = 0.0$ ${}^b x^s = -0.225$ ${}^f x^s = 0.225$ ${}^b y^s = 0.0$ ${}^f y^s = 0.0$ ${}^{m_1} \mathbf{q} = 0.0$ ${}^{m_2} \dot{\mathbf{q}} = 0.0$	m m m m m m rad rad/s

Table 5.10: The path constraints for the RO manoeuvre.

Phase	Node	Variable Constraints	Unit
Standing	1	${}^{bw}x = 0.0$ ${}^{bw}y^G = 0.0$ ${}^{fw}y^G = 0.0$	m
		${}^b y^s = 0.0$ ${}^f y^s = 0.0$ ${}^t \theta = \frac{\pi}{2}$ ${}^{m_1} \dot{q} = 0.0$	m m rad rad
		${}^{m_3} \ddot{q} = 0.0$	-
“Pop”	19	${}^t y = 0.0$	m
Apex	38	${}^{bw}y \geq 0.5$ ${}^{fw}y \geq 0.5$	m m
Biped Landing	60	${}^{bw}y^G = 0.0$ ${}^{fw}y^G = 0.0$ ${}^b x^s = -0.225$ ${}^f x^s = 0.225$ ${}^b y^s = 0.0$ ${}^f y^s = 0.0$	m m m m m m
Steady	65	${}^{bw}y^G = 0.0$ ${}^{fw}y^G = 0.0$ ${}^b x^s = -0.225$ ${}^f x^s = 0.225$ ${}^b y^s = 0.0$ ${}^f y^s = 0.0$ ${}^{m_1} q = 0.0$ ${}^{m_2} \dot{q} = 0.0$	m m m m m m rad rad/s
		${}^{bw}x \geq 2.0$	m

Table 5.11: The path constraints for the OD manoeuvre.

Phase	Node	Variable Constraints	Unit
Standing	1	${}^{bw}x = 0.0$ ${}^{bw}y^G = 0.0$ ${}^{fw}y^G = 0.0$	m m m
		${}^b y^s = 0.0$ ${}^f y^s = 0.0$ ${}^t \theta = \frac{\pi}{2}$ ${}^{m_1} \mathbf{q} = 0.0$	m m rad rad
		${}^{m_3} \dot{\mathbf{q}} = 0.0$ ${}^s \dot{x} \leq 5.0$ ${}^p \dot{x} \leq 5.0$	- m/s m/s
Apex	38	${}^{bw}y \geq 0.5$ ${}^{fw}y \geq 0.5$	m m
Biped Landing	60	${}^{bw}y^G = 0.0$ ${}^{fw}y^G = 0.0$ ${}^b x^s = -0.225$ ${}^f x^s = 0.225$ ${}^b y^s = 0.0$ ${}^f y^s = 0.0$	m m m m m m
Steady	65	${}^{bw}y^G = 0.0$ ${}^{fw}y^G = 0.0$ ${}^b x^s = -0.225$ ${}^f x^s = 0.225$ ${}^b y^s = 0.0$ ${}^f y^s = 0.0$ ${}^{m_1} \mathbf{q} = 0.0$ ${}^{m_2} \dot{\mathbf{q}} = 0.0$ ${}^{bw}x \geq 2.0$	m m m m m m rad rad/s m

Table 5.12: The path constraints for the OU manoeuvre.

Phase	Node	Variable Constraints	Unit
Standing	1	${}^{bw}x = 0.0$ ${}^{bw}y^G = 0.0$ ${}^{fw}y^G = 0.0$	m m m
		${}^b y^s = 0.0$ ${}^f y^s = 0.0$ ${}^t \theta = \frac{\pi}{2}$ ${}^{m_1} \dot{q} = 0.0$	m m rad rad
		${}^{m_3} \dot{q} = 0.0$ ${}^s \dot{x} \leq 5.0$ ${}^p \dot{x} \leq 5.0$	- m/s m/s
“Pop”	19	${}^t y = 0.0$	m
Apex	38	${}^{bw}y \geq 0.5$ ${}^{fw}y \geq 0.5$	m m
Biped Landing	60	${}^{bw}y^G = 0.0$ ${}^{fw}y^G = 0.0$ ${}^b x^s = -0.225$ ${}^f x^s = 0.225$ ${}^b y^s = 0.0$ ${}^f y^s = 0.0$	m m m m m m
Steady	65	${}^{bw}y^G = 0.0$ ${}^{fw}y^G = 0.0$ ${}^b x^s = -0.225$ ${}^f x^s = 0.225$ ${}^b y^s = 0.0$ ${}^f y^s = 0.0$ ${}^{m_1} \dot{q} = 0.0$ ${}^{m_2} \ddot{q} = 0.0$	m m m m m m rad rad/s
		${}^{bw}x \geq 2.0$	m

Chapter 6

Results

This chapter presents the results from the formulated trajectory optimization problems of the SO, RO, OD and OU manoeuvres. For the sake of simplicity, the solved trajectory of the formulated optimization problems will be referred to as the simulated trajectories. Each of the simulated trajectories of the various ollie manoeuvres will be presented separately. In the following chapter, the results will be critically analysed.

It should be noted that, within the time constraints of this project, a feasible OU manoeuvre was not able to be generated. The possible reasons for this will be a point of discussion in this chapter. Also, it is important to note that, for all results, the body weight of the biped was $BW = 716.13N$ (73kg).

Visual representations of the simulated trajectories have been presented below, however, if one would like a more complete representation of the simulated trajectories, links to videos posted on YouTube have been attached in Appendix B.

6.1 The SO Simulation Results

The SO trajectory optimization problem converged to a locally optimal solution with a maximum penalty violation of 3.2×10^{-6} . The simulated trajectory of the SO is shown in Figure 6.1 and the force profile is shown in Figure 6.2. The maximum GRF at take-off for the SO is 5.79 BW and at landing is 3.14 BW. The length of the simulated manoeuvre is $t = 0.64s$.

6.2 The RO Simulation Results

The RO trajectory optimization problem converged to a locally optimal solution with a maximum penalty violation of 3.24×10^{-6} . The simulated trajectory of the RO is shown in Figure 6.3 and the force profile is shown in Figure 6.4. At $t = 0$, the skateboard and biped both have initial x-velocities of $3.2m.s^{-1}$ at a the position ${}^{bw}x = 0m$, and the simulation ends with the skateboard in position ${}^{bw}x = 2.0m$. The peak GRF at take-off for the RO is 3.78 BW and at landing is 8.01 BW. The length of the simulated manoeuvre is $t = 0.63s$.

6.3 The OD Simulation Results

Lastly, the 0.36m and 0.45m OD trajectory optimization problems converged to locally optimal solutions with a maximum penalty violation of 3.24×10^{-6} . The simulated trajectory of the 0.36m OD is shown in Figure 6.5 and the force profile the 0.36m OD is shown in Figure 6.6. The peak GRFs for the 0.36m OD at take-off and landing were 2.58 BW and 4.21 BW respectively, and for the 0.45m OD were 2.90 BW and 3.57 BW respectively. The length of the simulated manoeuvres were $t = 0.58s$ and $t = 0.61s$ respectively.

6.4 Summary of Peak Ground Reaction Forces

A summary of the simulated peak GRFs obtained for the 0.5m SO, 0.5m RO, 0.36m OD and 0.45m OD are shown in Table 6.1 below.

Table 6.1: A summary of the recorded GRFs from the simulated SO, RO and OD manoeuvres, expressed in terms of BW.

	Take-off	Landing
SO	5.79	3.14
RO	3.78	8.01
0.36m OD	2.58	4.21
0.45m OD	2.90	3.57

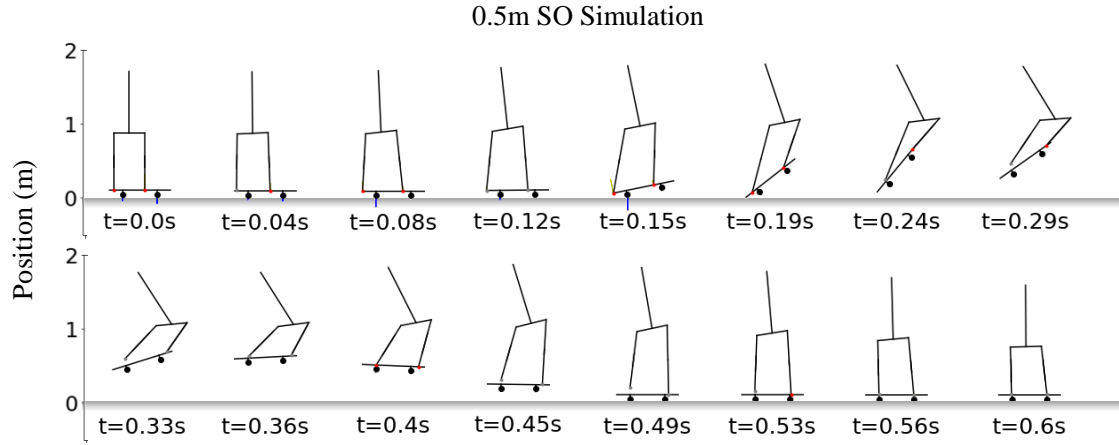


Figure 6.1: The simulated trajectory of the modelled skateboard-skateboarder system performing a 0.5m SO manoeuvre given in four node intervals.

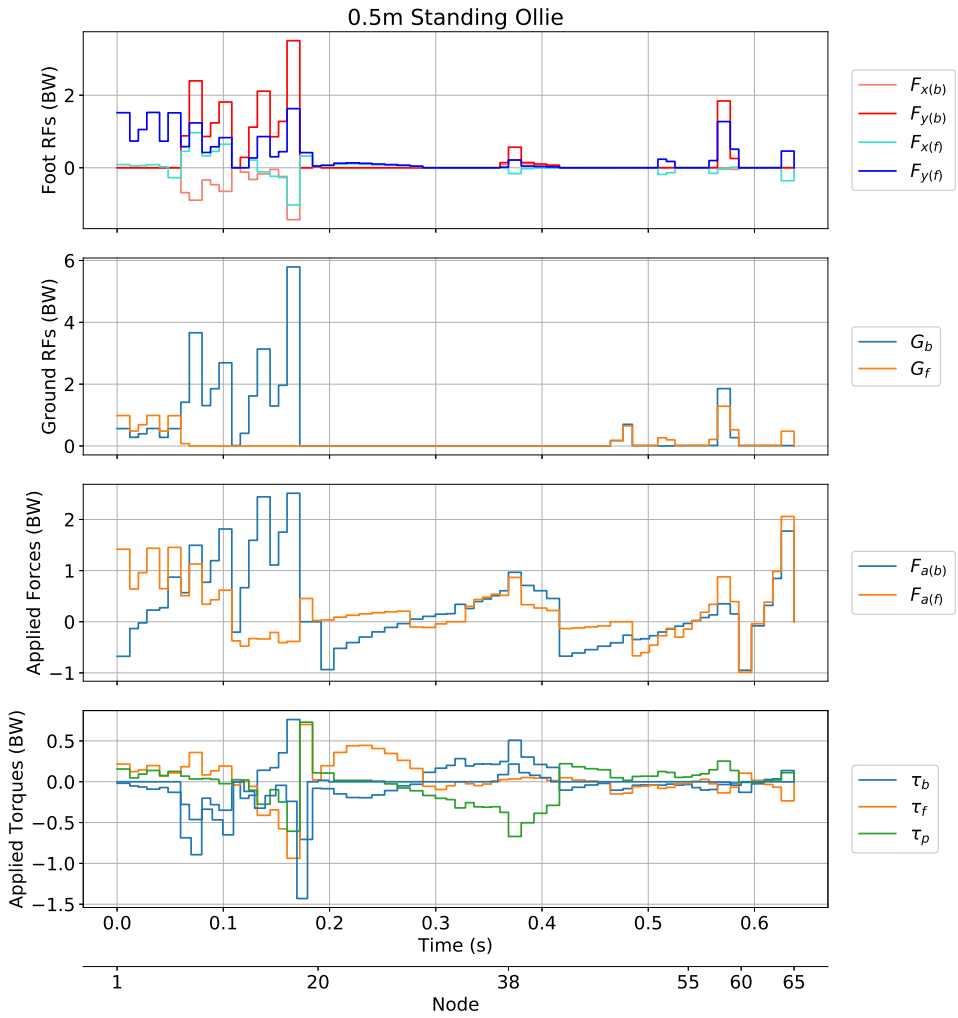


Figure 6.2: The simulated force profile of the SO manoeuvre showing the foot-deck and wheel-ground reaction forces, the applied force at the prismatic joint and the applied torques.

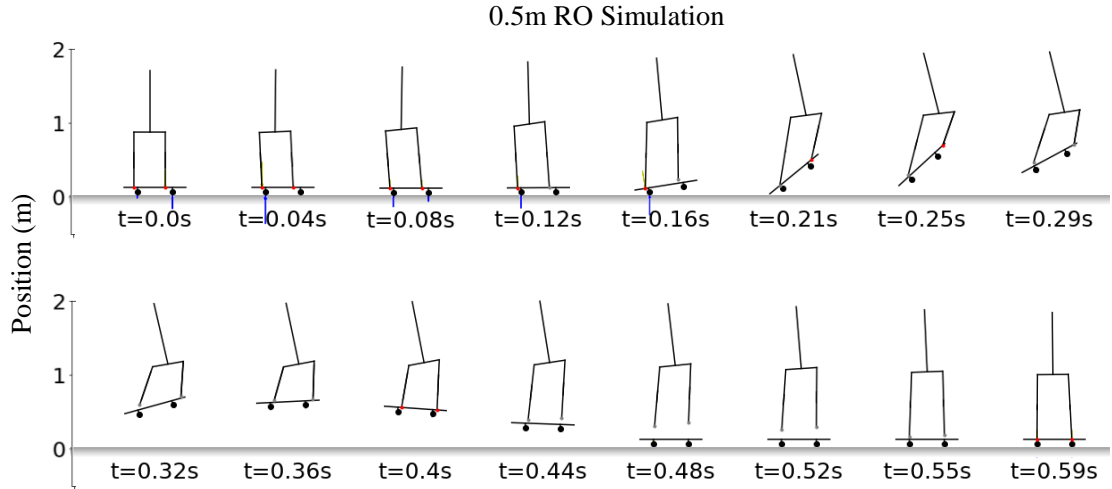


Figure 6.3: The simulated force profile of the RO manoeuvre showing the foot-deck and wheel-ground reaction forces, the applied forces at the prismatic joint and the applied torques.

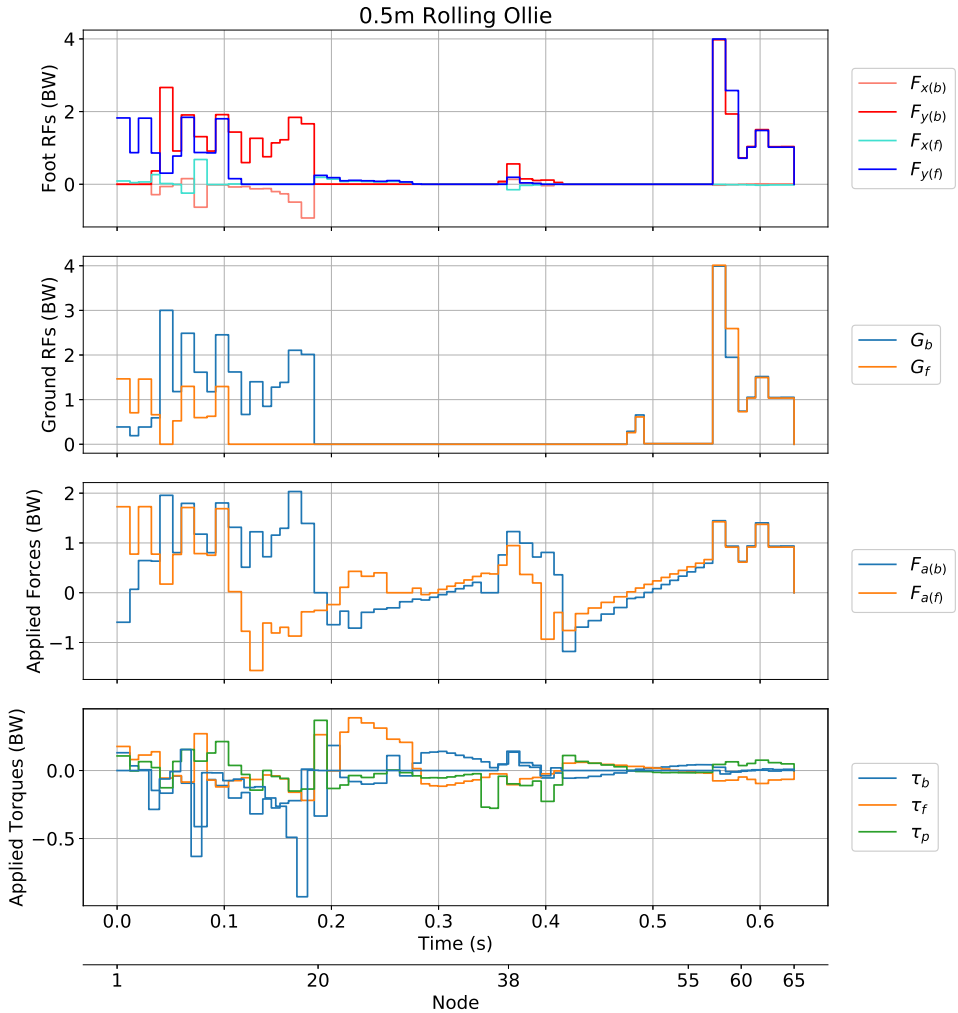


Figure 6.4: The simulated force profile of the RO manoeuvre showing the foot-deck and wheel-ground reaction forces, the applied forces at the prismatic joint and the applied torques.

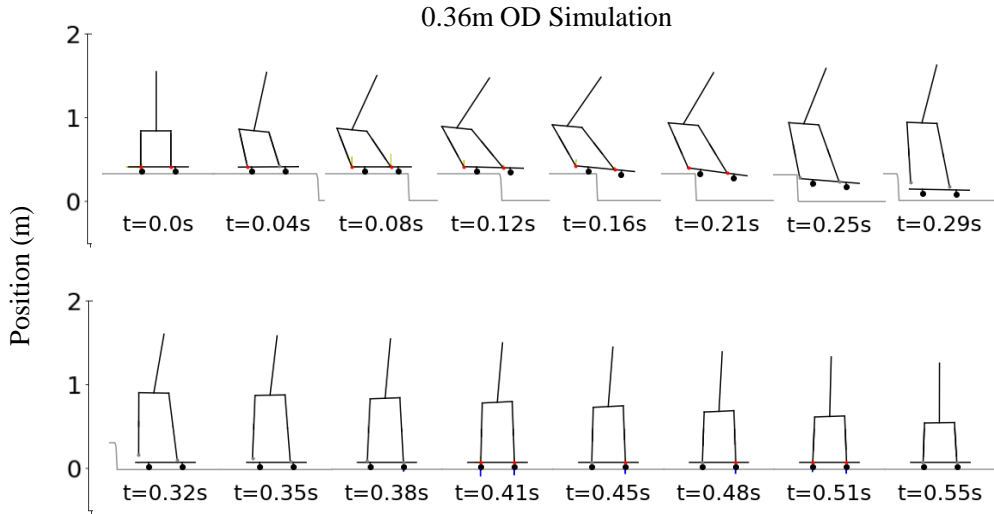


Figure 6.5: The simulated trajectory of the modelled skateboard-skateboarder system performing an OD manoeuvre from a $0.36m$ step, given in four node intervals.

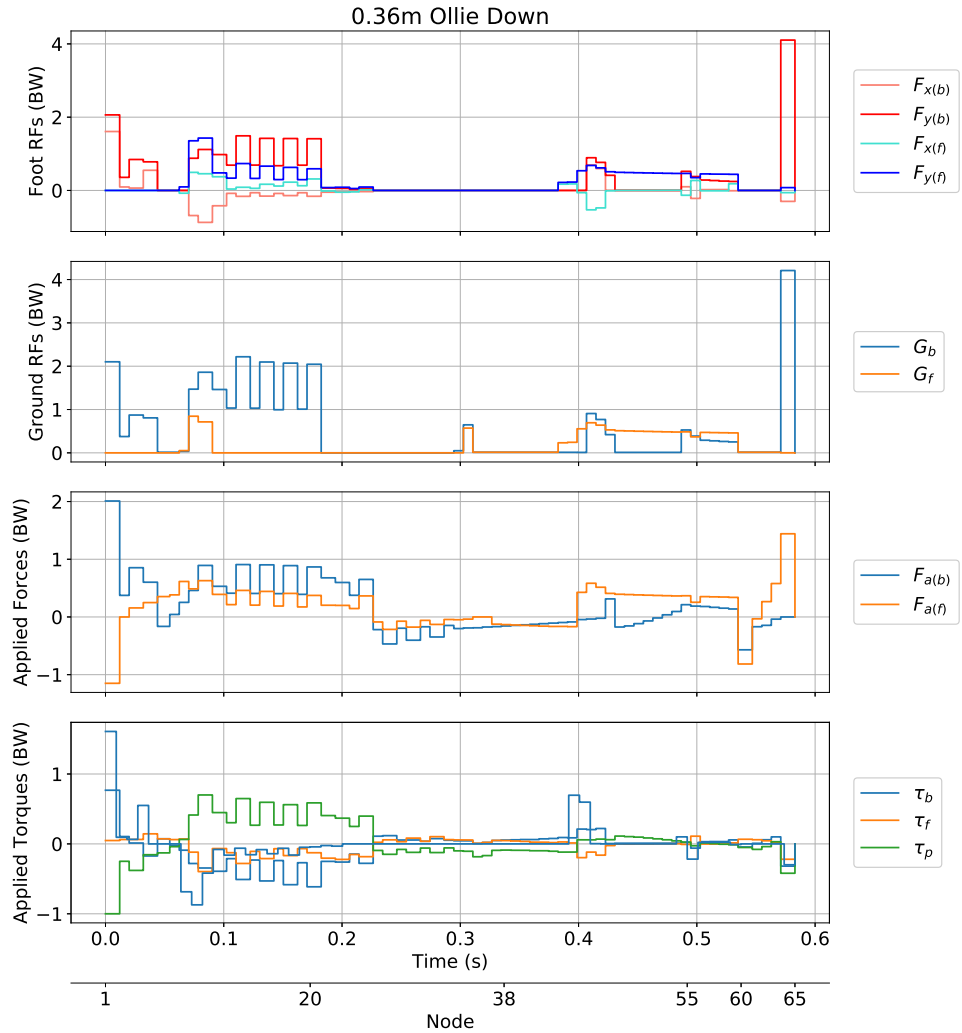


Figure 6.6: The simulated force profile of the $0.36m$ OD manoeuvre showing the foot-deck and wheel-ground reaction forces, the applied forces at the prismatic joint and the applied torques.

Chapter 7

Discussion

This chapter will provide a critical analysis of the results presented in the previous chapter. The discussion will be partitioned into three sections: 1) an analysis of the modeling of the contacts in the system, 2) a comparison of the simulated trajectory of the skateboarder-skateboard system performing the SO and RO manoeuvre against the real-life trajectories, and 3) a comparison of the simulated GRF profiles and peak GRF data to that obtained from literature. Further insight into the means by which the system performs the manoeuvre will also be discussed.

7.1 The Simulated Trajectories

Using the simulated results from of the SO and RO manoeuvres presented in the previous chapter, the manoeuvres can be compared to the real-life trajectories given in Figures 4.2 and 4.3. This comparison is a visual, high-level comparison to gauge the extent to which the observed motion of the ollie has been replicated.

An important aspect of the simulated trajectories presented in the previous chapter that should not be understated is that the motion of all of the simulated results appear to adhere to the laws of physics. Furthermore, visually, the contacts seem to behave as desired. This statement is further validated by the maximum penalty violation of the optimized systems which is 3.2×10^{-6} . This is sufficiently below the chosen violation threshold of 1×10^{-5} , and thus, it can be assumed that the various system contacts have been implemented successfully.

7.1.1 The SO simulated Trajectory

The simulated trajectory of the SO, shown in Figure 6.1, will first be evaluated by comparing it to the defined phases of the ollie, and then, the trajectory will be compared to the snapshots of the real-life skateboarder performing an ollie.

Drawing on the force profiles for the SO given in Figure 6.2, the motion of the SO simulated trajectory, shown in Figure 6.1, can be partitioned into the identified essential aspects and phases of the ollie described in the “Understanding the Ollie” section in chapter 2:

- A. **Crouching:** *The skateboarder places his back foot on the tail of the skateboard and his front foot roughly midway down the skateboard, ensuring his stance is still balanced. His knees are bent to prepare to rapidly jump upwards.*

Simulated: ($t = 0.0s$) The biped is in a crouched position, with its back foot on the tail region of the skateboard and its front foot just over half-way up the skateboard.

- B. **Pre-“pop”** *The skateboarder accelerates himself upwards by extending his legs and pushing down with his back foot to accelerate the tail of the skateboard downwards. This causes the board to pivot about the back wheel in a counter-clockwise direction.*

Simulated: ($0.0s < t \leq 0.17s$) The biped exerts a force downward on the tail of the skateboard with its back leg, as shown in the force profile given in Figure 6.2, while extending its prismatic leg joints. The skateboard rotates about its back wheel.

- C. **The “pop”:** *The tail of the skateboard is slammed into the ground while the skateboarder lifts his back foot from the skateboard. When the tail strikes the ground, the tail bounces off the ground, propelling the skateboard into the air. Simultaneously, the skateboarder slides his front foot forward along the skateboard, using the friction between the foot and the skateboard to “pull” the board into the air.*

Simulated: ($0.17s \leq t \leq 0.19s$) The skateboard tail makes contact with the ground, and, due to modeling of the collision, the skateboard is propelled into the air. Simultaneously the biped’s back foot leaves the skateboard, and the biped’s front foot slides up the skateboard deck, inducing a friction force that accelerates the skateboard into the air. This friction force is shown in the top plot in Figure 6.2.

- D. **Airborne:** *The skateboarder and skateboard are in the air. The skateboarder continues to slide his front foot forward and uses their back foot to level the skateboard out in the air. The skateboarder can tuck their legs in to achieve maximum skateboard height.*

Simulated: ($0.19s < t \leq 0.46s$) The biped and skateboard models are both in the air. The biped continues to use the friction force on its front foot to pull the skateboard into the air. The biped contracts its leg joints, effectively tucking in its legs, to reach the apex height of 0.5m. The biped uses its front and back feet to apply forces on the skateboard to level the skateboard.

E. Landing: *The skateboarder aims to position his front and back feet on the wheel bearings of the skateboard. The skateboarder bends his knees upon landing to cushion his landing, while using his arms to keep balanced. Both wheels are on the ground.*

Simulated: ($0.46s < t < 0.65$) The skateboard first makes contact with the ground with both wheels simultaneously. Then the biped lands on the skateboard with its front foot first, then its back foot, both located above the wheels of the skateboard. The biped's prismatic leg joints contract during the landing.

F. Post-Landing *The skateboarder has both feet on the bearings of the wheels and has extended his legs to a comfortable height. Both the wheels of the skateboard are on the ground and the skateboarder is standing still. The skateboarder and skateboard could be described as being in steady-state.*

Simulated: ($t = 0.64s$) The biped has both feet on the skateboard over the wheels. The prismatic leg joints are completely contracted. The angular velocities of the joints and the velocity of the prismatic joints are zero.

Comparing the description of the phases from chapter 2 to the description of the simulated trajectory given above, it is evident that each phase is adequately replicated in the simulated trajectory. Furthermore, the time taken to complete the manoeuvre was $t = 0.64s$ which is only $0.04s$ longer than the expected time.

A noticeable difference can be seen in the landing of the skateboard and biped. Skateboarder's usually push down on the skateboard while keeping their feet on the skateboard deck during landing to increase the stability of the landing, as found in the study by [32]. However, the simulation results show the skateboard landing first, then the biped's front and back feet. This may suggest that the stability of the skateboarder has been overlooked or oversimplified in modeling.

Since it has been shown that the simulation of the system replicates the phases of the SO manoeuvre, the observed spacial trajectory of the simulation should be investigated. The comparison between the SO simulated motion, and the snapshots of a skateboarder performing a SO are shown in Figure 7.1. It should be noted that the sequence of the simulated SO trajectory has been adjusted for timing purposes.

Comparing the simulated and real-life SO trajectories frame by frame shows a strong visual resemblance between the two trajectories. However, there are some discrepancies between the two. The initial angle of the skateboard at the "pop" ($t = 0.19s$) is greater in the real-life trajectory than the simulated trajectory. This may be a result of the exclusion of the pop-angle of the skateboard from the skateboard model. Another dis-

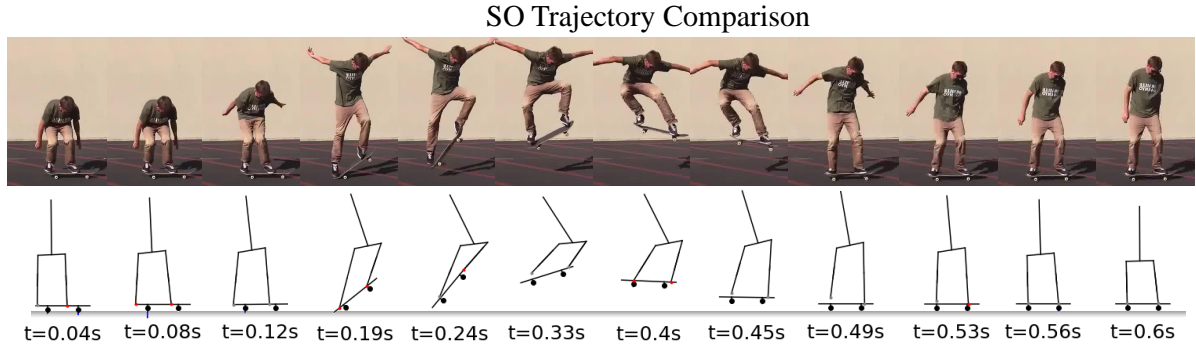


Figure 7.1: A comparison of the SO simulation results to snapshots of a skateboarder performing an SO. On a high level, the simulated results appear to replicate the ollie trajectory.

crepancy is the position of the pelvis, which, in the real-life manoeuvre, is shown to lag behind the skateboard in the x-direction, whereas, in the simulated trajectory, it leads the skateboard. This may too be a result of modeling the skateboarder legs as prismatic joints which cannot bend at the knee, like the human leg.

In summary, it has been shown that the trajectory of the simulated system performing the SO manoeuvre replicates both the defined phases of the SO, and, to a large extent, the visual real-life motion of the manoeuvre, with a few minor discrepancies which have been identified.

7.1.2 The RO simulated Trajectory

The simulated RO trajectory, shown in Figure 6.3, should now be analysed and validated against existing literature. Since it has been demonstrated that the SO manoeuvre replicates the defined phases of the ollie, this analysis will not be conducted for the RO to avoid repetition. Instead, the simulated trajectory of the back and front wheel of the skateboard, and the mid-point between the wheels can be compared to the real-life trajectory provided by Bhatia [16]. The comparison is shown in Figure 7.2.

It is clear from this comparison that the simulated and real-life trajectories of the RO are noticeably similar. All three plotted trajectories bare essentially the same shape as the plots from literature. It should be noted that this data recorded by Bhatia was conducted on a single skateboarder performing a single ollie, and naturally, this does represent the “template” of the expected trajectory for all ollie manoeuvres. Therefore, despite the fact that these trajectories do not align perfectly, their resemblance serves as validation for the developed system.

This is another promising result for the developed skateboard-skateboarder system. To evaluate the extent of the improvement of the motion of the system between this study

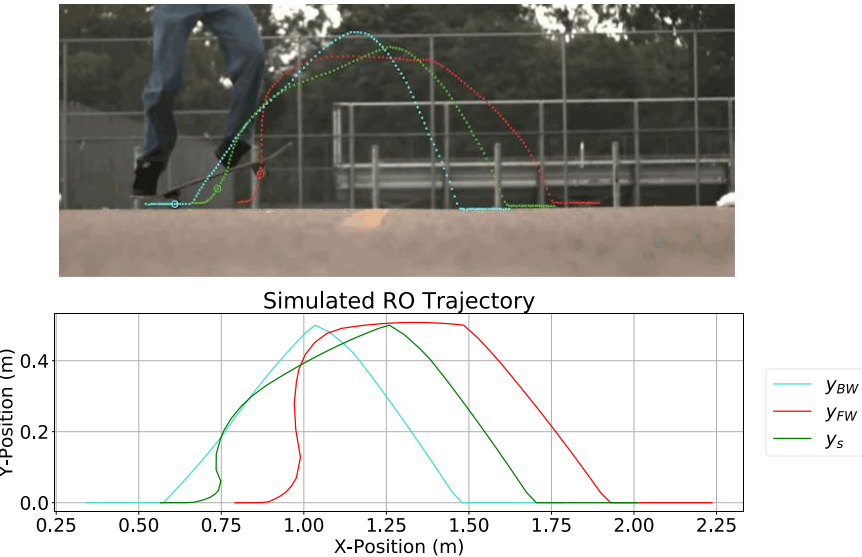


Figure 7.2: A comparison of the observed trajectory provided by Bhatia [16] and the simulated trajectory of the RO manoeuvre.

and the previous study by Kolev [14], the RO simulated results obtained by Kolev are shown in Figure 7.3. Since the biped model in this study is able to leave the skateboard, move its feet along the skateboard, and induce a friction force, the system used in this study exhibits a trajectory which replicates the ollie manoeuvre to a further extent.

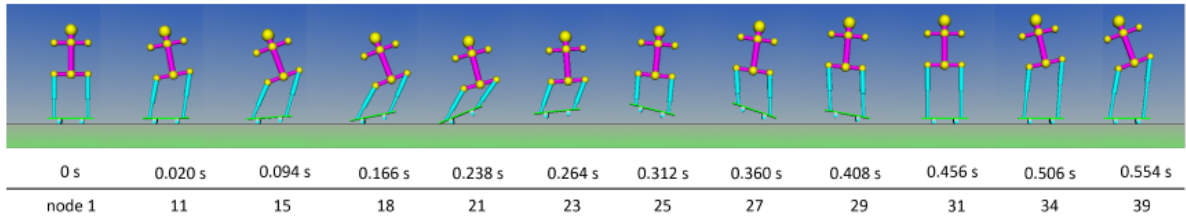


Figure 7.3: The RO simulation results from the study conducted by Kolev [14]. The skateboarder's legs were fixed to the skateboard and the upper body was modelled as a rigid-body. The arms were drawn for aesthetic appeal.

It has thus far been shown that the skateboard-skateboarder system, through the application of trajectory optimization, can be used to replicate the motion of the SO and RO manoeuvres. It should now be analysed whether the system can be used to replicate the GRFs experienced by the skateboard too.

7.2 The Ground Reaction Forces

The two chosen aspects of the GRFs which can be compared to literature are the peak GRFs and the GRF profiles. Each will be analysed individually.

7.2.1 Peak Ground Reaction Forces

A summary of the simulated peak GRFs for the various ollie manoeuvres and the peak GRFs recorded in literature is shown in Table 7.1. The simulated SO and RO take-off and landing GRFs fall outside of one standard deviation of the results obtained in literature. The same is true for the simulated peak GRFs on take-off and landing for the 0.45m OD. However, the peak GRF of the simulated 0.36m OD at take-off is within one standard deviation of the results obtained in study 2. Additionally, it is interesting to note the 5 BW difference between the simulated RO and SO landing GRFs, considering that both manoeuvres involve essentially the same vertical translation.

Table 7.1: A comparison of the peak GRF data from literature and the simulated results. The GRFs are expressed in terms of BW.

	Study 1		Study 2		Study 3		Simulation	
	Take-off	Landing	Take-off	Landing	Take-off	Landing	Take-off	Landing
SO	-	-	2.47 ± 0.38	2.40 ± 0.33	2.05 ± 0.17	4.61 ± 1.19	5.79	3.14
RO	-	-	2.55 ± 0.51	2.71 ± 0.23	-	-	3.78	8.01
0.36m OD	-	-	2.34 ± 0.32	3.15 ± 0.51	-	-	2.58	4.21
0.45m OD	-	4.74 ± 0.46	-	-	-	-	2.90	3.57

Another simulation result which seems to bare conflicts with intuition is that the peak landing GRF for the 0.36m OD is greater than that of the 0.45m OD, despite the 0.36m OD being performed off a higher step. It is shown in study 1 and study 2 that the landing GRF should be greater for the 0.45m OD than the 0.36m OD.

This analysis of the discrepancies of the simulated peak GRFs and the peak GRF data from literature suggests that, although the motion of the ollie may have been replicated by the system, the forces within the system have not been adequately represented in the modeling process. Further analysis of the GRF profiles is necessary to justify this conclusion.

7.2.2 Ground Reaction Force Profiles

Current literature provides the GRF profiles for the RO, the OU at take-off and the OD at landing. However, since the OU was not able to be generated in this study, the simulated RO can be compared to the OU GRF profiles due to the similarities in the two manoeuvres at take-off. The comparison of the GRF profiles for the simulated RO and OD manoeuvres and the data obtained from literature are shown in Figures 7.4 and 7.5. For both simulated results, since the sample frequency of the simulated results is far less than the frequency of the results from literature, an additional three-point moving average was applied to the results in order to give an illustration of the average GRFs by

smoothing the results.

Looking at the take-off GRF comparison in Figure 7.4, it can be seen that the moving average GRF profile has a similar shape to the average GRF of all participants. Both profiles have a global maximum in the initial stage of the take-off, and a local maximum immediately before the end of the take-off phase. Furthermore, the magnitude of the recorded GRFs differ by less than 0.5 BW. This suggests that, although the peak GRFs of the simulated and recorded RO may differ significantly, the averaged GRF profile resembles the GRF profiles recorded in literature.

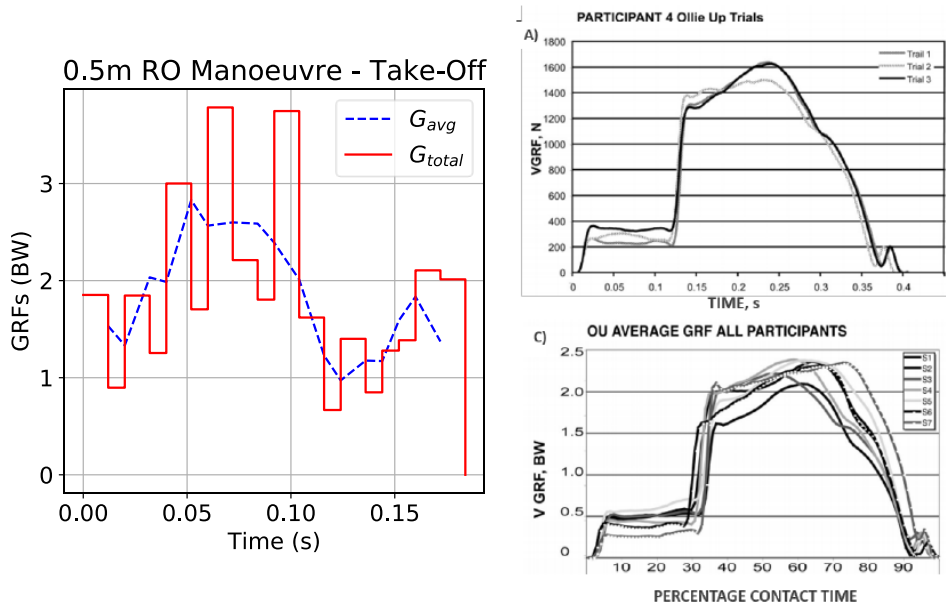


Figure 7.4: A comparison of the simulated RO take-off GRF profile to the OU take-off GRF profiles recorded in literature [2], with a three-point moving average shown in blue.

The same can be said for the simulated 0.45m OD results when compared to the results recorded in literature, shown in Figure 7.5. Both the three-point moving average profile and the average GRF for all participants have a local maximum global maximum immediately. The magnitudes of the GRF profiles, however, do not bare such similarities. The simulated GRF profiles are approximately half the magnitude of the profiles from literature.

Furthermore, the simulated 0.45m OD results show another significantly high local maximum occurring shortly before the end of the simulation. This local maximum may occur as a result of reducing the complexity and motion of the the human leg to a prismatic joint. Unlike the human leg, the prismatic joint is able to contract in on itself while exerting a force less than the biped's BW until the joint reaches its hard-stop limits. When the human leg makes contact with the skateboard, it immediately applies a force greater than or equal to the BW of the human. This is shown in Figure 7.6, where, despite the foot being in contact with the skateboard at landing, the reaction force is less

than 1 BW. Therefore, modeling the skateboarder's legs using prismatic joints may have caused the model to lack the required complexity to encapsulate the key dynamics of the skateboarder.

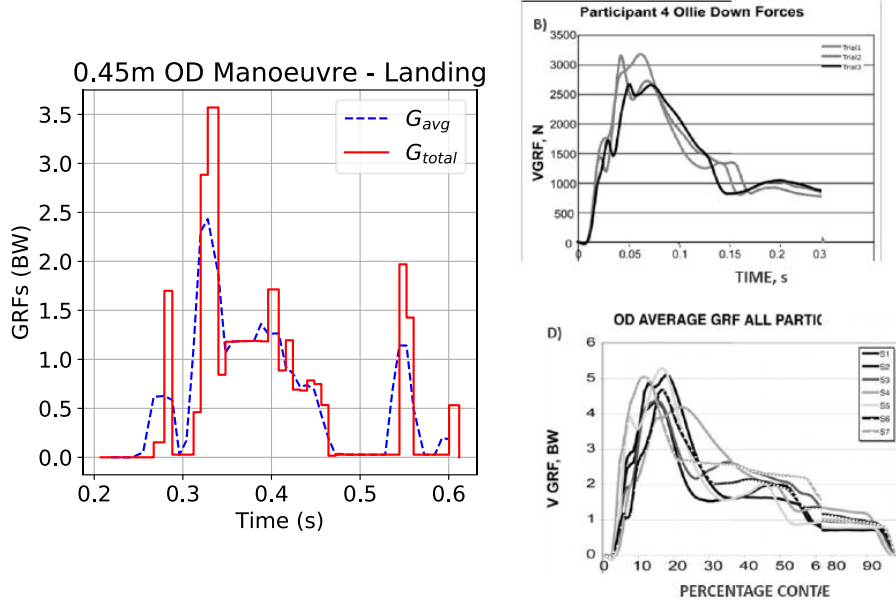


Figure 7.5: A comparison of the simulated OD landing GRF profile to the OD landing GRF profiles recorded in literature [2], with a three-point moving average shown in blue.

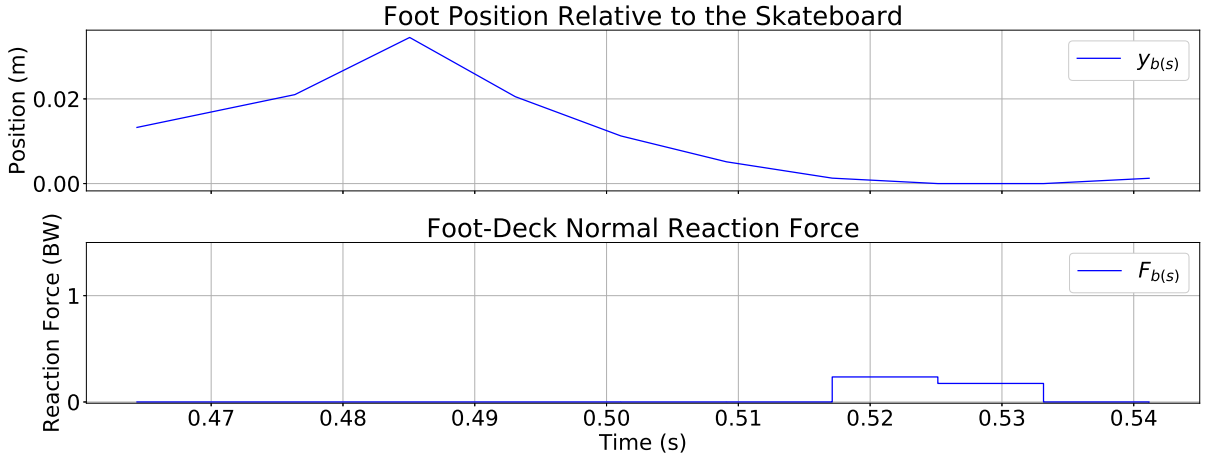


Figure 7.6: Plots of the position of the front foot relative to the skateboard and the foot-deck reaction force during landing. The foot is in contact with the skateboard for $0.515s < t < 0.535s$

Lastly, the force profiles recorded in literature for a skateboarder performing a kickflip [?] can also be compared to the simulated RO GRF profile. The comparison, shown in Figure 7.7, again displays similarities between the GRF profiles. Considering that the simulated results correspond with the approximate time interval $0.4s \leq t \leq 1.6s$, the general trends of the profiles are visibly similar. Both profiles have a local maximum shortly before take-off. And, upon landing, there is a sharp peak in the GRF profiles. It can also be seen that the magnitudes of the GRF profiles are of a similar scale. However, another local minimum occurs shortly after the the skateboard lands on the ground. This

may be due to the fact that the biped is still airborne at this stage. This discrepancy is further proven in Figure 7.8, which shows that the real-life skateboarder's feet are in contact with the skateboard during landing, but that the biped lands on the skateboard once the skateboard has already landed.

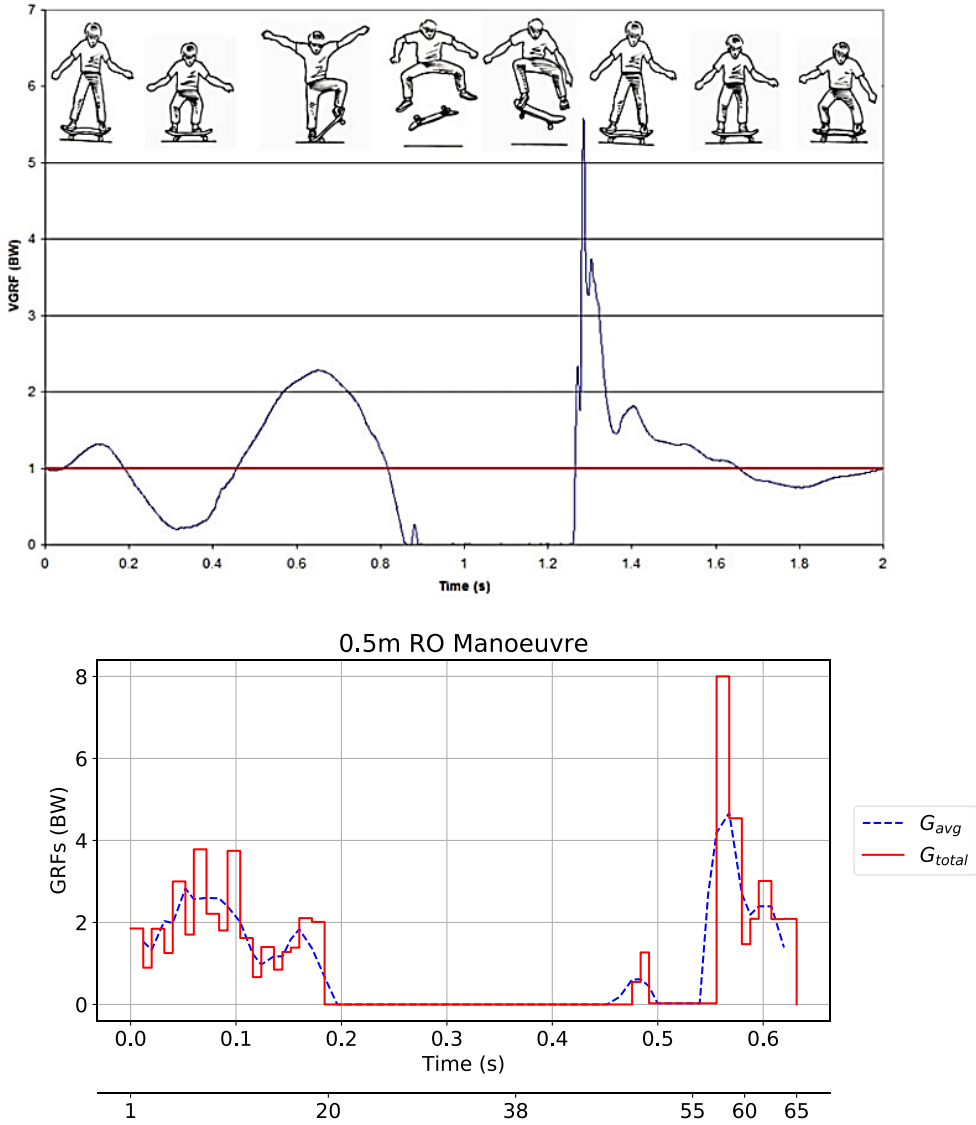


Figure 7.7: A comparison of the recorded GRF profile for a kickflip [?] to the simulated RO GRF profile.

7.3 Additional Observations

A secondary test was conducted for the SO manoeuvre in order to gauge the means by which the skateboard-skateboarder model increases the height of the jump. An alteration to the path constraints given in Table 5.9 was made to increase the apex height, such that at $n = 38$, ${}^{bw}y \geq 1.0\text{m}$ and ${}^{fw}y \geq 1.0\text{m}$. The simulation results are shown in Figure 7.9.

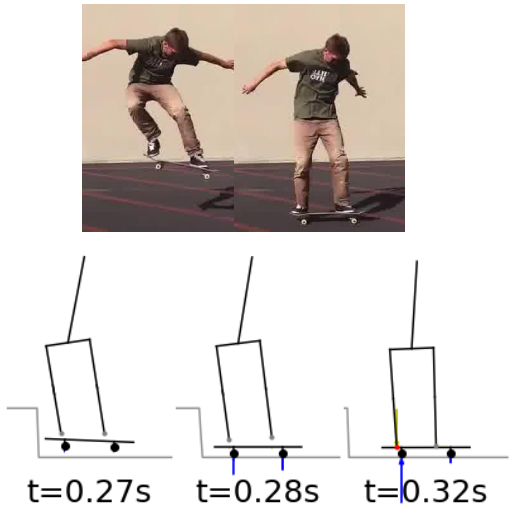


Figure 7.8: The real-life skateboarder lands on the ground with his feet already on the skateboard, whereas the biped lands on the skateboard once the skateboard has already made contact with the ground.

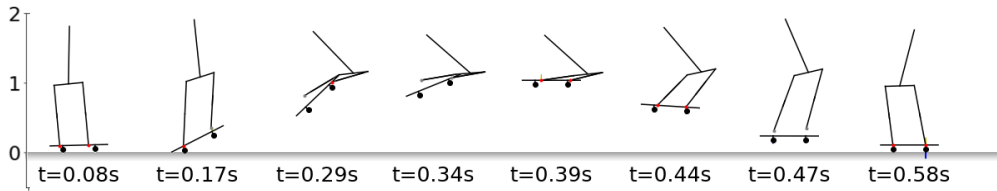


Figure 7.9: The simulated trajectory of the high SO reaching a 1.0m apex. It can be seen that the biped tucks its legs in.

It is interesting to note that, in order to maximize the ollie height, the biped model raises its legs up close to its body, effectively “tucking” its legs in. This motion is precisely what was observed in the world record setting ollie by Aldrin Garcia shown in Figure 2.2.

Chapter 8

Conclusions

The aim of this study was to apply the principles of biomechanics to develop a mathematical model for a skateboard and skateboarder that, through the application of trajectory optimization, has the required complexity to replicate the ollie manoeuvre. Conclusions will now be made as to the extent at which this was achieved.

An identified area of the skateboard-skateboarder system which has not been explored thoroughly in literature was formulating a trajectory optimization problem which can model unscheduled inelastic multi-body collisions. This study demonstrated that the contact-implicit method proposed by Posa et al. [13] was adequate to model the various inelastic collisions, including the contacts between the ground and the skateboard wheels, and the skateboard deck and the skateboarder's foot. Furthermore, it was shown that this method can be used in conjunction with the hybrid dynamics method to model the elastic collisions within the system, namely the collision between the skateboard tail and the ground. Thus, it can be concluded that the methods used to model the scheduled and unscheduled contacts and collisions within the system were successfully implemented.

The results of the simulated SO and RO manoeuvres showed that, at a high-level, the motion of the simulated system bared noticeable resemblances to the real-world motion of the skateboarder. The biped model was able to use its feet to interact with the skateboard model at various positions along the skateboard deck, and the biped's feet were able to leave the skateboard deck entirely. This is a major improvement to the system developed by Kolev [14]. Furthermore, when maximising the apex height of the SO, the biped model was shown to "tuck" in its legs, which replicates the observed motion of skateboarders. It can thus be concluded that the system was able to replicate the motion of the ollie manoeuvre.

Comparing the results of the simulated RO and OD GRF profiles to the GRF profiles measured in literature, it was found that, by applying an averaging function to the simulated GRF profiles, the shape of the profiles were noticeably similar in terms of the observed local and global maxima. However, the magnitude of the simulated OD profile was significantly less than the results measured in literature. This was further observed upon comparing the peak GRFs for the SO, RO and OD manoeuvres. The simulated peak GRFs for all but one of the manoeuvres (the 0.36m OD peak landing GRF) fell outside of one standard of the results measured in literature. This leads to the conclusion that, although the motion of the ollie is replicated by the system, the forces involved in

the system have not been adequately replicated.

The discrepancies between the simulated and real-life measured GRF results suggest that there may have been oversight regarding the assumption made to model the system. It was identified that modeling the human as a biped, with legs modelled as rigid links connected by a prismatic joint, may have been the major contributor to the discrepancies between the GRF results obtained. Thus, it can be concluded that the biped model used to model the skateboarder lacked the required complexity to encapsulate the key dynamics of the skateboarder.

Chapter 9

Recommendations for Future Work

This chapter details possible approaches that could be used to improve the results of this study, and specifically, develop the skateboard and skateboarder models.

9.1 Development of the System Models

9.1.1 The Skateboarder Model

Due to the time constraints of the project, the scope of the skateboarder model was chosen as the simplest model that exhibits the key aspects of a skateboarder. Upon analysing videos of skateboarder's it was decided that arms were not an essential aspect of the manoeuvre, thus, they were not included in the final design. However, a model with arms was developed and implemented in a trajectory optimization problem to generate the SO manoeuvre. The model is shown in Figure 9.1 and the simulated SO manoeuvre is shown in Figure 9.2.

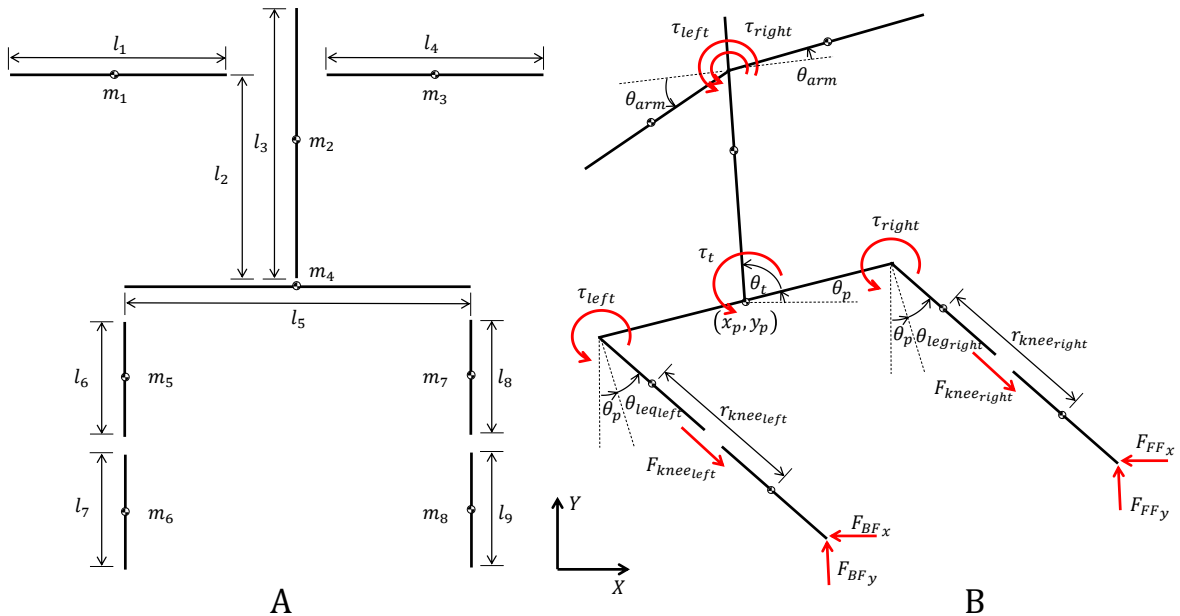


Figure 9.1: A model of a biped with a torso and arms proposed for future development of the skateboard model.

Since it has been demonstrated that this model is able to perform an ollie, it would be possible to use this model to determine the effects that arms have on the manoeuvre,

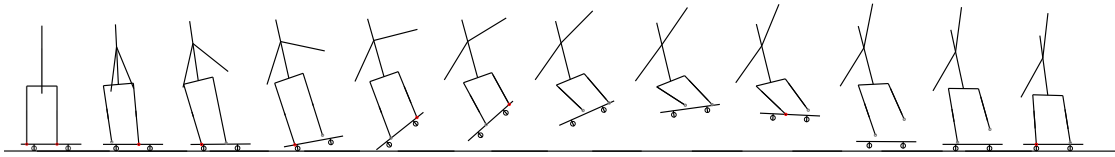


Figure 9.2: Simulated results of the biped model proposed for future works performing a 0.5m SO manoeuvre.

similar to the study by Wilson et al. [23] regarding the effects that arms have on human jumping.

Furthermore, a possible reason given for the difference between the simulated and measured GRF profiles provided previously is the prismatic joint used to model the human leg. In order to develop the skateboarder model, the skateboarder’s legs could be modelled as a prismatic joint with a spring-dampener element at the knee. This would improve the modeling accuracy of the functionality of the human leg.

9.1.2 The Skateboard Model

It was found that the skateboard model was sufficiently complex to generate a basic ollie manoeuvre. However, further considerations should be given to the modeling approach used for the skateboard and the “pop”. A key physical property of the skateboard model which was neglected was the pop-angle of the skateboard. Looking at the image of the skateboard shown in Figure 9.3, the pop angle is the angle at which the skateboard nose and tail are fixed relative to the deck. Including this in the model design would ensure that the impact between the skateboard tail and the ground during the “pop” is not occurring on a point on the tail, but rather, on a surface that is pressed up against the ground.



Figure 9.3: The pop-angle of the skateboard is the angle at which the skateboard nose and tail are set at relative to the deck [18].

Furthermore, the mathematics used to model the “pop” were based on assumptions made regarding the collision between the skateboard tail and the ground. The mathematical modeling of the collision should be re-explored, and a more in-depth consideration should be given to the complexity of the collision.

Bibliography

- [1] J. Koschorreck and K. Mombaur, “Modeling and optimal control of human platform diving with somersaults and twists,” *Optimization and Engineering*, vol. 13, no. 1, pp. 29–56, 2012.
- [2] E. C. Frederick, J. J. Determan, S. N. Whittlesey, and J. Hamill, “Biomechanics of skateboarding: Kinetics of the ollie,” *Journal of applied biomechanics*, vol. 22, no. 1, pp. 33–40, 2006.
- [3] R. Meronek, “Maloof high ollie challenge las vegas,” 2011. [Online]. Available: <https://skateparkoftampa.com/spot/a.aspx?ID=1519>
- [4] “Jumping: the ollie.” [Online]. Available: <https://www.exploratorium.edu/skateboarding/trick02.html>
- [5] Board size chart. Primitive Skateboarding. [Online]. Available: <https://primitiveskate.com/pages/board-size-chart>
- [6] J. Diebel, “Representing attitude: Euler angles, unit quaternions, and rotation vectors,” *Matrix*, vol. 58, no. 15-16, pp. 1–35, 2006.
- [7] S. Shield, “Pyomo tutorials,” 2019. [Online]. Available: https://github.com/UCTMechatronics/pyomo_tutorials
- [8] R. J. Full and D. E. Koditschek, “Templates and anchors: neuromechanical hypotheses of legged locomotion on land,” *Journal of experimental biology*, vol. 202, no. 23, pp. 3325–3332, 1999.
- [9] A. S. Kuleshov, “Nonlinear dynamics of a simplified skateboard model (p24),” in *The Engineering of Sport 7*. Springer, 2008, pp. 135–142.
- [10] Y. G. Ispolov and B. Smolnikov, “Skateboard dynamics,” *Computer methods in applied mechanics and engineering*, vol. 131, no. 3-4, pp. 327–333, 1996.
- [11] A. E. Österling, “On the skateboard, kinematics and dynamics,” *Kinematics and Dynamics (May 21, 2004)*, 2004.
- [12] M. P. Kelly, “Transcription methods for trajectory optimization: a beginners tutorial,” *arXiv preprint arXiv:1707.00284*, 2017.
- [13] M. Posa, C. Cantu, and R. Tedrake, “A direct method for trajectory optimization of rigid bodies through contact,” *The International Journal of Robotics Research*, vol. 33, no. 1, pp. 69–81, 2014.

- [14] D. Kolev, *Mathematical Modelling and Optimal Control of a Skateboarding Manoeuvre*, University of Cape Town, 2017.
- [15] I. Mordatch, E. Todorov, and Z. Popović, “Discovery of complex behaviors through contact-invariant optimization,” *ACM Transactions on Graphics (TOG)*, vol. 31, no. 4, p. 43, 2012.
- [16] A. Bhatia, “The physics of doing an ollie on a skateboard, or, the science of why i can’t skate,” 2014. [Online]. Available: <https://www.wired.com/2014/10/skateboard-physics-empzeal/>
- [17] “5 steps to better ollies,” 2015. [Online]. Available: <https://www.youtube.com/watch?v=OrOZxOTIv-g>
- [18] “Punisher skateboards butterfly jive complete 31-inch skateboard with canadian maple,” 2011. [Online]. Available: <https://www.youtube.com/watch?v=0is-9ltin-A&t=42s>
- [19] S. Plagenhoef, F. G. Evans, and T. Abdelnour, “Anatomical data for analyzing human motion,” *Research quarterly for exercise and sport*, vol. 54, no. 2, pp. 169–178, 1983.
- [20] S. Cave, “Skateboarding: From wooden box boards to commercial mainstream,” 2018. [Online]. Available: <https://www.liveabout.com/brief-history-of-skateboarding-3002042>
- [21] T. Montgomery, “State of skateboarding industry,” 2009. [Online]. Available: <https://web.archive.org/web/20140812232423/http://www.shop-eat-surf.com/2009/05/the-state-of-the-skateboarding-industry/>
- [22] C. J. Donnelly, D. G. Lloyd, B. C. Elliott, and J. A. Reinbolt, “Optimizing whole-body kinematics to minimize valgus knee loading during sidestepping: implications for acl injury risk,” *Journal of biomechanics*, vol. 45, no. 8, pp. 1491–1497, 2012.
- [23] C. Wilson, M. R. Yeadon, and M. A. King, “Considerations that affect optimised simulation in a running jump for height,” *Journal of Biomechanics*, vol. 40, no. 14, pp. 3155–3161, 2007.
- [24] W. Blajer, J. A. Goszczyński, and M. Krawczyk, “The inverse simulation study of aircraft flight path reconstruction,” *Transport*, vol. 17, no. 3, pp. 103–107, 2002.
- [25] Y. Xiang, H.-J. Chung, J. H. Kim, R. Bhatt, S. Rahmatalla, J. Yang, T. Marler, J. S. Arora, and K. Abdel-Malek, “Predictive dynamics: an optimization-based novel approach for human motion simulation,” *Structural and Multidisciplinary Optimization*, vol. 41, no. 3, pp. 465–479, 2010.

- [26] G. Capi, S.-i. Kaneko, K. Mitobe, L. Barolli, and Y. Nasu, “Optimal trajectory generation for a prismatic joint biped robot using genetic algorithms,” *Robotics and autonomous systems*, vol. 38, no. 2, pp. 119–128, 2002.
- [27] “Learn how to ollie with skateboard trick tips.” [Online]. Available: <http://www.skateboard-trick-tips.com/tricktips/ollie.html>
- [28] “The ”ollie” explained - self destruct ”skate basicks” dvd,” 2011. [Online]. Available: https://www.youtube.com/watch?v=0is-9ltin_A&t=42s
- [29] “Highest ollie on a skateboard,” 2011. [Online]. Available: <https://www.guinnessworldrecords.com/world-records/skateboarding-highest-ollie->
- [30] R. A. Jacobs and E. L. Keller, “Skateboard accidents,” *Pediatrics*, vol. 59, no. 6, pp. 939–942, 1977.
- [31] S. B. Kyle, M. L. Nance, G. W. Rutherford Jr, and F. K. Winston, “Skateboard-associated injuries: participation-based estimates and injury characteristics,” *Journal of Trauma and Acute Care Surgery*, vol. 53, no. 4, pp. 686–690, 2002.
- [32] A. Leuchanka, J. Ewen, and B. Cooper, “Bipedal in-shoe kinetics of skateboarding—the ollie,” *Footwear Science*, vol. 9, no. sup1, pp. S122–S124, 2017.
- [33] What size skateboard do you need? [Online]. Available: <https://www.warehouseskateboards.com/blog/2017/11/22/size-skateboard-need/>
- [34] M. Kelly, “An introduction to trajectory optimization: How to do your own direct collocation,” *SIAM Review*, vol. 59, no. 4, pp. 849–904, 2017.
- [35] A. Patel, “Understanding the motions of the cheetah tail using robotics,” Ph.D. dissertation, University of Cape Town, 2014.
- [36] M. Srinivasan and A. Ruina, “Computer optimization of a minimal biped model discovers walking and running,” *Nature*, vol. 439, no. 7072, p. 72, 2006.
- [37] M. Hubbard, “Lateral dynamics and stability of the skateboard,” *Journal of Applied Mechanics*, vol. 46, no. 4, pp. 931–936, 1979.
- [38] R. M. Murray, *A mathematical introduction to robotic manipulation*. CRC press, 2017.
- [39] D. T. Greenwood, *Advanced dynamics*. Cambridge University Press, 2006.
- [40] B. Siciliano, L. Sciavicco, L. Villani, and G. Oriolo, *Robotics: modelling, planning and control*. Springer Science & Business Media, 2010.

- [41] J. T. Betts, *Practical methods for optimal control and estimation using nonlinear programming*. Siam, 2010, vol. 19.
- [42] ——, “Survey of numerical methods for trajectory optimization,” *Journal of guidance, control, and dynamics*, vol. 21, no. 2, pp. 193–207, 1998.
- [43] A. Hereid, E. A. Cousineau, C. M. Hubicki, and A. D. Ames, “3d dynamic walking with underactuated humanoid robots: A direct collocation framework for optimizing hybrid zero dynamics,” in *2016 IEEE International Conference on Robotics and Automation (ICRA)*. IEEE, 2016, pp. 1447–1454.
- [44] K. Mombaur, A. Truong, and J.-P. Laumond, “From human to humanoid locomotionan inverse optimal control approach,” *Autonomous robots*, vol. 28, no. 3, pp. 369–383, 2010.
- [45] R. Fletcher, S. Leyffer, D. Ralph, and S. Scholtes, “Local convergence of sqp methods for mathematical programs with equilibrium constraints,” *SIAM Journal on Optimization*, vol. 17, no. 1, pp. 259–286, 2006.
- [46] HSL, “A collection of fortran codes for large scale scientific computation.” [Online]. Available: <http://www.hsl.rl.ac.uk/>
- [47] E. H. Bani-Hani, J. Lopez, and G. Mohanan, “Data on the coefficient of static friction between surfaces coated with different sizes of rubber granules produced from used tires,” *Data in brief*, vol. 22, pp. 940–945, 2019.
- [48] J. Bennet and R. Meepagala, “Coefficients of restitution,” 2006. [Online]. Available: <https://hypertextbook.com/facts/2006/restitution.shtml/>

Appendix A

Additional Information

A.1 Example: Application of the Euler-Lagrange Method for Chapter 3

Derive the Dynamics of the skateboard model shown in figure 5.15 using the Euler-Lagrange method.

The generalized coordinates describing the skateboard model can be chosen as:

$${}^s\mathbf{q} = [{}^s x, {}^s y, {}^s \theta]^\top \quad (\text{A.1})$$

The position of the skateboard COM can be expressed in terms of the generalized coordinates:

$${}^s p = \begin{bmatrix} {}^s x \\ {}^s y \end{bmatrix} \quad (\text{A.2})$$

The derivative of the position of the skateboard COM can be calculated as follows:

$${}^s \dot{p} = \begin{bmatrix} {}^s \dot{x} \\ {}^s \dot{y} \end{bmatrix} \quad (\text{A.3})$$

The potential and kinetic energies of the skateboard can be calculated:

$$V = m_s g {}^s y \quad (\text{A.4})$$

$$T = \frac{1}{2} {}^s \dot{p}^\top m_s {}^s \dot{p} + \frac{1}{2} {}^s I {}^s \dot{\theta}^2 \quad (\text{A.5})$$

$$T = \frac{1}{2} {}^s I {}^s \dot{\theta}^2 + \frac{1}{2} m_s {}^s \dot{x}^2 + \frac{1}{2} m_s {}^s \dot{y}^2 \quad (\text{A.6})$$

The Lagrangian can now be calculated:

$$\mathcal{L} = T - V \quad (\text{A.7})$$

$$\mathcal{L} = \frac{1}{2} {}^s \dot{p}^\top m_s {}^s \dot{p} + \frac{1}{2} {}^s I {}^s \dot{\theta}^2 - m_s g {}^s y \quad (\text{A.8})$$

A.1. EXAMPLE: APPLICATION OF THE EULER-LAGRANGE METHOD FOR CHAPTER 3

The position of the applied forces in the system can now be calculated. The position of the back foot applied forces can be described as:

$${}^{bf}r = \begin{bmatrix} x - {}^B r \cos({}^s\theta) \\ y - {}^B r \sin({}^s\theta) \end{bmatrix} \quad (\text{A.9})$$

and the force vector for the back foot can be described as:

$${}^{bf}f = \begin{bmatrix} {}^B F_x \\ - {}^B F_y \end{bmatrix} \quad (\text{A.10})$$

The generalized force vector can be formulated as follows:

$$Q_i = \sum_{j=1}^m \mathbf{f}_j \cdot \frac{\partial \mathbf{r}_j}{\partial q_i} \quad (\text{A.11})$$

where $i = 1, \dots, 3$ is an index for the generalized coordinates, and $j = 1, \dots, 4$ is an index for the number of generalized forces. The equations of motion of the system can be calculated using the following equations:

$$\frac{d}{dt} \frac{\partial \mathcal{L}}{\partial \dot{q}} - \frac{\partial \mathcal{L}}{\partial q} = Q \quad (\text{A.12})$$

An example of the obtained equations of motion is given for ${}^s\ddot{x}$ below:

$${}^s\ddot{x} = \frac{{}^B F_x + {}^F F_x}{m_s} \quad (\text{A.13})$$

Appendix B

Links to Simulation Videos & Code

B.1 The Simulated Videos

The videos of the simulated SO, RO and OD trajectories have been uploaded to YouTube on the channel:

N. Anderson FYP 2019

https://www.youtube.com/channel/UCVdvNixm89RMvSaJ_IHw_wA

The SO simulation:

“SO simulation 0.5m”

<https://www.youtube.com/watch?v=jh5BW7sJL98>

“SO simulation 0.5m realtime”

https://www.youtube.com/watch?v=1BKB4_ycaac

The RO simulation:

“RO simulation 0.5m”

<https://www.youtube.com/watch?v=7k9ztWggttY>

“RO simulation 0.5m realtime”.

<https://www.youtube.com/watch?v=mNDXiJQyyFI>

The 0.36m OD simulation:

“OD simulation 0.36m”

<https://www.youtube.com/watch?v=LryZDw0XuRc>

“OD simulation 0.36m realtime”

<https://www.youtube.com/watch?v=0ilhm5zdrVo>

The 0.45m OD simulation:

“OD simulation 0.45m”

<https://www.youtube.com/watch?v=KNe8lxcbm2w>

“OD simulation 0.45m realtime”

<https://www.youtube.com/watch?v=oxfUNo4-prw>

B.2 The Python Code

Some of the Python code used for this project is available for viewing in the following GitHub repository:

https://github.com/NickHAnderson019/NAnderson_FYP_2019